The Thesis Committee for Owen Michael O'Neal
Certifies that this is the approved version of the following thesis:

Measurements of Adiabatic Effectiveness from Full Coverage Film Cooling on a Scaled Turbine Vane with Laidback Fanshaped Holes

APPROVED BY
SUPERVISING COMMITTEE:

Supervisor:

David G. Bogard

Michael Crawford

Measurements of Adiabatic Effectiveness from Full Coverage Film Cooling on a Scaled Turbine Vane with Laidback Fanshaped Holes

by

Owen Michael O'Neal

Thesis

Presented to the Faculty of the Graduate School of

The University of Texas at Austin

in Partial Fulfillment

of the Requirements

for the Degree of

Master of Science in Engineering

The University of Texas at Austin

December 2017

Dedication

This thesis is dedicated to my family, who have always supported me throughout my education. I would not be where I am today without your love and guidance, thank you.

Acknowledgements

I would first like to thank Dr. David Bogard for his patience and mentorship as an advisor these past two years. His dedication to his field of study and to his students is admirable. He has helped me better understand the responsibilities of the engineering profession tremendously. This research was funded by Siemens energy, and I would like to thank Dr. Michael Crawford and the Siemens team for providing helpful feedback and reviewing this thesis.

I would also like to thank all of the fellow members of the TTCRL who I have had the pleasure of working with. Kyle Chavez, Josh Anderson, John McClintic, Jacob Moore, Fraser Jones, Khanh Hoang, Chris Yoon, Dale Fox -- thanks for the good times and all the Taco Tuesdays. Special thanks are owed to Kyle Chavez for training me to use the large wind tunnel facility when I first joined the lab. His extensive contributions to the test section preparation and the creation of the post-processing scripts made this thesis possible. I would also like to thank Jacob Moore for his assistance in the collection of experimental data used in this thesis.

Thanks again to my friends and family. Your support has kept me going these past two years, and made my time in Austin truly memorable.

Abstract

Measurements of Adiabatic Effectiveness from Full Coverage Film Cooling on a Scaled Turbine Vane with Laidback Fanshaped Holes

Owen Michael O'Neal, M.S.E.

The University of Texas at Austin, 2017

Supervisor: David G. Bogard

This study was focused on measurements of adiabatic effectiveness on a scaled turbine vane which made use of a contoured endwall to match engine conditions. The vane model featured a full coverage film-cooling configuration with five rows of cylindrical holes in the showerhead and ten rows of laidback fanshaped holes distributed on the pressure and suction sides. The vane model was tested across a wide range of blowing ratios in several different coolant configurations including: individual rows on the pressure and suction side, full coverage tests with and without showerhead cooling, and full coverage tests at low and high mainstream turbulence levels. Comparisons between these configurations were made in order to assess the effects of local curvature, showerhead cooling, and mainstream turbulence levels. Single row tests measured in areas of high convex curvature tended to have an improved performance relative to flat plate predictions, while the opposite was true for rows in areas of concave curvature. Overall, showerhead cooling did not provide any significant improvements in effectiveness far downstream on both the pressure and suction side. Increasing mainstream turbulence levels tended to diminish the

film cooling effectiveness. The negative effect of higher mainstream turbulence was most significant at low blowing ratios, but became negligible at higher flow rates.

Table of Contents

List of Tables

List of Figures

Nomenclature

SYMBOLS

A	Area
AR	Area Ratio
c	Coverage
C	Chord length of the model vane
C_{ax}	Axial chord length of the model vane
C_d	Discharge coefficient
C_p	Pressure distribution
d	Coolant hole diameter, or orifice throat diameter
DR	Density ratio, ρ_c/ρ_∞
F	Mass fraction hole splits
g	Gravity
h	Heat transfer coefficient, Lab altitude
H	Height of the model vane
I	Coolant momentum flux ratio
k	Thermal conductivity
L	Coolant hole length, Temperature lapse rate
$\dot{m}$	Mass flow rate
M	Coolant blowing ratio, Molar mass
n	Number
P	Pressure, Pitch length
q''	Specific heat flux
R	Universal gas constant, Local radius of wall curvature
Re	Reynolds number
s	Streamwise coordinate from stagnation line (stagnation = 0)
S_e	Equivalent slot width
U	Average velocity
VR	Velocity Ratio, U_c/U_∞
t	Breakout length
T	Temperature
Tu	Turbulence level
x	Local streamwise coordinate (downstream hole exit = 0)
	Horizontal camera pixel location
y	Wall-normal coordinate
	Vertical camera pixel location
z	Spanwise coordinate (bottom of imaging pitch = 0)

GREEK

α	Streamwise Injection Angle
β	Ratio of orifice plate to pipe diameter,

	Spanwise (compound) injection angle
γ	Heat capacity ratio
δ	Uncertainty
Δ	Difference
ε	Emissivity
ρ	Density
η	Effectiveness, Thermal efficiency
ξ	Scaled downstream distance
σ	Standard deviation
ψ	Percent Distance

SUBSCRIPTS & ACCENTS

atm	Atmosphere
aw	Adiabatic wall
c	Coolant
cyl	Cylindrical or metering
dyn	Dynamic
exit	At the hole exit
exp	Expansion
f	With film cooling
fossilized	Fossilized
fwd	Forward
h, holes	Holes
inlet	At the test section inlet
local	Local
measured	Measured
o	Orifice plate
pipes	Pipes
ref	reference
rms	Root mean square
row	Row
s	Surface
static	Static
t	Stagnation
variations	Variations
wall	Wall surface
0	Without film cooling, Due to conduction, At sea level
∞	Referring to mainstream flow

ACRONYMS

AO	All Open
CI	Confidence Interval
CN	Contraction Nozzle

CFD	Computational Fluid Dynamics
DAQ	Data Acquisition
DLT	Direct Linear Transformation
HP	Horse Power
IR	Infrared
LBF	Laidback Fanshaped`
NHFR	Net Heat-Flux Reduction
NIST	National Institute of Standards and Technology
NSH	Non-Showerhead
PCHIP	Piecewise Cubic Hermite Interpolating Polynomial
PS	Pressure Side
RH	Relative Humidity
SR	Single Row
SS	Suction Side
S1-5	Set Point 1-5
TTCRL	Turbulence and Turbine Cooling Research Laboratory

Chapter 1 – Introduction

1.1 - Gas Turbine Power and the Brayton Cycle

Gas turbines are ubiquitous in the realms of energy generation and transportation. Recent advances in natural gas recovery from shale formations have substantially reduced the price of natural gas in the United States. Natural gas combined cycle power plants, which recover the waste heat created after combustion to generate steam for a steam turbine, have efficiencies approaching 60% [1]. Their competitive pricing and high efficiency have made natural gas powered gas turbines an increasingly popular choice for new power generation compared to coal and nuclear sources. The aviation sector is also largely dependent on the performance of gas turbine engines, which represent a significant capital expense necessary to power a commercial fleet. For example, a single GE9X engine used to power a Boeing 777 costs upwards of $40 million USD, and is expected to have 30+ year lifetime [2]. That investment, plus the cost of jet fuel consumed throughout its lifetime, provides a strong incentive for the aviation industry to ensure that gas turbine engines operate as efficiently as possible and maximize their lifetime of operation.

The thermodynamic processes of a gas turbine engine can be approximated by the Open Brayton Cycle. In the cycle (shown below in Figure 1.1), the working fluid of the engine undergoes alternating processes of isentropic compression and expansion and isobaric addition and rejection. In the open version of the cycle, the exhaust gases leaving the turbine at state 4 can either be expanded through a nozzle to create thrust used for propulsion or used to produce shaft work for electric generation. The thermal efficiency of

an ideal Brayton cycle is shown by Equation 1.1, and when a constant specific heat is assumed, by Equation 1.2 [3]. The primary driver of efficiency which engine designers have the most control over is the combustion temperature or turbine inlet temperature (T_3). Much of the research efforts to improve the performance of gas turbine engines have been focused on methods to improve the durability of critical engine components at higher temperatures.

$$\eta_{th} = \frac{(h_3 - h_4) - (h_2 - h_1)}{(h_3 - h_2)} \tag{1.1}$$

$$\eta_{th} = 1 - \frac{T_4 - T_1}{T_3 - T_2} \tag{1.2}$$

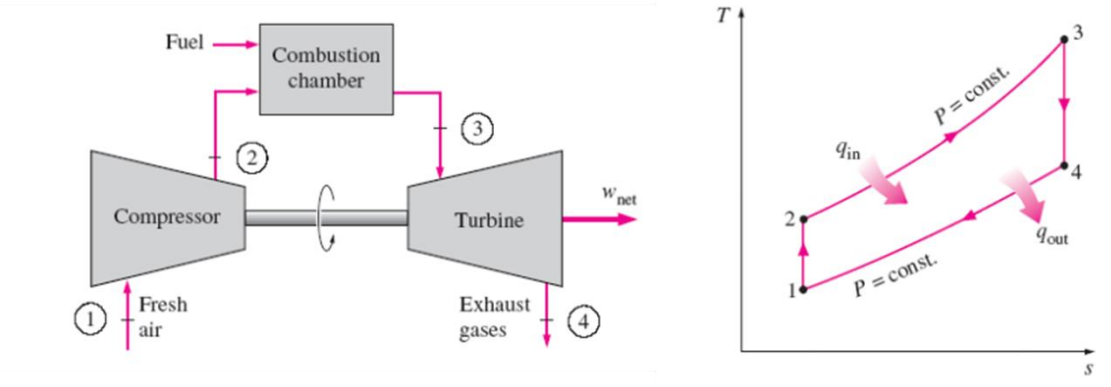

Figure 1.1: Diagram of idealized open Brayton cycle

Process 1-2: Isentropic compression through the engine's compression stages
Process 2-3: Isobaric heat addition in the combustor
Process 3-4: Isentropic expansion through the engine's turbine stage
Process 4-1: Isentropic heat rejection

1.2 - BACKGROUND ON FILM COOLING

The turbine inlet temperatures used in gas turbine engines have steadily increased over the last sixty years due to advances in heat resistant materials and the use of active cooling systems, shown in Figure 1.2. Typical combustion temperatures exceed 2000K, which is far greater than the thermal limits that the metal alloys used can withstand. The engine components which experience the greatest thermal loads are the first stage nozzle guide vanes and rotor vanes, immediately downstream of the combustor. Active cooling systems are necessary to protect the turbine parts from degradation and prevent engine failure at high operating temperatures. Film cooling supplements internal cooling techniques by allowing a small supply of coolant air to flow over the external surface, which reduces the heat transfer between the mainstream gas and the turbine component.

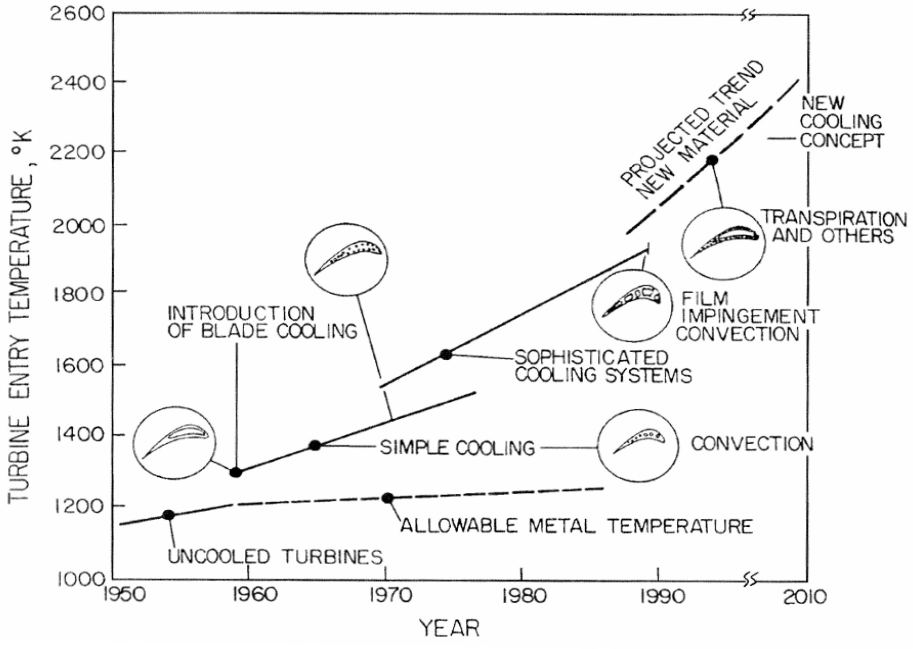

Figure 1.2: Increase in turbine inlet temperatures associated with advances in cooling systems

Both internal cooling and external "film" cooling methods are used to reduce the wall temperature of turbine components. A supply of coolant air is bled off from the compressor stages, and fed through internal passages into components of the engine downstream which require cooling. The internal passages of the turbine blades are designed to maximize the convective heat transfer between the coolant and the turbine wall. One way this can be achieved is by using internal serpentine passages, which increase the surface area of the passage and allows the coolant to make multiple passes over the wall surfaces. Another scheme is to increase the convective heat transfer coefficient by using ribbed turbulators or impingement cooling. In addition to the convective cooling within these internal passages, film cooling is used by allowing coolant to flow over the external surface through holes machined into the wall of the airfoil. The leading edge of the turbine airfoil, which receives the greatest thermal load, is often covered by a closely spaced group of cooling holes known as the showerhead. Additional rows of holes are placed downstream on the surface of the airfoil on both the pressure and suction side. Ideally, this external film cooling forms an insulating layer of cold air attached to the airfoil surface which "shields" the engine component from the high temperatures of the mainstream combustion gas.

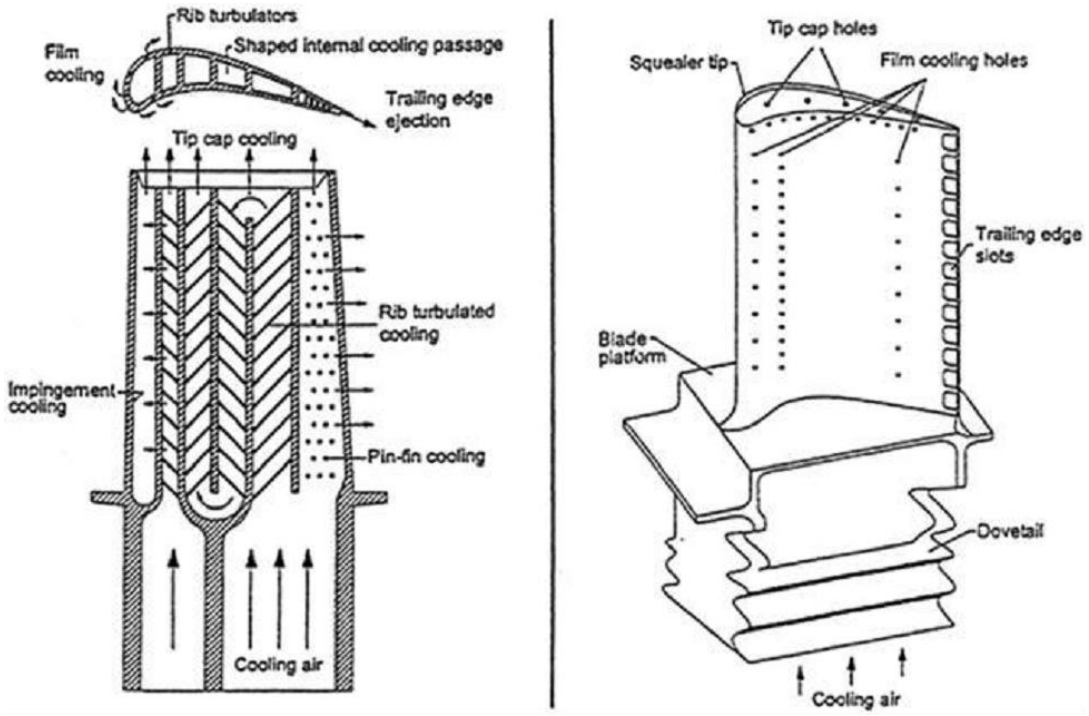

Figure 1.3: Turbine blade design featuring internal and external cooling

As much as 20-30% of the total airflow through the combustor is redirected for cooling purposes [4]. The reduction in mainstream airflow and the aerodynamic losses that result from coolant injection diminish the overall performance of the engine, and can offset the potential gains in thermodynamic efficiency produced with a higher turbine inlet temperature. Understanding how to optimize the film cooling performance, specifically the reduction in wall temperature of the cooled engine components, without an excessive use of coolant is therefore important for engine manufacturers. Research efforts on turbine film cooling are focused on using this coolant as efficiently as possible, to maximize engine durability without an undue sacrifice of performance.

1.2.1 - Important Non-Dimensional Parameters in Film Cooling

Film cooling can be described by several non-dimensional parameters, which have been shown to scale important aspects of the cooling performance such as jet mixing and separation. The density ratio (*DR*) is shown in Equation 1.3, where ρ_c is the density of the coolant and $\rho_\infty$is the density of the mainstream gas.

$$DR = \frac{\rho_c}{\rho_\infty} \tag{1.3}$$

Typical gas turbine engines operate at a density ratio of 2.0, which can be difficult to achieve in laboratory conditions. For example, all tests conducted for this study were performed at a *DR* = 1.20. Performance results at low *DR* can be related to engine conditions by matching either the velocity ratio (VR), mass flux ratio (*M*), or momentum flux ratio (*I*) [4]. It is not possible to match all of these parameters to engine conditions simultaneously, so which scaling parameter is most appropriate depends upon the aspect of film cooling being studied.

The velocity ratio scales the shear layer and turbulence production between the coolant jets and mainstream, where U_C is the average velocity of the coolant and U_∞ is the velocity of the mainstream gas.

$$VR = \frac{U_c}{U_\infty} \tag{1.4}$$

The mass flux ratio or blowing ratio (*M*) is proportional to the mass flow rate of coolant.

$$M = \frac{\rho_c U_c}{\rho_\infty U_\infty} \tag{1.5}$$

The blowing ratio is a useful parameter because it scales the thermal transport capacity of the coolant. Increasing the amount of coolant will generally improve the overall cooling performance, except in cases where the coolant jet becomes separated from the surface of the airfoil. Separation is dependent on many factors, including hole shape, local curvature, injection angle, and the difference in momentum between mainstream and coolant flows.

The relative difference in momentum between the coolant jet and mainstream flow is described by the momentum flux ratio (*I*).

$$I = \frac{\rho_c U_c^2}{\rho_\infty U_\infty^2} \tag{1.6}$$

The impact of the mainstream flow on the coolant jet tends to redirect the coolant jet back towards the surface, which has a significant effect on cooling performance. If the coolant jet becomes separated, the bulk of the coolant will be ejected into the mainstream flow and have little effect on the temperature of the wall surface.

The performance of film cooling is assessed by the reduction in the surface temperature of the turbine components receiving coolant. The heat transfer rate between the mainstream combustion products and the surface of the turbine is described by Newton's law of cooling, where T_{wall} is the temperature of the surface and T_{ref} is the driving temperature.

$$q'' = h\left(T_{ref} - T_{wall}\right) \tag{1.7}$$

The heat flux to the wall surface with and without film cooling present is shown by Equations 1.8 and 1.9 respectively.

$$q_f'' = h_f(T_{aw} - T_{wall}) \tag{1.8}$$

$$q_0'' = h_0(T_\infty - T_{wall}) \tag{1.9}$$

When film cooling is not present, the driving temperature is that of the mainstream combustion gas, T_∞. However, when film cooling is used, the temperature of the coolant is not a good descriptor of the driving temperature, because as the coolant flows over the surface it mixes with the mainstream gases. The most-commonly selected reference temperature is the adiabatic wall temperature, T_{aw}, which represents the temperature immediately above a non-conducting surface. Equations 1.8 and 1.9 can be combined into a parameter known as the net heat flux reduction (*NHFR*), which describes the overall change in heat flux into the wall surface due to the use of film cooling.

$$NHFR = 1 - \frac{h_f(T_{aw} - T_{wall})}{h_0(T_\infty - T_{wall})} \tag{1.10}$$

Film cooling usually results in a significant reduction in heat transfer to the turbine components by reducing the driving temperature above the surface. However, there can also be an increase in heat transfer coefficient due to increased turbulent mixing with the mainstream gas, which has detrimental effect on *NHFR.* The combined effects of heat transfer coefficient augmentation and driving temperature reduction need to be understood together in order to assess the performance of a particular film cooling configuration.

It is common in the literature measuring the adiabatic wall temperature to represent it in a non-dimensionalized form, known as the adiabatic effectiveness.

$$\eta = \frac{T_\infty - T_{aw}}{T_\infty - T_{c,exit}} \tag{1.11}$$

The adiabatic effectiveness is a normalized adiabatic wall temperature, which makes it easier to compare the reduction in driving temperature to the higher temperatures which would be observed in engine conditions. The coolant temperature ($T_{c,exit}$) is defined at the exit of the hole, and is also referred to as the coolant discharge temperature. The coolant and mainstream temperatures set the lower and upper bounds that would be expected for the adiabatic wall temperature, and so the magnitude of adiabatic effectiveness varies between 0 and 1. Measuring the magnitude and spatial variation of adiabatic effectiveness gives an indication of the coolant's interaction with the component surface, and makes it easy to identify areas which may not receive adequate cooling under a given film cooling configuration. In general, the film cooling performance is more sensitive to changes in adiabatic effectiveness than heat transfer augmentation. Adiabatic effectiveness (η) varies more widely with coolant injection compared to heat transfer augmentation ($\frac{h_f}{h_0}$), which typically has values near 1 [5]. For this reason, adiabatic effectiveness is more commonly studied in the literature, and is the primary testing focus of this study.

1.2.2 - Shaped Hole Effects

Since it was first studied by Goldstein et al. [6], the geometry of the cooling hole has been known to have a significant effect on the film cooling performance. Their study showed that laterally expanding the cooling hole produced higher levels of effectiveness immediately downstream of the hole exit, and promoted a greater lateral spread of coolant. Shaped holes that have a diffused exit reduce the momentum of the coolant jet as it is ejected, which inhibits the tendency of the jet to separate from the wall surface. The larger

exposed area of shaped hole exits helps the mainstream momentum in turning the coolant jet back towards the wall surface, which has a significant effect on performance.

In attempts to improve on the performance of the standard cylindrical or round cooling hole, there have been many variations of shaped hole geometries studied in the literature. However the most commonly reported shaped hole geometries are fanshaped or laidback fanshaped (LBF) holes. Fanshaped holes make use of a cylindrical metering hole which is then laterally expanded before reaching the wall surface. Laidback fanshaped holes have an additional forward expansion angle which further increases the exit area and reduces the angle of injection into the mainstream at the wall surface. A generic diagram of these three hole geometries is shown in Figure 1.4.

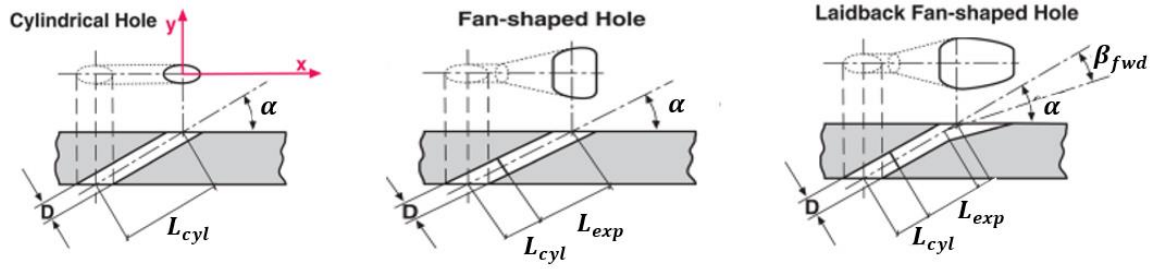

Figure 1.4: Diagram of cylindrical, fan-shaped, and laidback fan-shaped hole geometries from Saumweber and Schulz [7]

Saumweber and Schulz [7] published a study comparing the performance of cylindrical and fanshaped holes with a range of expansion angles (6°,10°, & 14° with an equal L_{exp}). Spatially averaged effectiveness measured from a range of blowing ratios from M = 0.5 to 2.5, showed that the cylindrical hole had a sharp drop in performance beyond blowing ratios of M =0.7 due to jet separation. Fanshaped holes showed a gain in cooling effectiveness relative to the cylindrical holes, which became weaker with increasing

expansion angles and stronger with increasing blowing ratios. The fanshaped hole with a 6° expansion angle had an improved performance relative to the cylindrical hole, but the spatially averaged effectiveness began to drop beyond M=1.5. As the expansion angle was increased to 10° and 14°, the peak spatially averaged effectiveness was shifted to higher blowing ratios until there was no detectable drop in performance within the range of blowing ratios investigated. Gritsch et al. [8] compared the film cooling performance of a fanshaped and laidback fanshaped hole on a flat plate over M=0.5 to 1.5. The lateral and forward expansion angles used were 14° and 15° respectively. The hole geometries were designed so that the two shaped holes had equal area ratio, AR = 3.0. The laidback fanshaped hole had a lower centerline effectiveness compared to the fanshaped hole, but the lateral spreading of the coolant was better. This lead to improved laterally averaged effectiveness values for the laidback fanshaped holes, especially at the highest blowing ratio tested.

Previous studies have developed correlations for predicting the performances of cylindrical holes, but doing so for shaped hole geometries is a more recent effort. Colban et al. [9] proposed a correlation for predicting laterally averaged adiabatic effectiveness from a single row of shaped holes on a flat plate. The correlation was developed using a number of data sets available in the literature, which included a variety of shaped hole geometries. The correlation is based on coverage (t/P), blowing ratio (M), and a scaled downstream distance (ξ) based on equivalent slot width. Equivalent slot width (S_e) is based on the expanded hole exit area. Area ratio and coverage are the only two geometric parameters used in order to account for differences in shaped hole geometry. The

correlation forces the laterally averaged effectiveness to match the coverage value at x/D=0, which represents the ideal limit of a single row of discrete holes. The correlation form is shown in Equation 1.12.

$$\bar{\eta} = \frac{1}{\frac{P}{t}+C_1 M^{C_2} \xi^{C_3}} \text{ , where } \xi = \frac{X}{M*S_e} = \frac{4*\frac{X}{D}*\frac{P}{D}}{\pi*M*AR} \tag{1.12}$$

1.2.3 - Effects of Wall Curvature

The curvature of a turbine airfoil can have a significant effect on the tendency of the coolant jet to remain attached to the wall surface, due to the presence of a pressure gradient normal to the wall surface. Ito et al. [10] measured the effect of curvature on a gas turbine blade on film cooling effectiveness. They concluded that the trend of jet trajectory can be explained by considering the balance of the forces exerted on the injected fluid by the static pressure and the centrifugal force along the path of the injected fluid. For low momentum flux ratios, the pressure gradient on a convex surface will cause the coolant jet to be turned back towards the wall. As the coolant jet momentum begins to exceed that of the mainstream, the radius of curvature of the coolant jet will exceed that of the mainstream, and the jet will move away from the wall. Compared to flat plate results, the film cooling performance on convex surfaces will increase at low momentum flux ratios, and decrease at high momentum flux ratios. The opposite trend holds true for concave surfaces.

Lutum et al. [11] performed a study of fanshaped and laidback fanshaped hole geometries on a convex surface ($\frac{2R}{D} = 50$), and compared the influence of external pressure

gradient and Mach number on film cooling performance. They concluded that for low and moderate bowing ratios, M<1, the film effectiveness was increased on convex surfaces relative to flat surfaces. Free-stream acceleration generally decreased adiabatic effectiveness relative to a zero pressure gradient flow, although increased adiabatic effectiveness could be obtained in the near-hole region due to the reduced tendency of jet separation in the accelerated free-stream. Zhang and Moon [12] measured the adiabatic effectiveness of three rows of laidback fanshaped holes located on the pressure side of a turbine blade with concave curvature. They found that the average film effectiveness for the downstream single row injection was higher at the same blowing ratio than the other two upstream rows in areas of higher concave curvature. The results of these two studies are consistent with the expected effect of convex/concave curvature on the film cooling performance as outlined by Ito et al.

1.2.4 – Effects of Increased Mainstream Turbulence

Saumweber et al. [13] performed a study on the effects of increasing mainstream turbulence levels on both cylindrical and laidback fanshaped holes on a flat plate. Laterally averaged adiabatic effectiveness results were compared at M=0.5-2.5 over a range of turbulence levels (Tu = 3.6, 7.5, 11%). For cylindrical holes, increased turbulence was detrimental at low blowing ratios and beneficial at high blowing ratios. For shaped holes, increased turbulence intensity was detrimental for all blowing ratios tested, but the effect was most pronounced at low blowing ratios. Liu et al. [14] reported a similar result for laidback fanshaped holes tested from M=0.5-2.0 at Tu = 0.5% and 13%. The film cooling

effectiveness was significantly reduced by higher mainstream turbulence at low blowing ratios, but the effect became negligible at the highest blowing ratio. Increased mainstream turbulence levels can have a positive or negative effect on the film cooling performance depending on the shape of the coolant hole and the attachment of the coolant jet to the wall surface. High turbulence intensifies mixing of the coolant with the mainstream gas, which can actually improve the film cooling if the coolant jet is already separated. In addition, high turbulence increases the lateral spreading of the coolant. In general, the potential benefits of high mainstream turbulence do not come into effect with shaped holes. Shaped holes which are sufficiently expanded do not have any tendency to detach even at high blowing ratios. The lateral expansion of the shaped hole has a much more pronounced effect on the lateral spreading of the coolant than any spreading which would be caused by an elevated free-stream turbulence intensity.

1.3 - Full Coverage Film Cooling

1.3.1 - Full Coverage Configurations on a Turbine Vane with Shaped Holes

Studies of shaped holes have generally demonstrated an improved performance compared to cylindrical holes. However, the design of an optimal full coverage configuration on a turbine vane remains a difficult task because the row-to-row interactions between shaped holes are not well understood, as is the influence of showerhead cooling. Guo et al. [15] studied the adiabatic effectiveness on a full coverage nozzle guide vane with axial laidback fanshaped holes using the transient liquid crystal technique. On the suction side, they found that the shaped holes produced a higher level of effectiveness than

compared to cylindrical holes. A different trend was observed on the pressure side, where shaped holes initially outperformed round holes, but had a much faster decay of effectiveness as the coolant moved downstream. In another paper, Gao et al. [16] studied a fully cooled turbine blade with axial laidback fanshaped holes using the pressure sensitive paint technique. They observed longer and more distinct coolant traces on the suction side compared to the pressure side, which resulted in a higher level of laterally averaged effectiveness even with a fewer number of rows of holes providing cooling. A similar result was found by Mhetras and Han [17] who studied a fully cooled turbine blade with compound angle laidback fanshaped holes. Gao et al. found that the film cooling effectiveness increased with increasing averaged blowing ratio in the range of their study (M=0.3 to 1.2), although they tested a lower range of blowing ratios than is typical for shaped holes. Colban et al. [18], who tested much higher blowing ratios (M=0.9 to 4.8) on a scaled turbine blade with axial laidback fanshaped holes, found that increasing blowing ratio tended to accentuate jet liftoff on both the pressure and suction sides, reducing the overall performance.

1.3.2 - Downstream Effects of Showerhead Cooling

When comparing results with and without showerhead cooling, the additional downstream cooling provided by the showerhead makes it difficult to isolate the performance of rows further downstream. However, comparisons of the overall effectiveness can still assess which configuration has the better performance. The effects of showerhead cooling on the film cooling performance downstream has been studied for

both round and shaped holes. Polanka et al. [19] studied the effects of showerhead cooling for the first pressure side row of round holes downstream of the showerhead. They found that the primary effect of showerhead injection was to increase turbulence levels of the approach flow, which resulted in increased coolant dispersion. This has a negative effect at low blowing ratios, but can actually improve performance at higher blowing ratios where a coolant jet might experience separation by redirecting more of the coolant back towards the wall surface. Colban et al. [18] studied the effect of showerhead cooling on the first pressure side row with axial laidback fanshaped holes, and found a similar result. The presence of upstream coolant tended to increase the turbulent diffusion of the downstream jet, resulting in more coolant being dispersed back towards the surface and improving performance. Gao et al. [16] also compared the cases with and without showerhead cooling for full coverage turbine blade with axial laidback fanshaped holes. They found that showerhead cooling improved the laterally averaged effectiveness on both the pressure and suction sides. Kinell et al. [20] reported a similar improvement in effectiveness due to showerhead cooling on a turbine vane with similarly shaped axial laidback fanshaped holes. However they found there was also an enhancement in heat transfer coefficient which would have a negative impact on the net heat flux reduction.

1.4 - Objectives of the Current Study

Adiabatic effectiveness measurements have been conducted for a full coverage film cooling configuration on a scaled turbine vane model featuring cylindrical and laidback fanshaped holes. Tests were performed under a wide range of blowing ratios, and a

comparison was done at low and high levels of mainstream turbulence, Tu = 0.5% and 7.5%, respectively. The vane model studied makes use of an endwall and adjustable sidewalls to match the pressure distribution at engine conditions. The cooling hole configuration consisted of five rows of cylindrical holes in the showerhead region, six rows of laidback fanshaped holes on the pressure side, and four rows of laidback fanshaped holes on the suction side. Results from this study are presented in terms of laterally-averaged adiabatic effectiveness. The vane model was tested in several different coolant configurations, including individual rows on the pressure and suction side, and full coverage tests with and without showerhead cooling. Comparisons between these configurations were made in order to assess the effects of local curvature, showerhead cooling, and mainstream turbulence levels.

Chapter 2 – Experimental Methods and Test Facility

2.1 - CLOSED LOOP WIND TUNNEL

All tests in this study were performed in a closed loop wind tunnel facility at the Turbulence and Turbine Cooling Research Laboratory at the University of Texas at Austin, shown in Figure 2.1. The mainstream flow is driven by a 50HP variable-pitch single stage axial fan, and is maintained at a constant temperature by a water-fed, fin-coil heat exchanger. The mainstream flow passes through a conditioning screen downstream of the fan, and enters a 4:1 contraction nozzle before passing through the test section.

2.1.1 - Secondary flow loop

All the experiments in this study were run at a density ratio of 1.2, in order to prevent the formation of frost which is difficult to control at higher DR. In order to create this density difference between coolant and mainstream flows, a portion of the mainstream was extracted into a secondary flow loop, shown below in Figure 2.2. The extracted flow then entered a heat exchanger supplied with liquid nitrogen fed from 160L Dewar flasks. Desiccants packs were placed in the tunnel before each test in order to keep humidity level low during operation, usually under 5% RH. This was critical to prevent frost formation during experiments. The vane model had three separate coolant passages which were fed by inlet ducts cast with the same interior profile to ensure uniform flow. Gate valves controlled the flow rates into these passages, and orifice flow meters installed upstream of these valves gave measurements of the amount of coolant entering each passage.

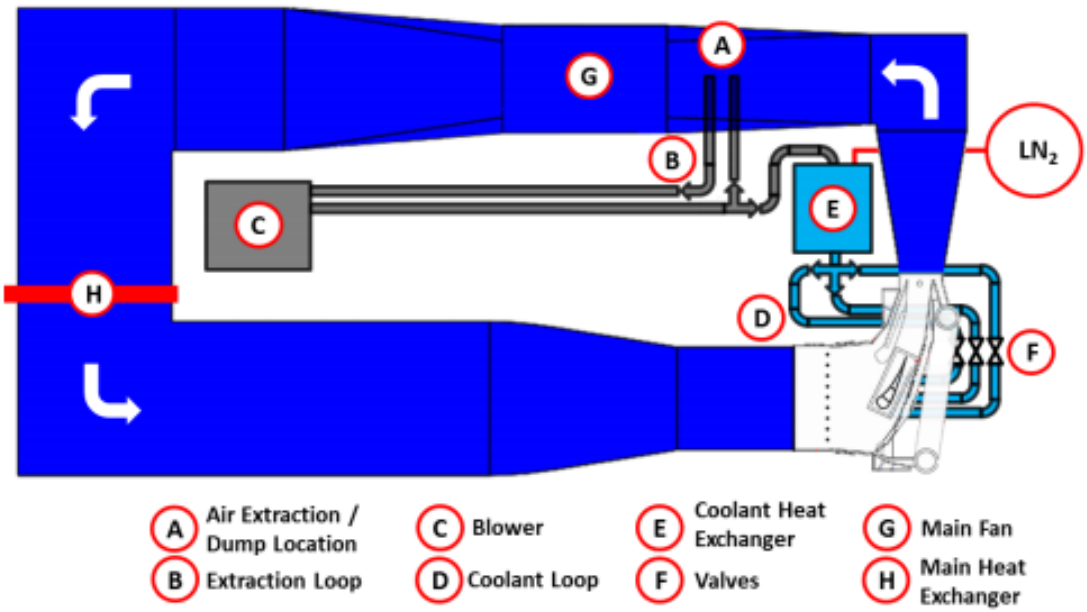

Figure 2.1: Schematic of closed loop wind tunnel facility [21]

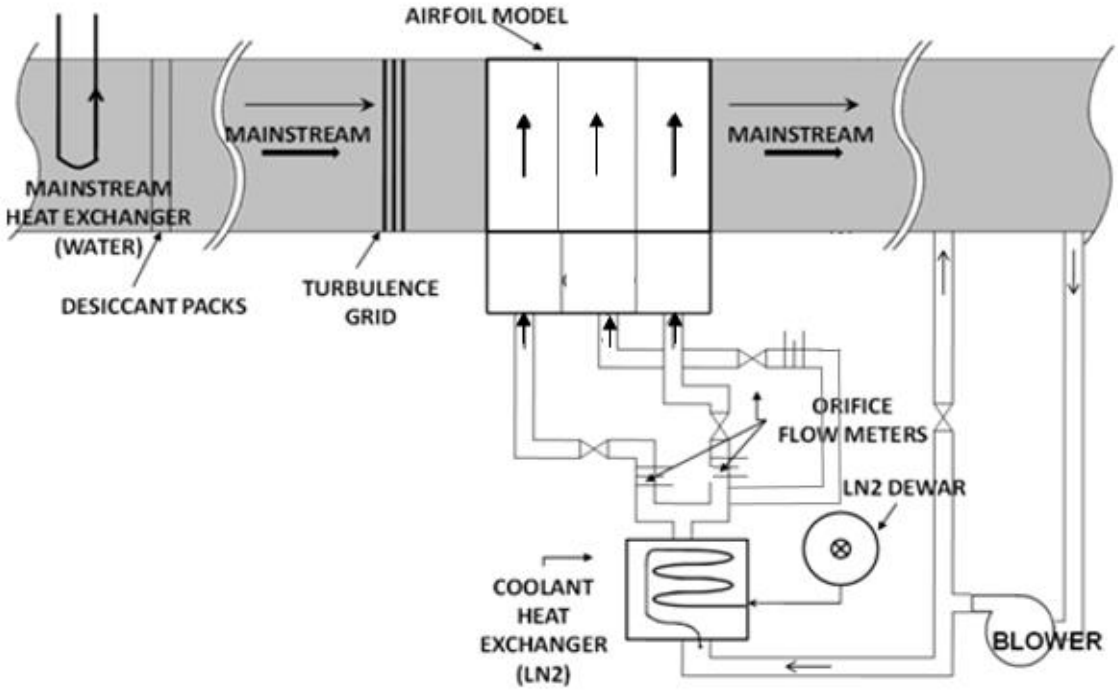

Figure 2.2: Schematic of secondary coolant flow loop [21]

2.1.2 - Model Test Section

The test section, shown in Figure 2.3, holds a three vane linear cascade with a 560 x 1020 mm inlet. The cascade has a removable test vane used for experimental measurements. Flow bypasses were used to set the location of the stagnation point on the leading edge of the test model. The test section has outer sidewalls which are adjustable. Another unique feature of this test section is the use of a contoured endwall, which accelerates the flow downstream of the vane model and allows the pressure distribution to more closely match engine conditions. For some tests, a turbulence grid was placed across the entrance of the test section to raise the average turbulence levels from 0.5% to 7.5%. More detail on the construction of that grid, and the assessment of the resulting turbulence profile is provided in the next section. Several salt crystal (NaCl) window ports were installed into the acrylic walls of the test section to allow for infrared imaging of the test vane model.

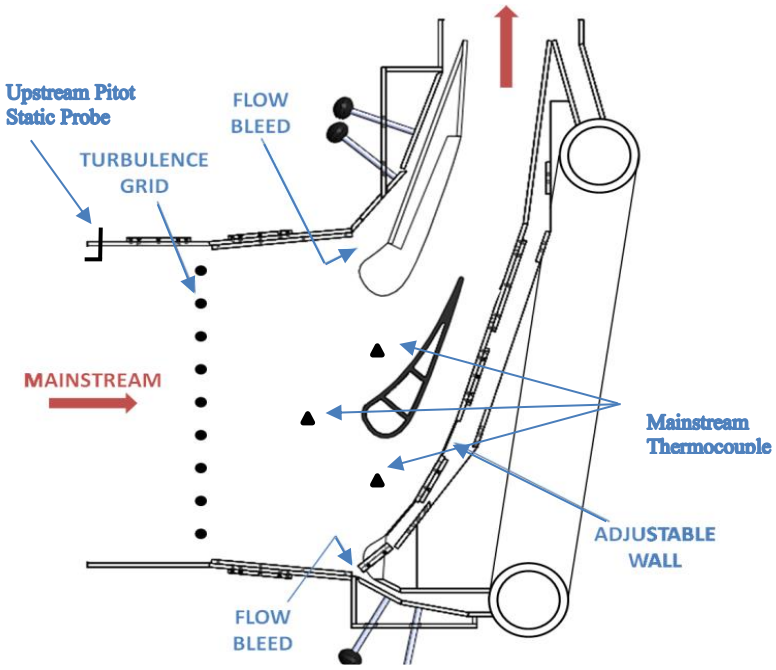

Figure 2.3: Model vane test section [21]

2.1.3 - Mainstream Turbulence Levels and Turbulence Grid Design

Previous measurements by members of the TTCRL have found a low mainstream turbulence level (Tu) of 0.5% when the closed loop wind tunnel is operated with no turbulence grid in place [21]. A new turbulence grid was designed with the intended goal of generating a turbulence level of 10% at a distance of 0.2*C_{ax} upstream of the leading edge. A correlation previously developed by Mosberg [22] for predicting turbulence levels is shown as Equation 2.1, where A = 0.8, x_f is the downstream distance, and b is the rod diameter.

$$Tu\ \% = A\left(\frac{x_f}{b}\right)^{\frac{5}{7}} \tag{2.1}$$

The turbulence grid was constructed with ½" diameter aluminum rods, and mounted with horizontal steel sheets to provide structural support and reduce deflection. Springs were added to the ends of some rods to help secure the grid in place, in addition to some safety wires attached through the tunnel ceiling. A solidity of 50% was selected because tighter rod placement caused wakes to merge more quickly and produced a more uniform turbulence downstream of the grid.

A verification of the turbulence profile was done with hot-wire anemometry, using an A.A. Lab System AN-1003 test module connected to a 5μm hot-wire probe. A traverse system was used to measure the mean mainstream velocity and its standard deviation over a full pitch span across the tunnel. Hot-wire measurements found the pitch averaged turbulence level to be 7.5%, with a peak intensity of 10% measured at the stagnation line (x/P = 0). The profiles of turbulence levels, mean velocity, and RMS velocity are shown in Figures 2.4-6. The lateral variation in mainstream velocity, and therefore turbulence levels, is due to upstream effects caused by the hot-wire probe's proximity to the vane model. The mainstream flow is decelerated upstream of the leading edge of the vane model, and is accelerated through the cascade passage.

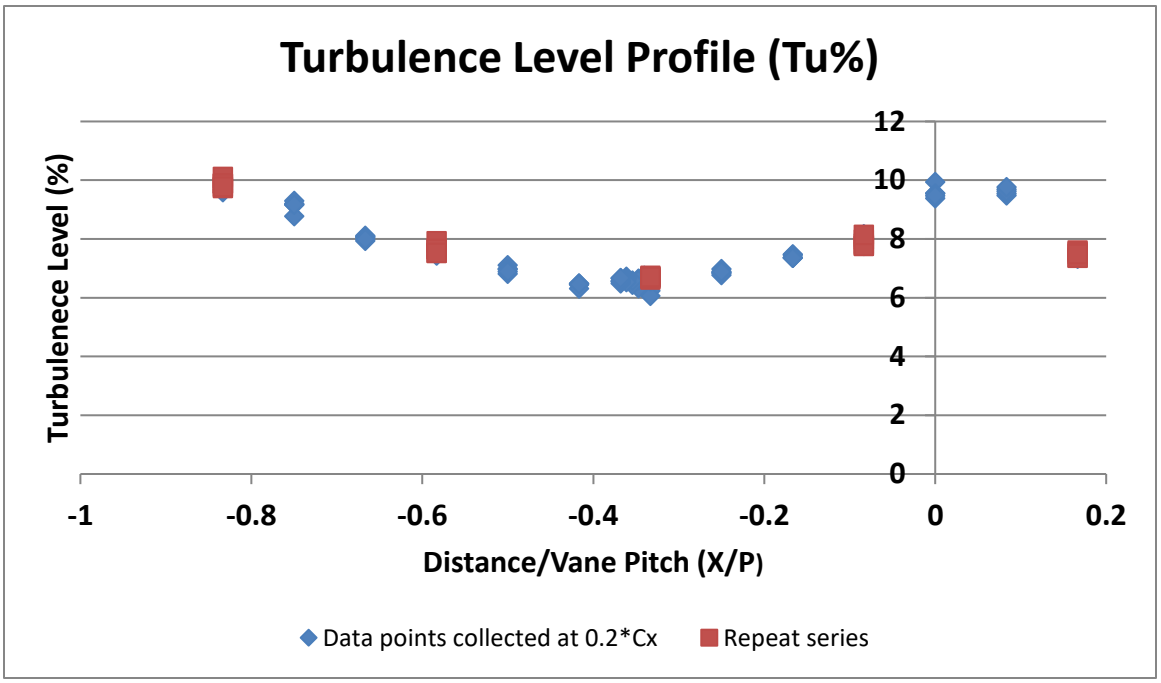

Figure 2.4: Turbulence profile measured 0.2*C_{ax} upstream of the leading edge

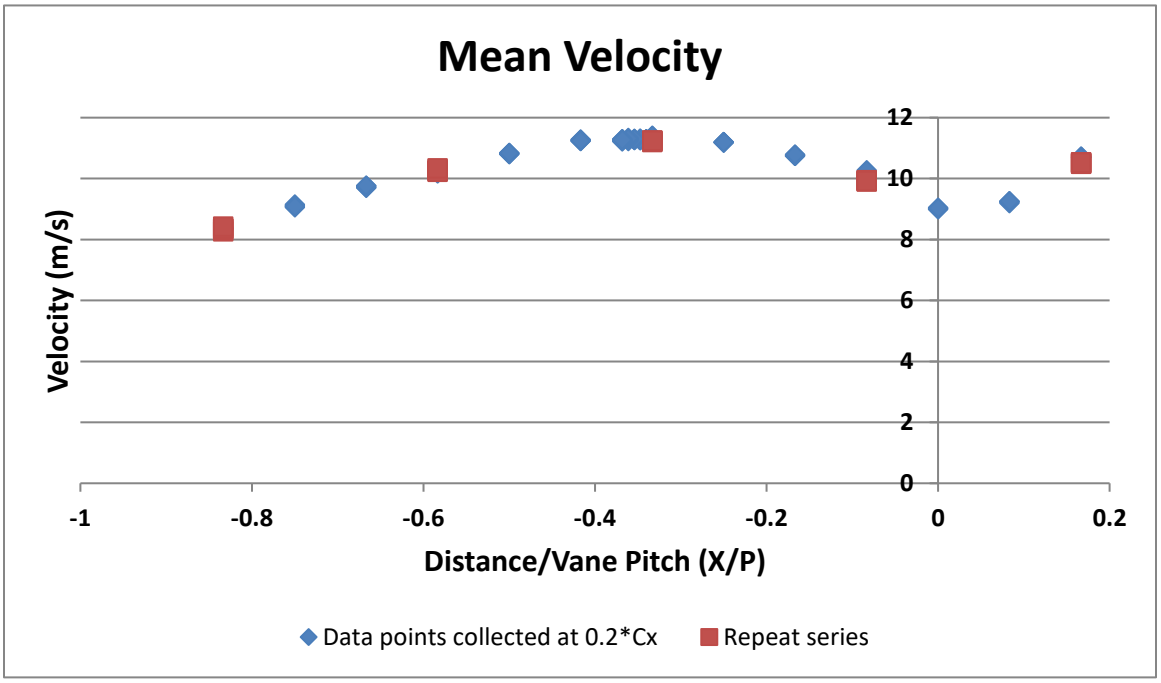

Figure 2.5: Mean velocity profile measured 0.2*C_{ax} upstream of the leading edge

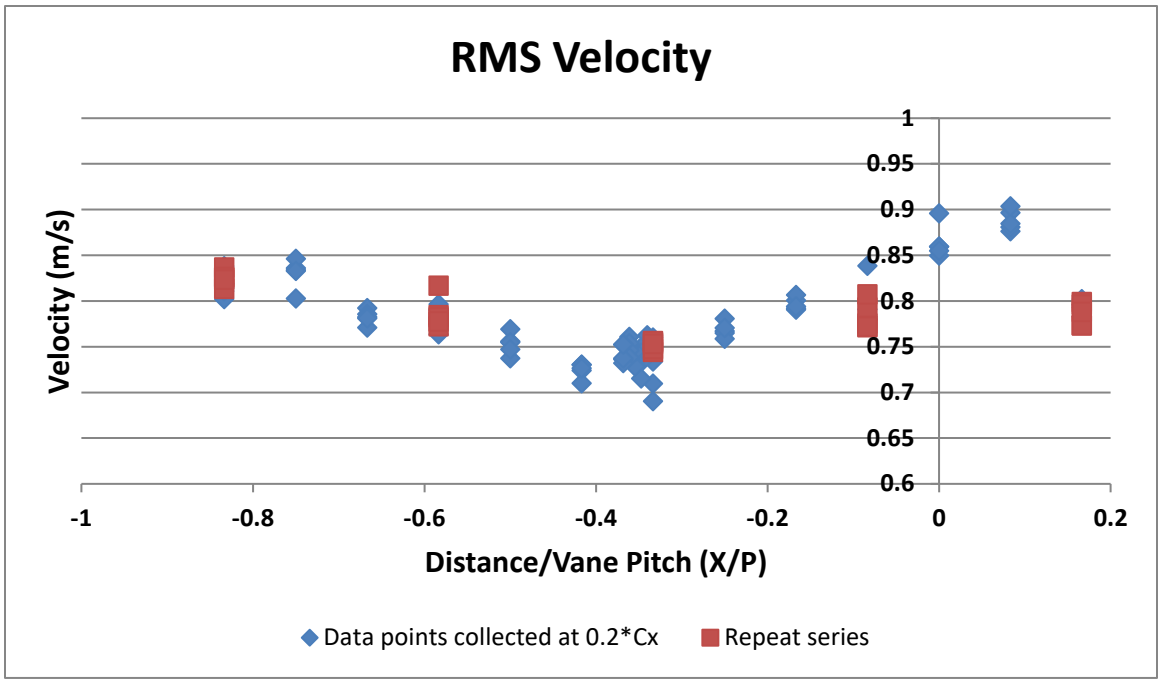

Figure 2.6: RMS velocity profile measured 0.2*C_{ax} upstream of the leading edge

2. 2 - Model Vane Description

The scaled turbine vane model was constructed using a low thermal conductivity polystyrene foam (k = 0.048 W/m*K) which limited the amount of through-wall conduction during adiabatic effectiveness testing. The film cooling holes for the test vane were machined into five removable hatches, which were sealed into place with vacuum grease, weather stripping, and spackle. Both the hatches and the vane model body were sanded and then painted with a flat black Kyrlon camouflage spray paint to provide a uniform surface with a constant emissivity. Once painted, the area of the model vane being imaged was outlined with an aluminum-based paint which provided a contrast in emissivity visible to the IR cameras. These lines would be used to obtain a spatial correlation between

camera pixels and the actual locations on the model surface, which is described in a later section.

The fully cooled configuration featured 15 rows of film cooling holes: 5 rows of cylindrical holes (Rows 7-11) in the showerhead and 10 rows of laidback fanshaped holes (LBF) (Rows 1-6 & 12-15) distributed around the pressure and suction side of the model. All of the laidback shaped holes were axially oriented with the streamwise flow, while the cylindrical holes in the shower head used a compound angle of 90°. Figure 2.7 shows the approximate locations of the individual rows on the airfoil model, and which coolant channel each row was fed by. Channels 1, 2, 3 are also referred to as the back, middle, and front coolant passages respectively.

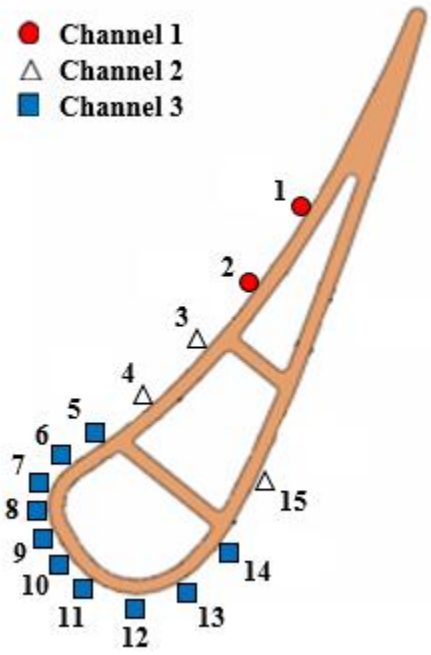

Figure 2.7: Schematic of vane coolant channel configuration

2. 3 - INSTRUMENTATION

2.3.1 - Data Acquisition System

All data acquisition for pressure and temperature measurements was accomplished with hardware from National Instruments, specifically NI-SCXI-1300 and NI-SCXI-1303 DAQ modules. The computer managed the data collection process through an in-house LabVIEW script developed over several years by previous members of the lab. Measurements were read at a data rate and duration specified by the user. Samples for this study were collected at a rate of 400Hz, averaged over 5 seconds. Sampling at this rate and duration sufficiently reduced the precision uncertainty during testing below the levels needed to get useful measurements, typically less than 0.1% of the measurement value.

2.3.2 - Thermocouples

All gas temperature measurements were made with Type-E welded-junction or soldered-junction thermocouples. In replacement of the standard NIST calibration for E-type thermocouples, all of the thermocouples used in this study were individually calibrated against a high accuracy thermistor contained within a glycol water bath, an example of which is shown in Figure 2.8. The average accuracy of this type of calibration, which is described in more detail in the next chapter on uncertainty analysis, was around ±0.17K.

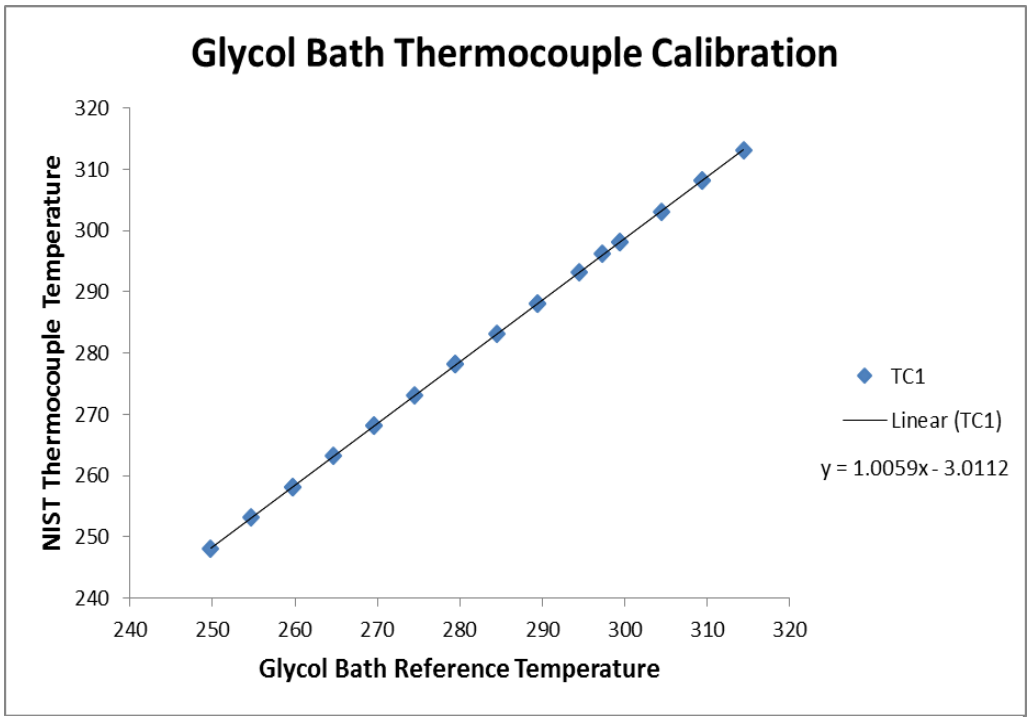

Figure 2.8: Example of glycol bath thermocouple calibration

2.3.3 - Pressure Transducers

All pressure measurements necessary to calculate the flow rate of coolant in the secondary flow loop were made with pressure transducers manufactured by Omega (model P2650-xxx5V). Pressure transducers with pressure ranges including 0-125 Pa, 0-500Pa, -1200Pa-1200Pa, and 0-5000Pa were used based on their specific measurement task. Each transducer output was connected to an unique input in the data acquisition system, so that bias errors in the DAQ system could be accounted for in their calibrations. Calibrations creating a linear fit for applied pressure to voltage output were performed using a Meriam A-1087 micromanometer by Chavez in 2015 [23]. It was assumed that the slope of the

calibrations remained constant in between the original calibrations and testing, but there was a minor adjustment of the y-intercept (~0.01 Pa) to account for drifting in the zero pressure reading. A list of the pressure transducers and their calibrated accuracies is shown in Table 2.1.

Table 2.1: List of pressure transducers and their locations in this study

Transducer	Range	Location	Calibrated Accuracy	Omega Model No.
PT E	0 – 0.5 inAq 0 – 124.4 Pa	Approach Flow Pitot-Static Probe	0.005 inAq 1.18 Pa	PX2650 0.5D5V
PT 403	+- 2 inAq +- 497 Pa	Mainstream Static Pressure	0.014 inAq 3.48 Pa	PX2650 2BD5V
PT X	0 – 2 inAq 0 – 497 Pa	Back Passage Orifice Differential Pressure	0.04 inAq 0.99 Pa	PX653- 02D5V
PT G	0 – 2 inAq 0 – 497 Pa	Middle Passage Orifice Differential Pressure	0.07 inAq 1.77 Pa	PX2650 2D5V
PT 414	+- 5 inAq +- 1244 Pa	Front Passage Orifice Differential Pressure	0.028 inAq 6.92 Pa	PX2650 5BD5V
PT 428	+- 2 inAq +- 497 Pa	Back Passage Plenum Differential Pressure	0.051 inAq 12.58 Pa	PX2650 2BD5V
PT 402	+- 5 inAq +- 1244 Pa	Middle Passage Plenum Differential Pressure	0.016 inAq 3.99 Pa	PX2650 5BD5V
PT 401	+- 5 inAq +- 1244 Pa	Front Passage Plenum Differential Pressure	0.013 inAq 3.27 Pa	PX2650 5BD5V
PT 408	0-25 inAq 0-6221 Pa	Upstream Coolant Pipe Differential Pressure	0.056 inAq 13.96 Pa	PX2650 25D5V

2.3.4 - Mainstream Temperature and Velocity Measurements

The mainstream temperature was averaged between three thermocouples mounted approximately 5 cm above the floor of the tunnel. One thermocouple was placed on either side of the vane model to account for differences between pressure and suction side

temperatures, and the third was placed upstream of the model in line with the stagnation point, as shown in Figure 2.3. The differences between these three thermocouples were small, typically between 0.2 and 0.5K. The average mainstream temperature of the tunnel during operation was 305K.

An upstream Pitot-static tube was placed approximately 1m upstream of the test section, downstream of the contraction nozzle. The mainstream velocity can be calculated from a Pitot-static probe by using the Bernoulli equation, shown in Equation 2.2. ΔP_{dyn} is the dynamic pressure, and ρ_∞ is the density of the mainstream gas which was approximated by using the local atmospheric pressure reported by the National Weather Service at nearby Camp Mabry, Austin, TX.

$$U_\infty = \sqrt{\frac{2\Delta P_{dyn}}{\rho_\infty}} \tag{2.2}$$

Equation 2.3 was used to account for changes in atmospheric pressure due to elevation, where $P_{atm,0}$ is the equivalent sea level pressure reported by the weather station, $L = 0.0064\ K/m$ is the temperature lapse rate, h is the lab altitude (182m), T is the lab temperature, g is the gravity, M is the molar mass of dry air, and R is the universal gas constant. Adiabatic effectiveness measurements were made with the tunnel operating at 11.0 m/s.

$$P_\infty = P_{atm,0}\left(1 - \frac{Lh}{T + Lh}\right)^{\frac{gM}{RL}} \tag{2.3}$$

The operating conditions used throughout the adiabatic effectiveness tests are summarized in Table 2.2

Table 2.2: Experimental Parameters used for Adiabatic Effectiveness Testing

Experimental Parameter	Value and tolerance
Mainstream Temperature	305 ± 0.44 K
Mainstream Velocity	11.0 ± 0.05 m/s
Turbulence Level	0.5, 7.5 ± 0.1%
Average Coolant Temperature	250 ± 0.17 K
Density Ratio	1.20 ± 0.002
Chord Reynolds Number	226,000 ± 1000

2.3.5 - Coolant Loop Flow Rate and Temperature Measurements

The mass flow rate through an obstruction-type flowmeter is given by Equation 2.4.

$$\dot{m} = A_t \frac{C_d}{\sqrt{1-\beta^4}} \sqrt{2\rho_c \Delta P_{static}} \tag{2.4}$$

The discharge coefficient (C_d) of the orifice plate was previously determined by a laminar flow element calibration done by Chavez in 2015 [23]. β is the ratio of orifice plate to pipe diameter. Orifice meters used for the back, middle, and front passages had values of β = 0.33, 0.55, and 0.71 respectively. The temperature of the coolant flowing through the orifice meters was measured in order to calculate the coolant density (ρ_c) at the flowmeter used in the mass flow rate equation.

The coolant temperatures of each passage were measured at the entrance of the coolant plenum. It was necessary to measure the coolant temperatures individually for each passage because of the large difference in flow rates tested. An average coolant temperature of 250K between the three channels was targeted during testing in order to produce an

average density ratio of 1.20. A thermocouple was also placed at the top of each passage within the vane in order to give an indication of how much the coolant had warmed while flowing through the vane.

2.3.6 - Calculating the Film Cooling Hole Discharge Coefficients

The discharge coefficient for the cylindrical holes in the showerhead were assumed to be a constant of $C_{d,row} = 0.69$, based on previous measurements of discharge coefficient of inclined round holes in a showerhead performed by members of this lab [24]. Measurements of discharge coefficient for most of the rows of shaped holes were performed by Chavez in 2015 [23]. The following equation from Gritsch et al. [25] was used to calculate the discharge coefficient for each row of shaped cooling holes.

$$C_{d,row} = \dot{m}_c / \left(A_{c,row} P_{t,c} \left(\frac{P_{\infty,local}}{P_{t,c}}\right)^{\frac{\gamma-1}{2\gamma}} \sqrt{\frac{2\gamma}{(\gamma-1)RT_{t,c}} \left[\left(\frac{P_{t,c}}{P_{\infty,local}}\right)^{\frac{\gamma-1}{\gamma}} - 1\right]}\right) \quad (2.5)$$

Using a row averaged discharge coefficient has some benefit from an uncertainty standpoint, due to an increased mass flow rate (through a whole row versus a single hole) and removing any small variations in hole-to-hole diameter by using an average metering hole diameter.

2.3.7 - Calculating the Fractional Mass Flow rate Through Multiple Rows of Holes

In order to calculate the fractional flow split among each row within each coolant passage, the measured discharge coefficients from each passage were used to calculate the functional relationship between every row in a passage and the internal pressure of that

channel, in the form of a fourth order polynomial. The resulting fractional flow rates used for the full coverage tests are shown versus the total channel mass flow rate for the front and middle passages in Figure 2.9-10. Because the discharge coefficients were never measured for row 1, a 50-50 split between rows 1 and 2 was assumed for the coolant entering the back passage channel. At the lowest flow rates, small bias errors due to low pressure readings across the orifice plate could lead to fractional mass flow rates that did not sum to 100%, but were usually within 1-2%. The bias error at very low pressures were assumed to be equal across all rows within a passage, and the fractional flow rate equation was renormalized to ensure that fractional flow rates would always sum to 100%.

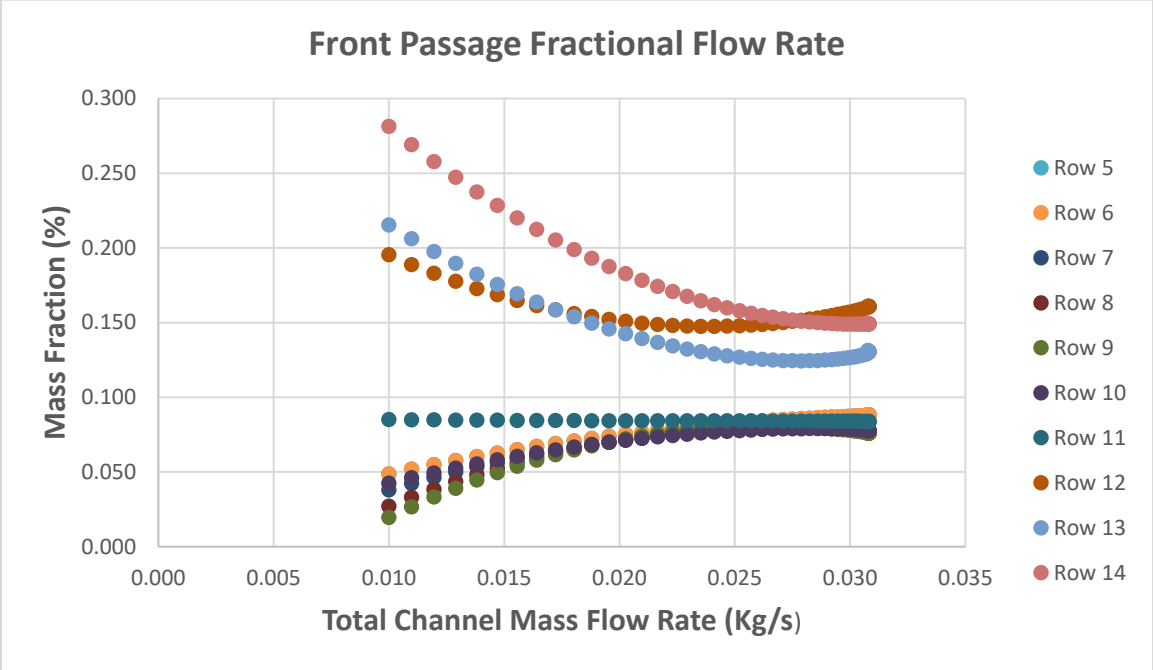

Figure 2.9: Fractional flow rate for the front passage during full coverage testing

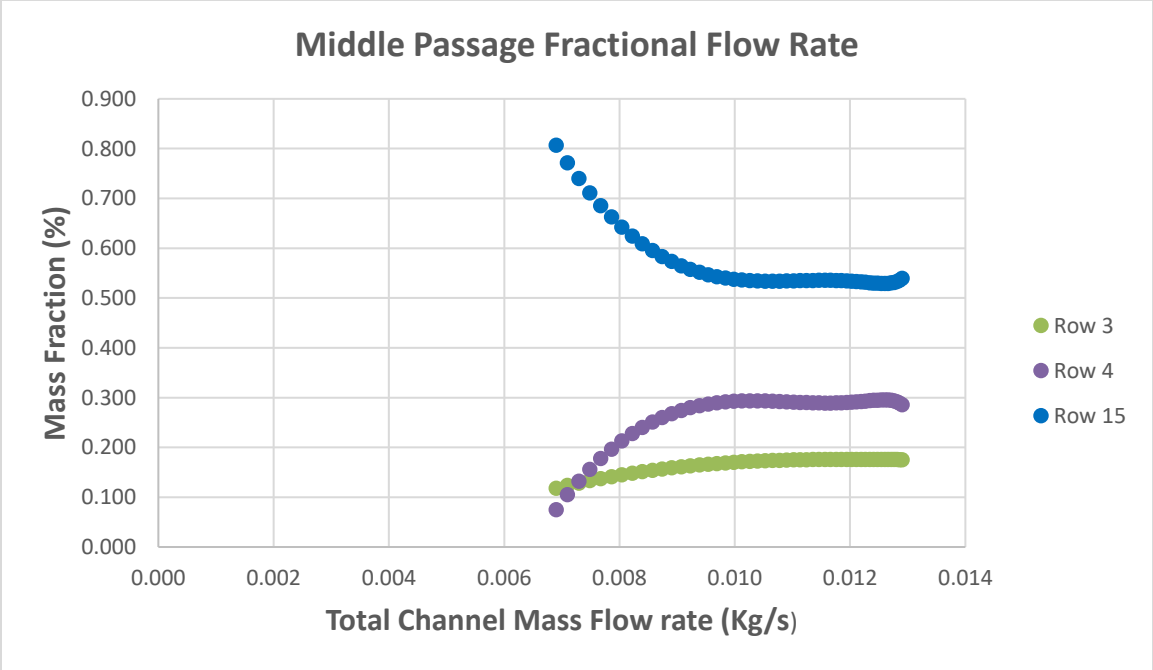

Figure 2.10: Fractional flow rate for the middle passage during full coverage testing

2.4 - IR THERMOGRAPHY

Surface temperatures were measured by five FLIR IR cameras (P20, T620, SC325, and two AC655 models) positioned to cover the full span of the test model (Figure 2.11-12). The resolution of the T620 and AC655 cameras was 640 by 480 pixels, while the resolution of the P20 and SC325 cameras was 320 by 240 pixels. Several salt crystal (NaCl) windows were positioned in the acrylic walls of the test section to provide optical access. During testing, images would be taken manually, simultaneously with measurements of the relevant temperature and pressure data recorded on the data acquisition system. The process would be repeated through five rounds of data collection, producing 25 pairs of images and measurement samples for each operating condition. A software package for handling most of the required post-processing of this data was developed in Matlab by Chavez [21]. An extensive discussion of this software can be found in his dissertation, although some of the key sub-processes have been described in the following sections.

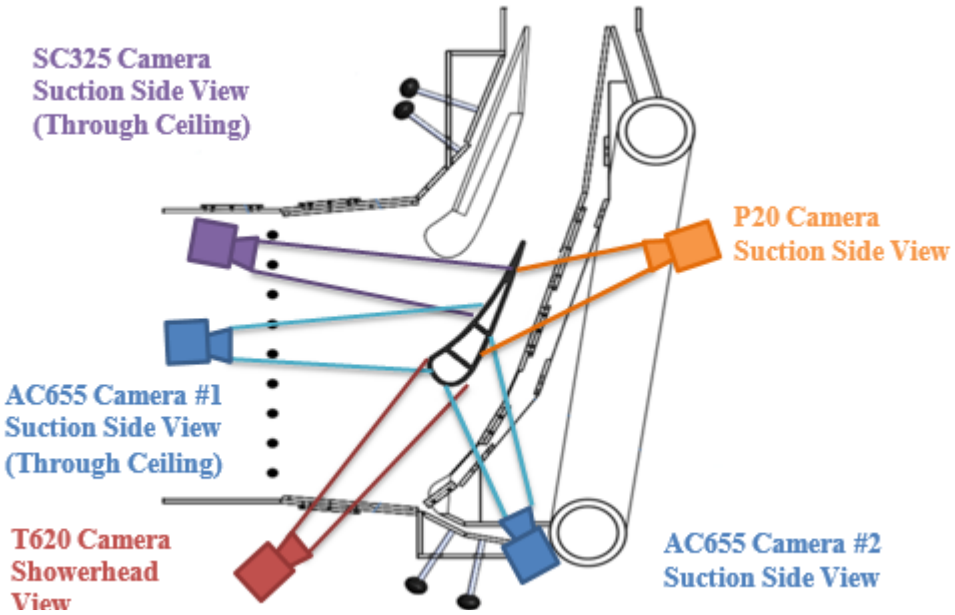

Figure 2.11: Schematic of IR camera configuration around test section

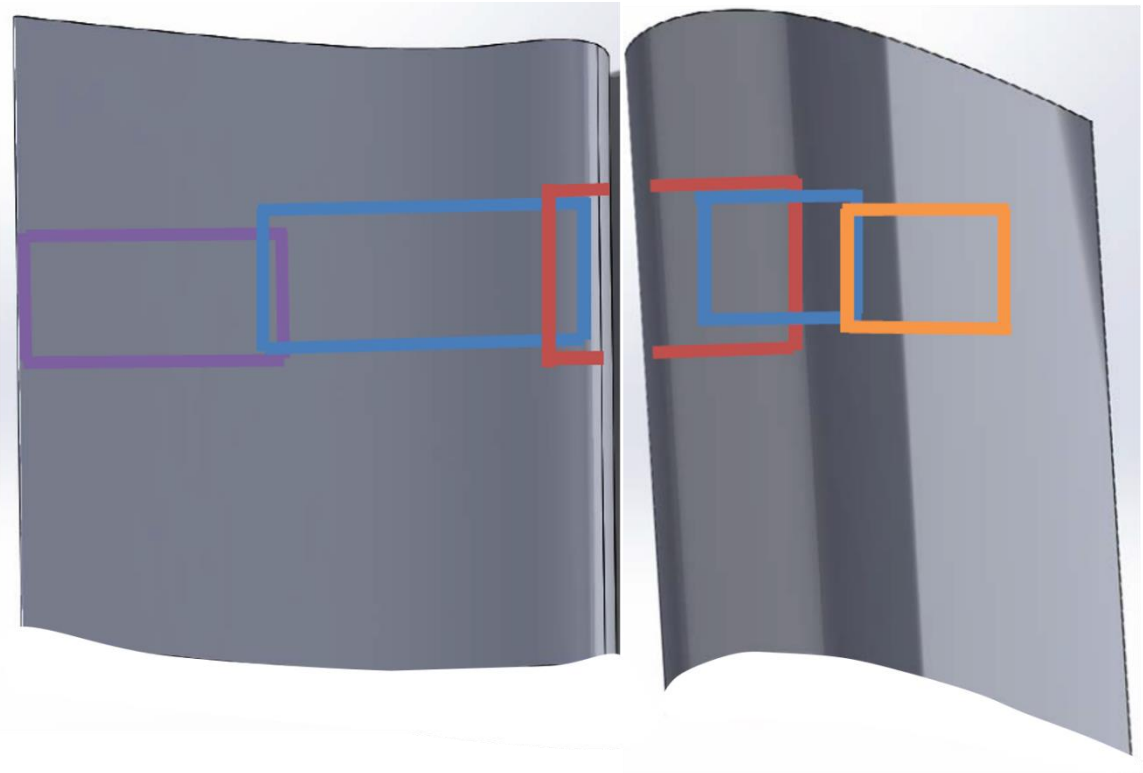

Figure 2.12: Approximate viewing areas used on the pressure and suction sides of the model vane

2.4.1 - Spatial Correlation

In order to account for curvature and the viewing angle of each camera, a spatial correlation was needed to transform the pixel coordinates of the IR images from each camera into streamwise (S) and spanwise (Z) coordinates. A Matlab script was developed for this purpose by Chavez [21], which utilizes a pinhole camera model and a direct linear transformation (DLT) as discussed by Hartley and Zisserman [26].

A series of locating lines were painted with a low emissivity, aluminum based paint along the viewable area of the airfoil surface. These lines were drawn parallel to the streamwise direction of flow, spaced an integer number of pitches apart spanwise, and marked every quarter inch. After establishing the camera positions, the user manually records the pixel locations for each fiducial mark using FLIR's proprietary software, *ThermaCAM Researcher 2002*. Having measured the locations of the fiduciary marks on the vane model, the 3D real world location of each mark is also known from the geometry of the airfoil.

The DLT algorithm was used to convert the 3D real world fiduciary mark locations onto the 2D IR image plane, which lets the user verify the transformation operation. Those results were then used to convert the same data onto the 2D S- and Z- coordinates for further processing. An example of a raw IR image converted to the non-dimensional coordinate system is shown in Figure 2.13. When this process was repeated for the full set of images associated with each camera, the camera information can be combined into a continuous set of temperature data in the S-and Z- coordinate system, contained in a single variable in the Matlab workspace memory.

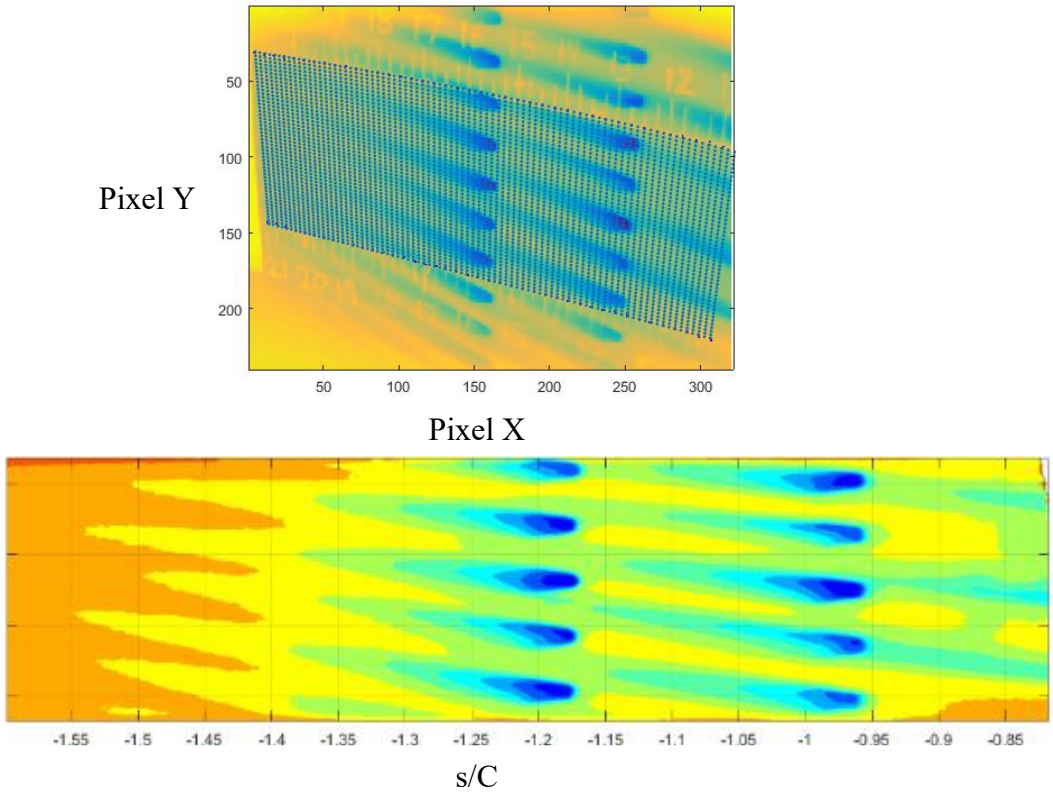

Figure 2.13: A raw IR image (top) showing the user-selected locating lines, and the same image (bottom) converted to the S- and Z- coordinate system

2.4.2 - Spatially-Dependent IR camera temperature calibration

Previous investigations in this lab have demonstrated the need for a spatially-dependent IR temperature calibration, especially in regions with high curvature like the showerhead. An in-situ calibration was performed for each camera to account for the cumulative effects of surface emissivity, IR window transmissivity, local curvature and camera viewing angle. To obtain this calibration, E-type gas probe thermocouples were made into modified surface thermocouples by epoxying the thermocouple junction to the underside of a thin, copper tab, which was then painted with the same paint as the test

model on the opposite side (Figure 2.14). An aluminum-based silver paint was drawn on the top of the thermocouple because the contrast in emissivities made it easier to identify the thermocouple tabs within the IR images. These modified surface thermocouples provided an area of uniform temperature around the thermocouple, which was then affixed to the surface of the model with electrical tape.

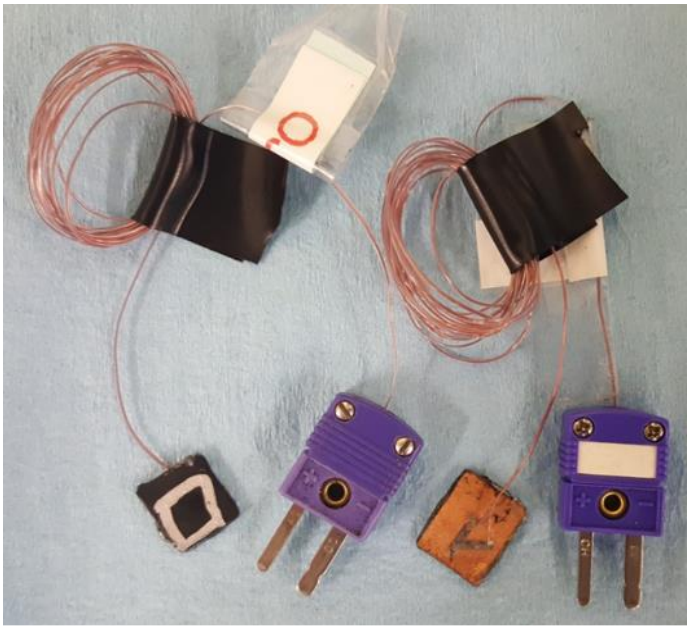

Figure 2.14: Surface thermocouples used for IR camera calibrations

A minimum of two thermocouples were used for each camera, usually placed protruding over the surface of a row of holes so that the calibration could include the coldest temperatures that would be observed during a test (Figure 2.15). When the cameras were placed in the final position to be used for later effectiveness experiments, the vane surface was then cooled down slowly from room temperature with images and data points being taken simultaneously with every change of 5 degrees over a range from 305 to 240K. The

data appeared roughly linear in the range of temperatures expected during testing, so a linear fit was applied for each unique S/C location. An example of the calibration results is shown in Figure 2.16, and the full set of calibrations can be found in Appendix A. As a check on their validity, the calibrations produced were compared to calibrations used for the 2015 program, which used cameras placed in a similar configuration. The calibrations produced in the two different programs were generally in agreement, although the deviations grew larger at the coldest temperatures, typically around 1-2K. This difference was attributed to a change in the viewing area of the model which occurred between the two programs. The target viewing window was lowered about two inches towards the mid-span of the model, which had the effect of reducing several cameras' viewing angle with respect to the model. The result of this calibration process is a full set of calibration points which exist at discrete S/C locations across the area of the model which was to be imaged. For positions within the image area not directly calibrated, a unique calibration can be generated by interpolating between two known calibration points. The interpolation of the slope and intercept of the set of calibration points was performed using a PCHIP scheme.

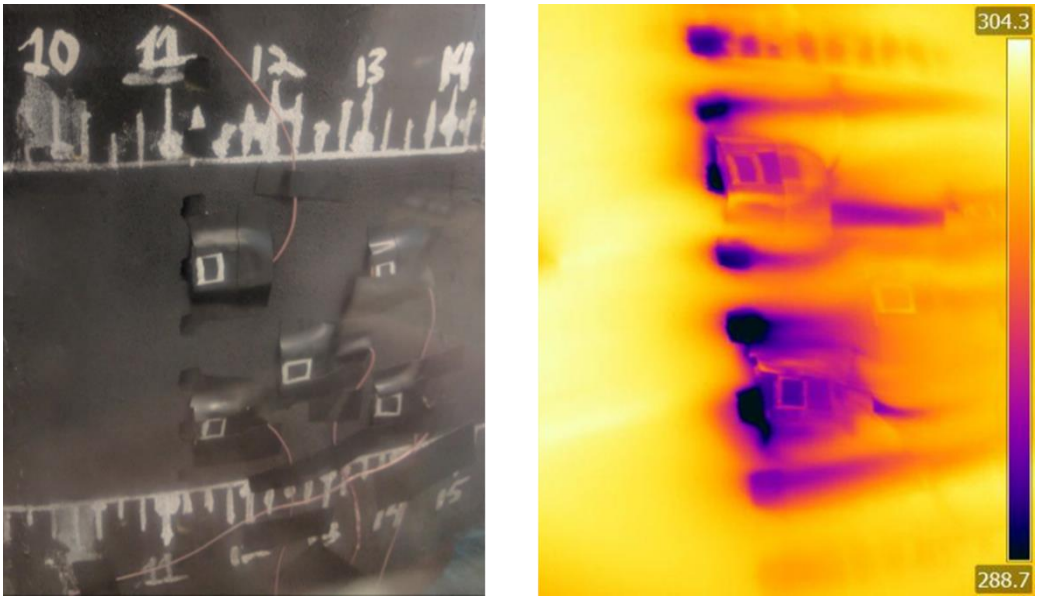

Figure 2.15: Example of calibration thermocouple placement and raw IR image

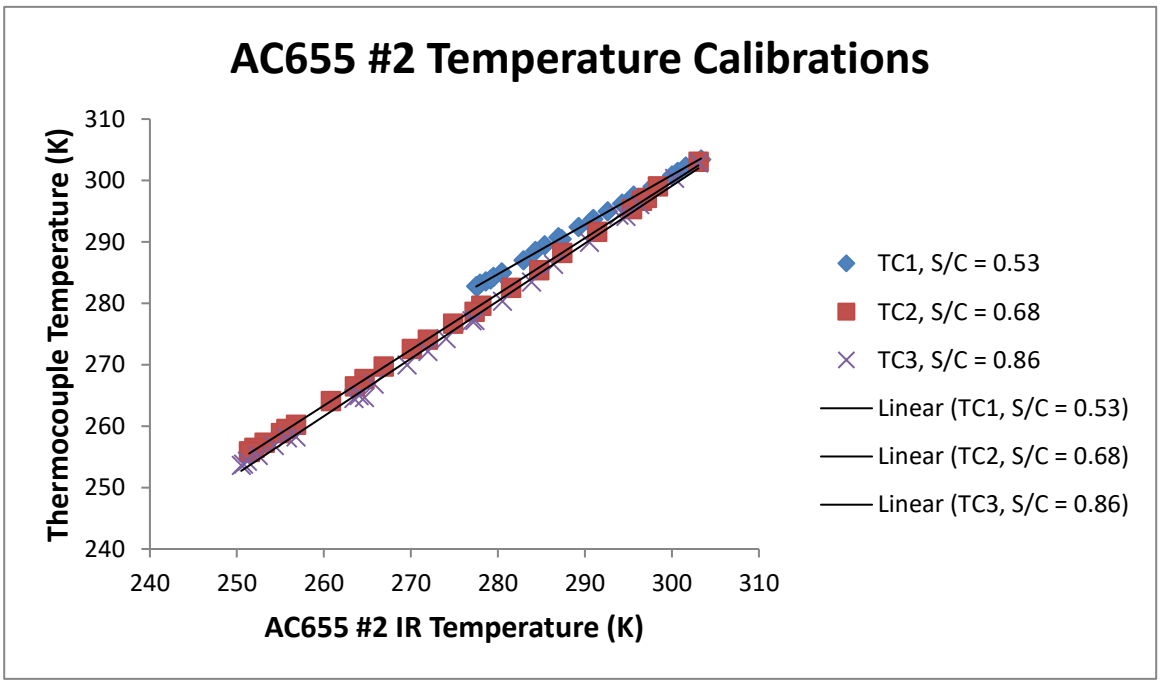

Figure 2.16: Example of IR temperature calibration for AC655 #2 camera

2.4.3 - Combining IR measurements from Individual Cameras

After the spatial and temperature calibrations have been applied for each camera, the images need to be combined into one continuous image encompassing the full span of the vane model. Individual camera datasets are combined according to minimum and maximum s/C limits specified by the user. Data in any overlapping region was calculated by applying a spatially-weighted average of the overlapping data. A linear blending function used for this purpose is shown in Equation 2.6, where ψ represents the percent distance across the spatial distance to be blended. This removes any small discontinuities in overlap regions which can be present due to propagation of uncertainty in the surface contours of η.

$$\eta_{blended} = \eta_{left}(1-\psi) + \eta_{riaht}(\psi) \tag{2.6}$$

2.5 - Experimental setup – Adiabatic Film Effectiveness Testing

Prior to each test, the desiccant packs would be regenerated overnight in an oven at 450 °F. Having placed the desiccant in the tunnel, the fan would be turned on at the desired high-speed mainstream velocity (11.0m/s). The water-to-air heat exchanger would then be activated to maintain the tunnel at its nominal operating mainstream temperature (305K). At the beginning of each test, the coolant valves would be fully opened, with a large amount of nitrogen introduced to the secondary flow loop, to perform a “cool down” until the average coolant temperature reached around 260K. This also helped the tunnel reach a lower relative humidity while the desiccant packs were in their most active drying state.

The mass flow rate of liquid nitrogen would then be reduced to slow the rate of cooling, and the gate valves controlling the coolant flow would be adjusted to reach a target operating condition.

Steady state was determined by monitoring the average coolant temperature, and waiting until the temperature had settled to varying within 0.1K over a period of 2-3 minutes. When steady state had been achieved at an average coolant temperature of around 250K, IR images were taken manually for each camera along with measurements of other relevant parameters that were recorded with LabVIEW. This process would be repeated five times to verify steady state conditions, each taken approximately a minute apart, before changing the coolant mass flow rate and moving on to the next operating condition. A settling period of around five minutes would be taken before beginning to take the next series of images. An example of a round of images produced during adiabatic effectiveness testing can be seen in Figure 2.17.

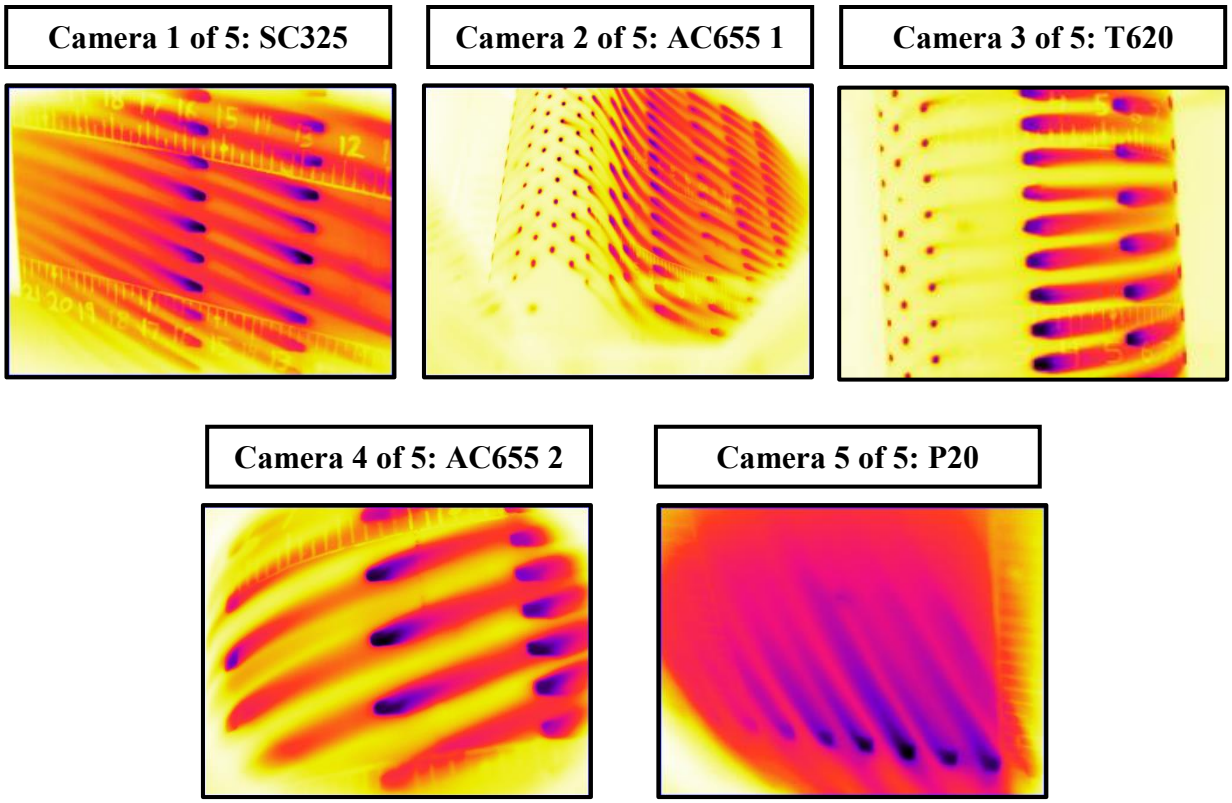

Figure 2.17: Examples of raw temperature data from the five cameras used for adiabatic effectiveness testing

2.5.1 - Calculating the Adiabatic Effectiveness

Initial values of adiabatic film effectiveness were measured with Equation 2.7, although a correction for conduction effects was necessary to calculate the final values recorded. In Equation 2.7, T_∞ is the mainstream temperature, $T_{c,exit}$ is the hole exit temperature, and T_s is the airfoil surface temperature used in place of the adiabatic wall temperature, T_{aw}. $T_{c,exit}$ was assumed to be the same as the temperature measured at the entrance to the inlet duct of each coolant passage.

$$\eta_{measured} = \frac{T_\infty - T_s}{T_\infty - T_{c,exit}} \tag{2.7}$$

2.5.2 - Correcting adiabatic effectiveness to account for conduction effects

A separate experiment was completed in order to measure values for the amount of conduction in the model. Several holes from each row within the viewing window were plugged with clay and covered over with paint. This created an area spanning the model surface which would be unaffected by coolant flowing over the surface. Coolant flow and tunnel conditions were matched to the conditions from the adiabatic film effectiveness tests, and data was collected in a similar manner. Equation 2.8 can be used to calculate an effectiveness value which represents the amount of cooling on the wall surface due to wall-normal conduction effects.

$$\eta_0 = \frac{T_\infty - T_s}{T_\infty - T_{c,exit}} \tag{2.8}$$

The originally measured effectiveness was then re-normalized according to Equation 2.9. Derivation of this conduction correction equation is discussed in Rutledge (2004) [27].

$$\eta_{aw} = \frac{\eta_{measured} - \eta_0}{1 - \eta_0} \tag{2.9}$$

Chapter 3 - Uncertainty Analysis

The individual uncertainties from the measurement system are described in the following sections. Uncertainty analysis for all calculated quantities were performed by applying either the error propagation method of Kline & McClintock [28] or the sequential perturbation method of Moffat [29].

3.1 - Uncertainty Analysis for Turbulence Levels

The uncertainty of turbulence levels is primarily determined by the precision uncertainty in the measurements of mean and root mean square velocities. The hot-wire probe is calibrated by fitting its voltage output to a mainstream velocity measured by a pitot static probe. Repeats of this calibration found that the uncertainty in the mean velocity measurement due to the hot-wire calibration was around 0.05 m/s. Data was collected at a rate of 10,000 Hz for a period of 10 seconds. During data collection, five samples were taken at each location traversed. The uncertainty in the root mean square velocity was calculated using the standard deviation of those sets of independent samples, shown in Equation 3.1 below.

$$\delta u_{rms} = \frac{2\sigma_{u_{rms}}}{\sqrt{n}} \tag{3.1}$$

Once the uncertainties were determined, they were propagated through Equation 3.2 to determine the overall uncertainty of the turbulence level.

$$\delta Tu = \sqrt{(\frac{\partial Tu}{\partial u_{mean}}\delta u_{mean})^2+(\frac{\partial Tu}{\partial u_{rms}}\delta u_{rms})^2} \tag{3.2}$$

The resulting uncertainties at each location were then averaged to generate a single uncertainty for the mean turbulence level. The results are shown in Table 3.1.

Table 3.1: Average uncertainty in turbulence level

Deviation/Uncertainty	Magnitude	Units
$\boldsymbol{\sigma_{u_{mean}}}$	0.027	m/s
$\boldsymbol{\sigma_{u_{rms}}}$	0.011	m/s
$\boldsymbol{\delta u_{mean}}$	0.050	m/s
$\boldsymbol{\delta u_{rms}}$	0.010	m/s
$\boldsymbol{\delta Tu}$	0.1%	-
$\boldsymbol{\bar{u}_{mean}}$	10.46	m/s
$\boldsymbol{\bar{u}_{rms}}$	0.780	m/s
$\boldsymbol{Tu}$	7.5%	-

3.2 - UNCERTAINTY IN PRESSURE DISTRIBUTION

The pressure distribution of the vane model was previously measured by Chavez in 2015 [23]. The pressure distribution is needed to estimate the local velocity used for calculating the blowing ratio. The final form of the equation used to calculate the pressure distribution is shown in Equation 3.3.

$$\boldsymbol{C_{p,local}} = \frac{\boldsymbol{P_{T,inlet}} - \boldsymbol{P_{S,local}}}{\boldsymbol{P_{T,inlet}} - \boldsymbol{P_{S,inlet}}} = \frac{\boldsymbol{\Delta P_{local}}}{\boldsymbol{\Delta P_{inlet}}} = (\frac{\boldsymbol{U_{\infty,local}}}{\boldsymbol{U_{\infty,inlet}}})^2 \tag{3.3}$$

The uncertainty in the measurements was primarily due to the fossilized bias of the linear fits for each pressure transducer, which ranged between 4.5 to 7.8 Pa. Drifting of the zero pressure reading (~0.01 Pa) and precision uncertainty also contributed significantly where the flow was measured in a low local velocity location. The error propagation of the pressure distribution is shown in Equation 3.4.

$$\delta C_{p,local} = \sqrt{\left(\frac{1}{\Delta P_{inlet}} * \delta \Delta P_{local}\right)^2 + \left(\frac{-\Delta P_{local}}{\Delta P_{inlet}^2} * \delta \Delta P_{inlet}\right)^2} \tag{3.4}$$

Figure 3.1 depicts the pressure distribution uncertainties at their s/C locations. The relative uncertainty of the pressure distribution becomes much higher when measured in areas of low velocity near the stagnation line, but otherwise the uncertainty was quite small, typically around 2% of the local Cp.

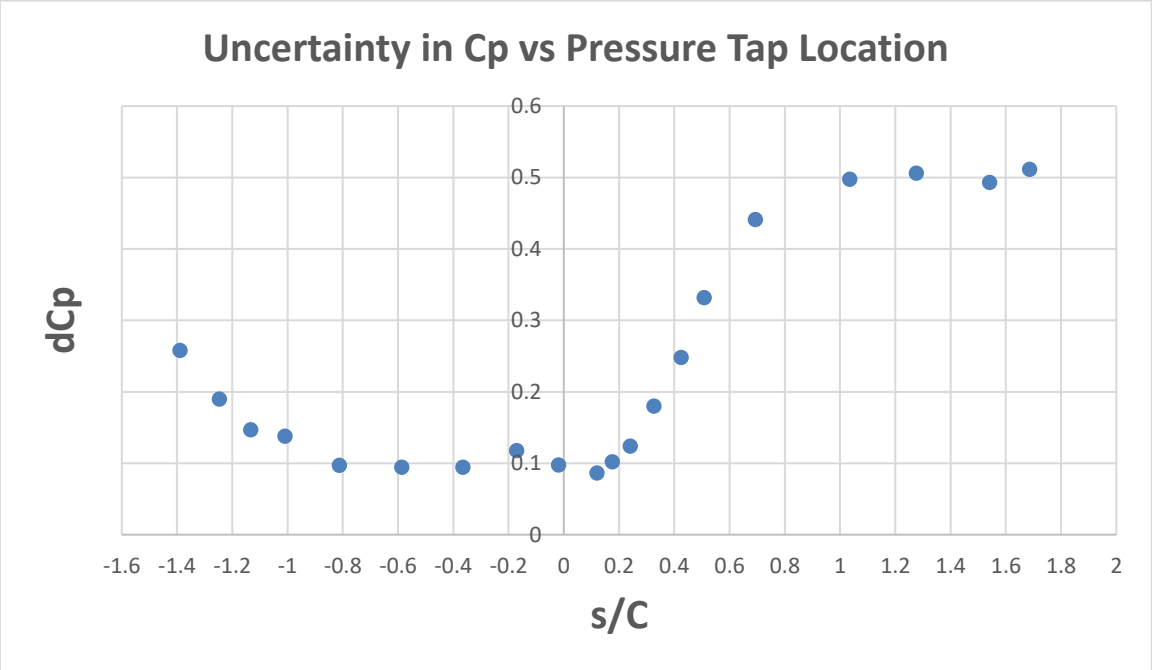

Figure 3.1: Uncertainty in the local pressure distribution

3.3 - Uncertainty in Orifice plate Discharge Coefficient, $C_{d,o}$

The procedure for obtaining the orifice plate discharge coefficient by calibrating against a laminar flow element is described by Chavez [21]. The resulting polynomial for discharge coefficient is a function of the pipe Reynolds number, $(\frac{10^6}{Re_{D,p}})^{0.75}$. The original measurements of discharge coefficients were performed by Chavez in 2015 [23], uncertainty analysis was more recently conducted for this thesis. The primary contributors to the uncertainty in Reynolds number are the fossilized error of the pressure transducers used during calibration and the calibration of the laminar flow element provided by the manufacturer. The discharge coefficients and their uncertainties for each coolant channel orifice plate are plotted in Figure 3.2-4 with respect to mass flow rate. Relative uncertainties in the discharge coefficients in the range of normal operating flow rates during testing (shown in red) were on the order of 1-2%.

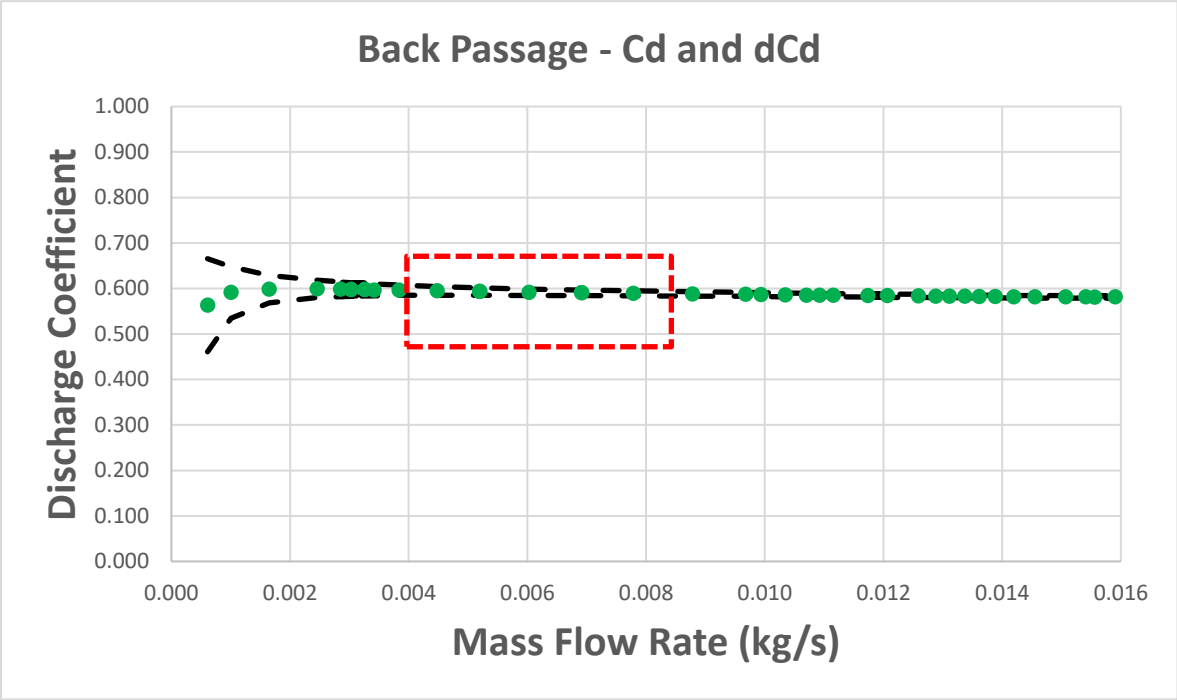

Figure 3.2: Measured Cd and uncertainty for the back passage orifice plate

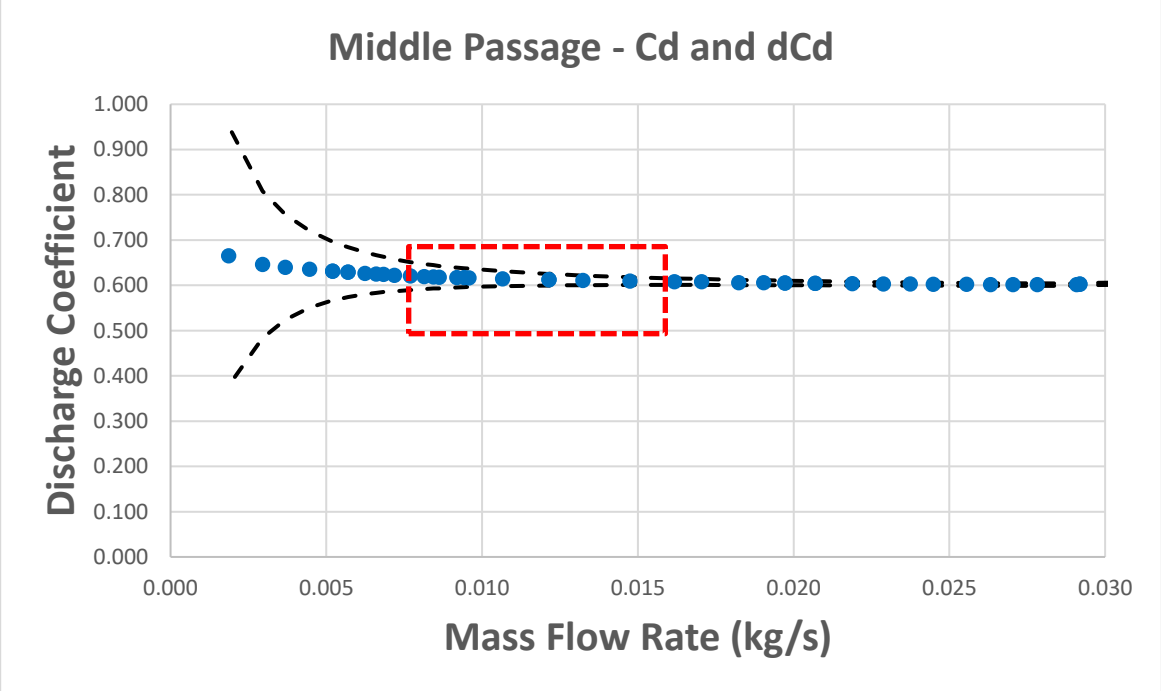

Figure 3.3: Measured Cd and uncertainty for the middle passage orifice plate

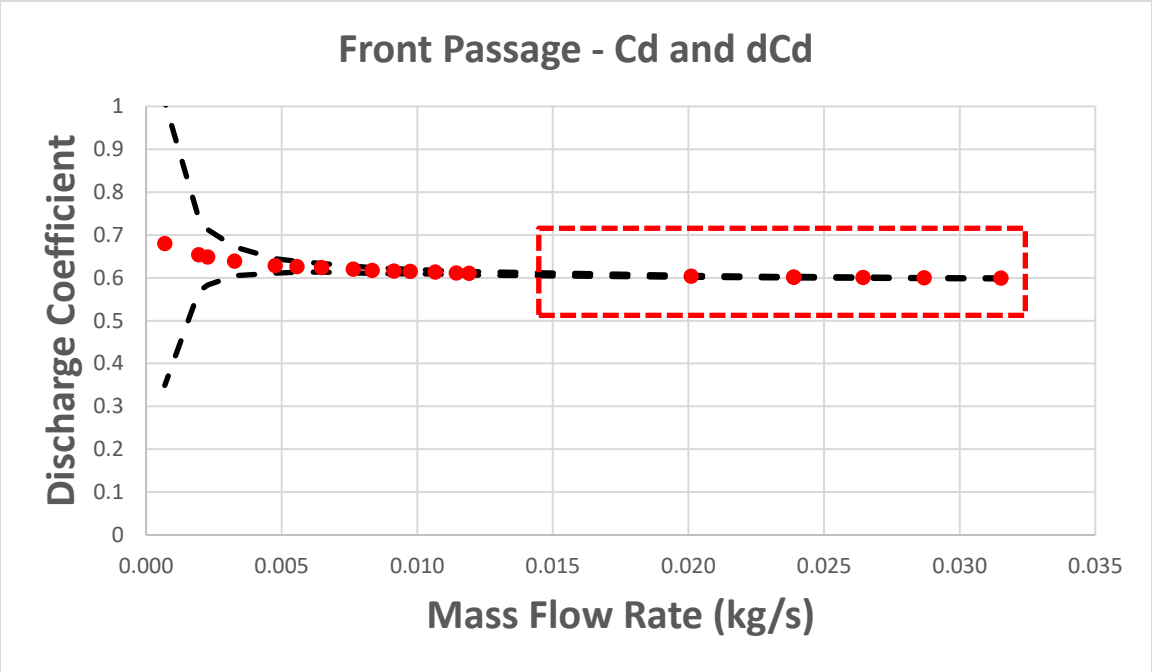

Figure 3.4: Measured Cd and uncertainty for the front passage orifice plate

3.4 - Uncertainty in Coolant Hole Discharge Coefficient $C_{d,holes}$

Discharge coefficients were measured for the coolant holes for each row tested individually (Rows 2-5, 12-15) by Chavez in 2015 [23]. Uncertainties in the hole discharge coefficients were calculated from Equation 2.5 through sequential perturbation of the uncertainties in the local pressure distribution, the orifice plate discharge coefficients, and the pressure transducers used to measure the coolant passage plenum pressure during testing. Equation 3.6 shows the calculation for uncertainty in coolant hole discharge coefficient, where $\delta C_{d,i}$ is the difference between the perturbed value of discharge coefficient from the i variable and the measured value of discharge coefficient, $\delta C_{d,i} = C_{d,i}^{+} - C_{d,0}$.

$$\delta C_{d,holes} = \sqrt{\delta C_{d_{C_p}}^2 + \delta C_{d_{C_{d,o}}}^2 + \delta C_{d_{P_{t,c}}}^2} \quad (3.6)$$

The uncertainty in the orifice plate discharge coefficients was the primary contributor to the uncertainty in $C_{d,holes}$, especially at lower flow rates. The uncertainty in the local pressure distribution was also significant at lower flow rates for several pressure side rows with a low local velocity. Figure 3.5 shows the uncertainties in the discharge coefficients versus their flow rates. On average, the uncertainty in the discharge coefficient was about 2-5% of the measurement value.

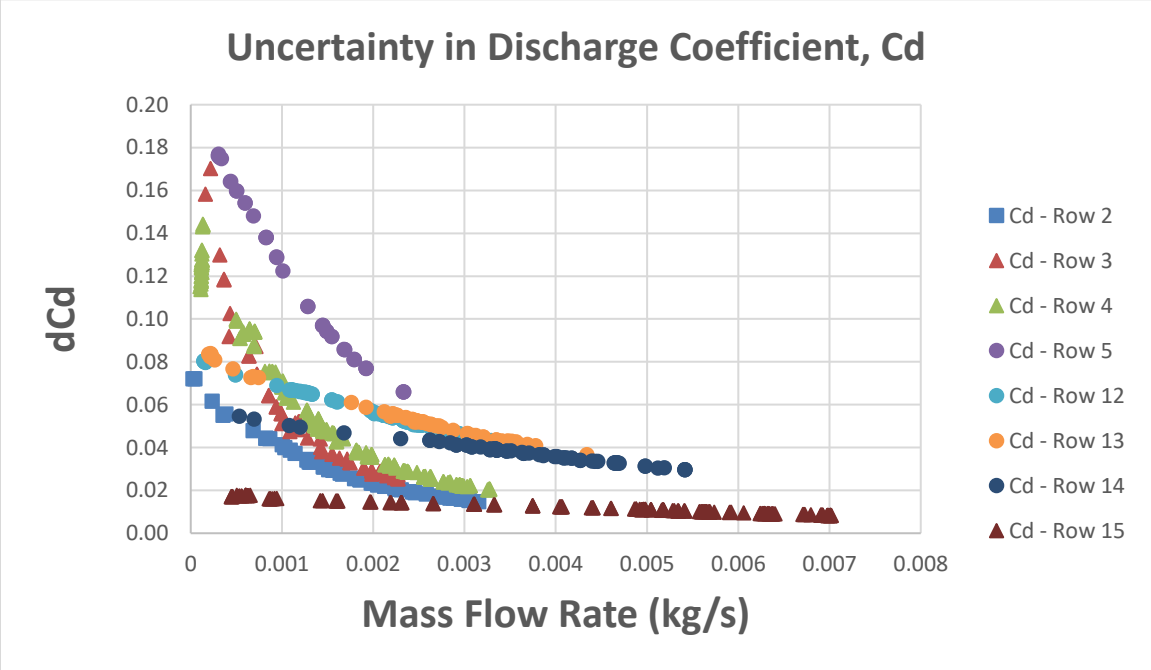

Figure 3.5: Uncertainties in the calculated hole discharge coefficients.

3.5 - Uncertainty in the Mass Fraction Hole Splits, F

The initial estimates for the hole mass flow rates based on hole discharge coefficients were used to calculate a fractional flow split which must always sum to 100% of the flow within the channel. Since the same pressure transducers and orifice plates were used during the discharge coefficient measurements and the film cooling experiments, a significant amount of the uncertainty during the film cooling tests can be removed. Renormalizing the mass flow rates calculated with $C_{d,holes}$ into fractional flow splits, F, removes the bias uncertainty from the orifice plate discharge coefficient and pressure transducers, which were the dominant contributors to the uncertainty in $C_{d,holes}$. The resulting uncertainty for the mass fraction flow splits was less than 1% during the adiabatic effectiveness tests.

3.6 - Uncertainty in Thermocouple Calibration, Mainstream Temperature, and Surface Temperature

A calibration was generated for each thermocouple by creating a linear fit between the temperature from the standard NIST calibration for an E-type thermocouple and that of a high accuracy thermistor in a glycol bath providing a reference. An example of this glycol bath calibration in Figure 2.8 shows that a linear fit is an appropriate choice for the range of temperatures that would be present during adiabatic effectiveness testing. A 95% confidence interval of the calibration curve was calculated as shown by Equation 3.7, referenced from Montgomery and Runger [30].

$$95\%\ CI = \pm t_{\frac{\alpha}{2},n-2} s_{yx} \sqrt{\frac{1}{n} + \frac{(x_p - \bar{x})^2}{SS_{xx}}} \tag{3.7}$$

To simplify the analysis, the average of the confidence interval was used in future error propagations. This results in a conservative estimate of the uncertainty for most temperature values measured in the project, and a liberal estimate for values near the minimum and maximum of the temperature calibration region, such as the near-hole region and far downstream where effectiveness is low. In this case, the average uncertainty in the thermocouples was $\delta T_{tc} = 0.17\text{K}$, which includes the confidence intervals of the calibration curves as well as a maximum bias of 0.05K due to the bias of the thermistor within the glycol bath taken from the manufacturer specifications [31].

Variations in the uniformity of the mainstream temperature of the tunnel were typically 0.5K. A schematic of the three mainstream thermocouple locations is shown in Figure 2.3. An average of the three mainstream temperature measurements was used for effectiveness calculations. The systematic uncertainty of the average mainstream temperature values was approximated by Equation 3.8.

$$\delta T_{\infty,variations} = t_{\frac{\alpha}{2},3} * \frac{\sigma_{T_\infty}}{\sqrt{3}} \tag{3.8}$$

The final uncertainty of the mainstream temperature, δT_∞ = 0.44K, was calculated by Equation 3.9, which included bias due to the calibration, bias due to variations within the wind tunnel, and the precision uncertainty during the actual test.

$$\delta T_\infty = \sqrt{\delta T_{\infty,variations}^2 + \delta T_{\infty,fossilized}^2 + \delta T_{\infty,p}^2} \tag{3.9}$$

Packard [32] performed in-situ IR temperature calibrations using the same procedure as this study. Repeat calibrations were used to assess the overall uncertainty in the test-to-test repeatability of the calibrations, which was about $\delta T_s = 0.5$K for all cameras. This included bias due to the affixed thermocouple, the confidence interval of the linear fit, and spread in the repeat calibrations. An example of the IR camera temperature calibrations is shown in Figure 2.14.

3.7 - Uncertainty in Adiabatic Effectiveness

The uncertainty in the measured film effectiveness is due to contributions from the uncertainties in the mainstream temperature, surface temperature, and coolant exit temperature. There is also an added uncertainty from the measurement of the effectiveness due to conduction effects, which is based on the same three temperature measurements. Equation 3.10 shows the uncertainty propagation for an arbitrary measure of effectiveness on the surface of the vane model.

$$\delta \eta_{measured,0} = \sqrt{(\frac{\partial \eta}{\partial T_\infty}\delta T_\infty)^2 + (\frac{\partial \eta}{\partial T_S}\delta T_S)^2 + (\frac{\partial \eta}{\partial T_{c,exit}}\delta T_{c,exit})^2} \tag{3.10}$$

The uncertainty in effectiveness ranged from $\delta\eta = 0.009 - 0.012K$ depending on the local value of effectiveness. A similar range was found for the uncertainty in the conduction correction (η_0). The final measurement of adiabatic effectiveness has contributions from the film effectiveness (η) and the conduction correction (η_0), which is shown by Equation 3.11.

$$\delta\eta_{aw} = \sqrt{(\frac{\partial\eta_{aw}}{\partial\eta_{measured}}\delta\eta_{measured})^2 + (\frac{\partial\eta_{aw}}{\partial\eta_0}\delta\eta_0)^2} \qquad (3.11)$$

The final uncertainty in adiabatic effectiveness is somewhat dependent on the magnitude of the conduction correction used. Based on the average value of $\eta_0 = 0.05$, the range in uncertainty for the final adiabatic effectiveness measurement was $\delta\eta_{aw} = 0.010 - 0.016K$.

3.7.1 – Repeatability of IR Images

The repeatability of the IR images used in the laterally averaged adiabatic effectiveness measurements can be assessed by comparing the results from each image taken during testing. This provides an assurance that the test model had already reached steady state when image collection had begun. Figure 3.6 shows the laterally averaged results for each image from the All Open – Low Tu test at the lowest flow rate, S1. Figure 3.7 compares the laterally averaged results from the first and last image taken for the All Open – Low Tu test at all five flow rates tested. In general, the repeatability for the measurements shown is quite good, as most series appear nearly line-on-line. The repeatability of the laterally averaged adiabatic effectiveness results for both figures

presented seems within the uncertainty of the local adiabatic effectiveness previously described.

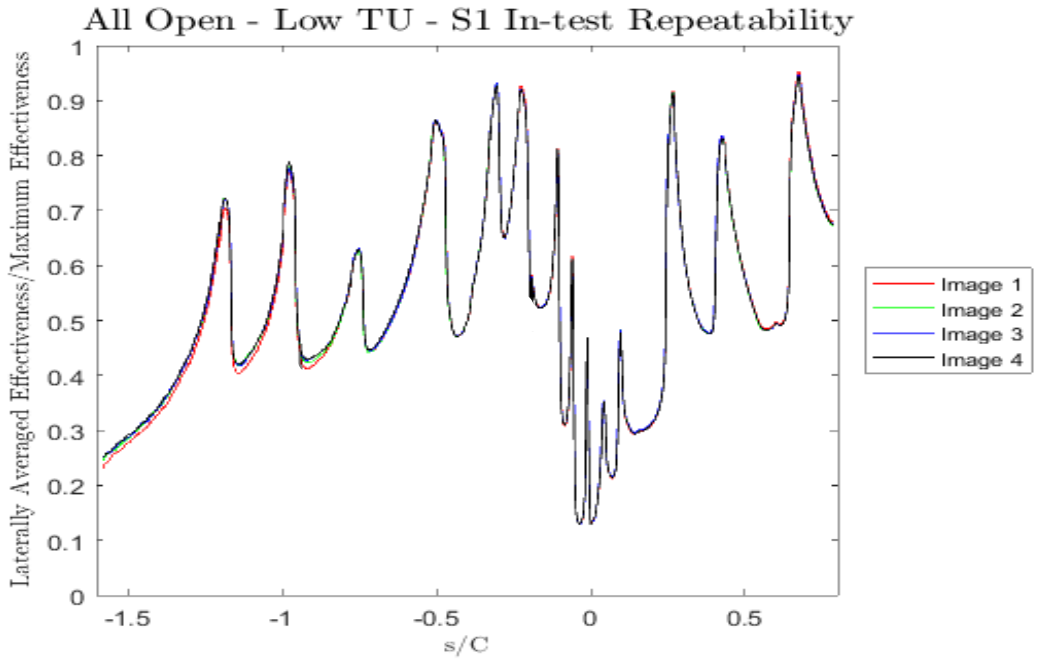

Figure 3.6: Repeatability of laterally averaged adiabatic effectiveness for four images used in the All Open - Low Tu test at the lowest flow rate – S1.

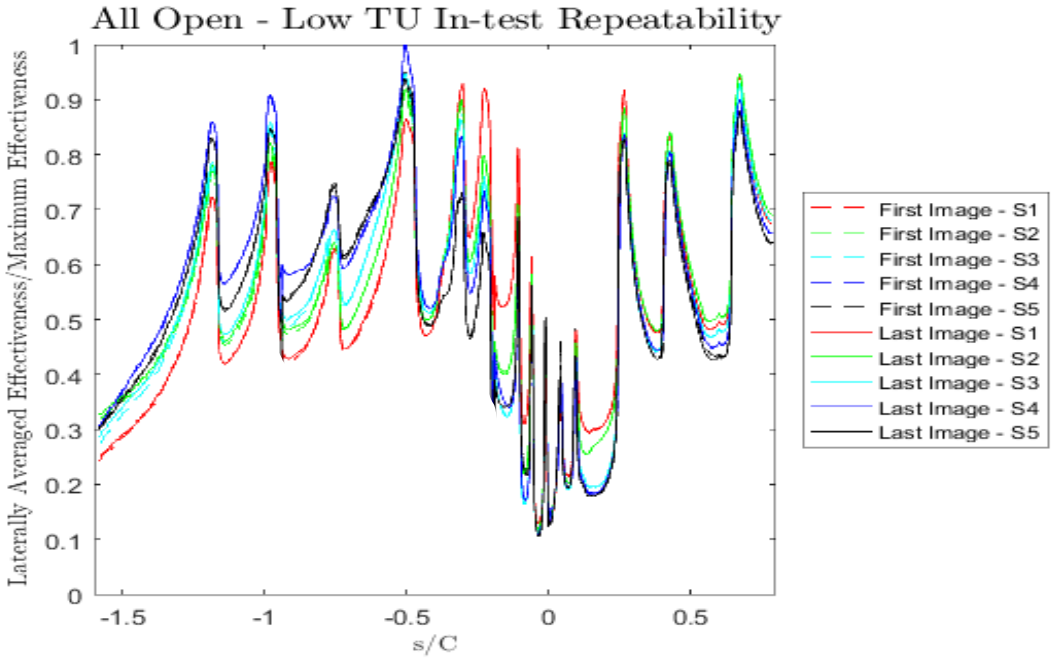

Figure 3.7: Repeatability of laterally averaged adiabatic effectiveness from first and last images used in the All Open – Low Tu tests

3.8 -UNCERTAINTY IN BLOWING RATIO

In order to calculate the uncertainty in blowing ratio, it is necessary to represent Equation 3.12 in terms of primary measurements. Blowing ratio for the showerhead holes was calculated using the mainstream approach velocity, while the shaped holes used the local velocity determined by the pressure distribution of the model.

$$M = \frac{\rho_c U_c}{\rho_\infty U_{\infty,}}(showerhead) \; or \; M = \frac{\rho_c U_c}{\rho_\infty U_{local}}(non - showerhead) \qquad (3.12)$$

The densities of the mainstream and coolant flows were calculated through the ideal gas law. Based on the amount of nitrogen that was pumped into the tunnel during cool down, it is a reasonable assumption to say that the gas species inside the tunnel is mostly nitrogen. Since the coolant and mainstream were at the same pressure and of the same species, the density ratio between those two flows reduces to a ratio of the mainstream and coolant temperatures.

$$DR = \frac{\rho_C}{\rho_\infty} = \frac{T_\infty}{T_C} \qquad (3.13)$$

The mainstream approach velocity was determined from the dynamic pressure measured by the pitot-static probe located just downstream of the contraction nozzle in the approach section of the tunnel.

$$U_\infty = \sqrt{\frac{2\Delta P_{dyn,CN}}{\rho_\infty}} = \sqrt{\frac{2\Delta P_{dyn,CN} R T_\infty}{P_\infty}} \qquad (3.14)$$

Local velocity is related the mainstream approach velocity by the pressure distribution at the location of each row of holes.

$$U_{local} = U_{\infty} * \sqrt{C_{p,local}} = \sqrt{\frac{2\Delta P_{dyn,CN} C_{p,local} RT_{\infty}}{P_{\infty}}} \tag{3.15}$$

The velocity of the coolant can be calculated from the coolant mass flow rate through the orifice plate in Equation 3.16. The mass flow rate was determined from the orifice plate equation and discharge coefficient calibration shown by Equation 3.17.

$$U_c = \frac{F\dot{m}_{c,o} RT_c}{n_h A_h P_{\infty}} \tag{3.16}$$

$$\dot{m}_{c,o} = C_{d,o} A_o * \sqrt{\frac{2\Delta P_o (P_{\infty} + P_{pipes})}{(1-\beta^4) RT_o}} \tag{3.17}$$

By combining Equations 3.12-3.17, it is possible to represent the blowing ratio from Equation 3.12 in terms of primary measurements and physical constants of the system.

$$M = \frac{T_{\infty}}{T_C} \sqrt{\frac{P_{\infty}}{2\Delta P_{dyn,CN} C_{p,local} RT_{\infty}}} \frac{FRT_c}{n_h A_h P_{\infty}} C_{d,o} A_o * \sqrt{\frac{2\Delta P_o (P_{\infty} + P_{pipes})}{(1-\beta^4) RT_o}} \tag{3.18}$$

After reducing repeated terms, Equation 3.19 shows the form of the blowing ratio calculation used for uncertainty analysis.

$$M = \frac{FT_\infty C_{d,o} D_o^2}{n_h P_\infty D_h^2} * \sqrt{\frac{\Delta P_o P_\infty (P_\infty + P_{pipes})}{T_\infty T_o (1-\beta^4) \Delta P_{dyn,CN} C_{p,local}}} \tag{3.19}$$

The uncertainty in blowing ratio as calculated by Equation 3.19 is most easily determined by using the sequential perturbation method of Moffat. Equation 3.20 shows the calculation for uncertainty in blowing ratio, where δM_i is the difference between the perturbed value of blowing ratio from the i variable and the measured value of blowing ratio, $\delta M_i = M_i^+ - M_0$.

$$\delta M = \sqrt{\delta M_F^2 + \delta M_{T_\infty}^2 + \delta M_{C_{d,o}}^2 + \delta M_{C_{d,o}}^2 + \delta M_{D_o}^2 + \delta M_{P_\infty}^2} \ldots \tag{3.20}$$

$$\ldots + \sqrt{\delta M_{D_h}^2 + \delta M_{\Delta P_o}^2 + \delta M_{P_{pipes}}^2 + \delta M_{T_o}^2 + \delta M_{\Delta P_{dyn,CN}}^2 + \delta M_{C_{p,local}}^2}$$

An example of the uncertainty calculations is shown in Table 3.2 for Row 15 in the All Open – Low Tu tests at a low flow rate. The same example is then repeated at a high flow rate in Table 3.3. The distribution of uncertainty for each row used during All Open tests is shown at a low and high flow rates in Table 3.4-5. In general, uncertainties in blowing ratio ranged from 7 to 9%, and were slightly larger at lower coolant flow rates. The uncertainty in the blowing ratio was dominated by the uncertainty in the metering hole diameter. The next largest contributors to the uncertainty in blowing ratio were the local pressure distribution, orifice plate discharge coefficient, and orifice plate pressure transducers. The uncertainty for the showerhead holes was similar, although the uncertainty due to local pressure distribution uncertainty was not included in these cases.

Table 3.2: Uncertainty in Blowing Ratio for Row 12 in the All Open – Low Tu test at a low flow rate

Measurement	x	Units	δx	x+δx	M(x+δx)	δM(x+δx)
Row Mass Fraction	0.1725	--	0.0017	0.1742	0.8986	0.0089
Mainstream Temperature	305.25	K	0.44	305.69	0.8910	0.0013
Orifice Discharge Coefficient	0.6177	--	0.0073	0.6249	0.9002	0.0105
Orifice Throat Diameter	0.043	m	0.00003	0.043	0.8910	0.0012
Number of Coolant Holes	18	--	0	18		
Mainstream Pressure	100200	Pa	500	100700	0.8853	-0.0044
Coolant Hole Diameter	0.0026	m	0.0001	0.0027	0.8242	-0.0655
Orifice Differential Pressure	106.24	Pa	6.92	113.16	0.9182	0.0285
Pipe Differential Pressure	3455.43	Pa	13.96	3469.38	0.8898	0.0001
Orifice Temperature	244.32	K	0.17	244.49	0.8894	-0.0003
Beta	0.55	--	0	0.55		
Mainstream Dynamic Pressure	521.16	Pa	3.48	524.64	0.8868	-0.0030
Local Pressure Distribution	-6.45	--	0.1241	-6.32	0.8972	0.0075
M	0.890					
δM_{total}	0.073					
Relative Uncertainty	8.2%					

Table 3.3: Uncertainty in Blowing Ratio for Row 12 in the All Open – Low Tu test at a high flow rate

Measurement	x	Units	δx	x+δx	M(x+δx)	δM(x+δx)
Row Mass Fraction	0.1590	--	0.0016	0.1613	1.6748	0.0166
Mainstream Temperature	304.52	K	0.44	304.95	1.6606	0.0024
Orifice Discharge Coefficient	0.6129	--	0.0024	0.6153	1.6646	0.0064
Orifice Throat Diameter	0.043	m	0.00003	0.043	1.6605	0.0023
Number of Coolant Holes	18	--	0	18		
Mainstream Pressure	100219	Pa	500	100719	1.6500	-0.0082
Coolant Hole Diameter	0.0026	m	0.0001	0.0027	1.5361	-0.1221
Orifice Differential Pressure	443.59	Pa	6.92	450.51	1.6711	0.0129
Pipe Differential Pressure	2451.62	Pa	13.96	2465.58	1.6583	0.0001
Orifice Temperature	246.11	K	0.17	246.28	1.6576	-0.0006
Beta	0.55	--	0	0.55		
Mainstream Dynamic Pressure	518.67	Pa	3.48	522.16	1.6527	-0.0055
Local Pressure Distribution	-6.45	--	0.1241	-6.32	1.6722	0.0140
M	1.658					
δM_{total}	0.125					
Relative Uncertainty	7.6%					

Table 3.4: Distribution of Uncertainty in Blowing Ratio in the All Open – Low Tu test at a low flow rate

Row	M	δMtotal	Relative Uncertainty
1	0.534	0.040	7.4%
2	0.842	0.068	8.1%
3	0.989	0.082	8.3%
4	1.204	0.102	8.5%
5	1.256	0.121	9.7%
6	0.865	0.080	9.2%
7	0.878	0.072	8.2%
8	0.677	0.056	8.2%
9	0.563	0.046	8.2%
10	0.968	0.080	8.2%
11	1.265	0.104	8.2%
12	0.890	0.073	8.2%
13	0.923	0.076	8.2%
14	0.897	0.074	8.3%

Table 3.5: Distribution of Uncertainty in Blowing Ratio in the All Open – Low Tu test at a high flow rate

Row	M	δMtotal	Relative Uncertainty
1	1.071	0.075	7.0%
2	1.689	0.130	7.7%
3	2.022	0.160	7.9%
4	2.645	0.213	8.1%
5	3.330	0.303	9.1%
6	2.631	0.227	8.6%
7	2.294	0.173	7.6%
8	2.249	0.170	7.6%
9	2.248	0.170	7.6%
10	2.325	0.176	7.6%
11	2.458	0.186	7.6%
12	1.658	0.125	7.6%
13	1.344	0.102	7.6%
14	1.178	0.089	7.6%

Chapter 4 – Adiabatic Effectiveness Testing Results

Adiabatic effectiveness tests were performed under several different coolant configurations: All Open (AO) refers to cases when all rows of holes were blowing coolant, Non-Showerhead (NSH) refers to cases when all laidback fanshaped holes were blowing coolant but the cylindrical rows in the showerhead (Rows 7-11) were blocked off, and Single Row (SR) refers to cases where a single row of laidback fanshaped holes was tested in isolation. Four rows on both the pressure side (Rows 2-5) and three rows on the suction side (Rows 12-14) were tested individually. In addition, another test using the All Open configuration was repeated with the turbulence grid in place, providing a higher mainstream turbulence level. Comparisons between these configurations were made in order to assess the impact of local curvature, showerhead cooling, and mainstream turbulence. Single row cases were compared to predictive flat plate correlations from the literature in order to show the effect due to local curvature. The All Open and Non-Showerhead cases were compared to isolate the effects of upstream showerhead cooling. All Open Low and High Tu cases were compared to show the effects of increasing mainstream turbulence levels.

Tables 4.1-4 show the distribution of blowing ratios measured for each test. Adiabatic effectiveness results have been laterally averaged over an integer number of pitches (between 2 to 4 depending on P/D) to produce laterally averaged plots. Results from tests using full coverage configurations are plotted across the full span of the test model in terms of s/C. Single row results are plotted versus x/D, where the origin is set at

the downstream breakout location. Plots of adiabatic effectiveness for an individual row have been normalized by that row's coverage level (t/P). Full coverage plots, which do not have a single coverage value, have been normalized by the maximum effectiveness level measured during all set points for that test (η_{max}). This work was based on proprietary data funded by Siemens Energy. Information on the performance of the first two rows on the pressure and suction sides (Rows 5-6, 12-13) from the three full coverage tests has been redacted at their request.

Table 4.1: Distribution of blowing ratios for Single Row - Low Tu tests

Setpoint	**S1**	**S2**	**S3**	**S4**	**S5**
Row	M	M	M	M	M
2	0.63	0.75	0.98	1.24	1.46
3	0.99	1.30	1.56	1.78	2.02
4	1.01	1.52	1.97	2.51	-
5	1.93	2.46	3.00	-	-
12	0.93	1.00	1.03	1.10	1.16
13	0.94	1.00	1.04	1.10	1.29
14	0.92	0.98	1.04	1.05	1.11

Table 4.2: Distribution of blowing ratios for Non-Showerhead - Low Tu tests

Setpoint	**S1**	**S2**	**S3**	**S4**	**S5**	
Row	M	M	M	M	M	
1	0.54	0.67	0.80	0.91	1.08	
2	0.86	1.06	1.26	1.44	1.70	
3	1.01	1.31	1.58	1.80	2.04	
4	1.25	1.78	2.08	2.33	2.64	
5	1.30	1.82	2.33	2.70	3.02	
6	0.90	1.32	1.76	2.11	2.39	
12	0.89	1.01	1.16	1.32	1.51	
13	0.92	0.97	1.02	1.09	1.23	
14	0.89	0.93	0.95	0.99	1.07	

Table 4.3: Distribution of blowing ratios for All Open - Low Tu tests

Setpoint	**S1**	**S2**	**S3**	**S4**	**S5**
Row	M	M	M	M	M
1	0.53	0.67	0.79	0.9	1.07
2	0.84	1.06	1.25	1.42	1.68
3	0.99	1.3	1.56	1.78	2.02
4	1.21	1.76	2.06	2.3	2.64
7	0.88	1.28	1.66	2.01	2.28
8	0.68	1.16	1.63	2.01	2.24
9	0.56	1.13	1.66	2.05	2.24
10	0.97	1.34	1.69	2.03	2.32
11	1.26	1.56	1.84	2.13	2.45
14	0.9	0.96	0.99	1.04	1.17

Table 4.4: Distribution of blowing ratios for All Open - High Tu tests

Setpoint	**S1**	**S2**	**S3**	**S4**	**S5**
Row	M	M	M	M	M
1	0.56	0.71	0.85	0.93	1.13
2	0.88	1.11	1.33	1.47	1.77
3	0.97	1.27	1.7	1.91	2.14
4	1.16	1.7	2.23	2.48	2.77
7	0.94	1.32	1.74	2.08	2.38
8	0.79	1.19	1.7	2.08	2.34
9	0.72	1.15	1.73	2.12	2.34
10	1.01	1.38	1.77	2.1	2.41
11	1.25	1.62	1.93	2.21	2.55
14	0.83	1	1.04	1.09	1.22

4.1 - SINGLE ROW RESULTS

4.1.1 - Coolant Temperature Correction

While processing the data from the single row tests, it was found that the coolant temperature was significantly warming between entering the coolant inlet duct and exiting onto the model surface near the top of the model. Thermocouple measurements were made at the entrance to the inlet duct and at the top of the internal channel. These measurements showed a large amount of warming taking place, as much as 15-20K during single row testing. This was attributed to the lower mass flow rates used when only a single row was in operation, because the difference between the same two thermocouple measurements during the All Open tests was negligible (~1-2 K). This was resulting in an artificially low effectiveness level because the coolant temperature measured at the inlet duct was no longer a good approximation of the discharge temperature. A coolant temperature correction was used in which the in-hole effectiveness of the single row test was matched to the in-hole effectiveness measured when all rows were blowing. The coolant temperature for each single row test was iteratively adjusted until those two conditions were matched. This lowered the density ratio for all of the single row tests below 1.20, with final values ranging from 1.10 to 1.15, with the largest change in corrected temperature occurring at the lowest blowing ratios. Because the temperature correction was based on the measured in-hole effectiveness of one hole, laterally averaged results were obtained using one pitch width around that same hole. The area being laterally averaged downstream was adjusted

by tracking the direction of the coolant flow. An example of this cropping process in shown in Figure 4.1.

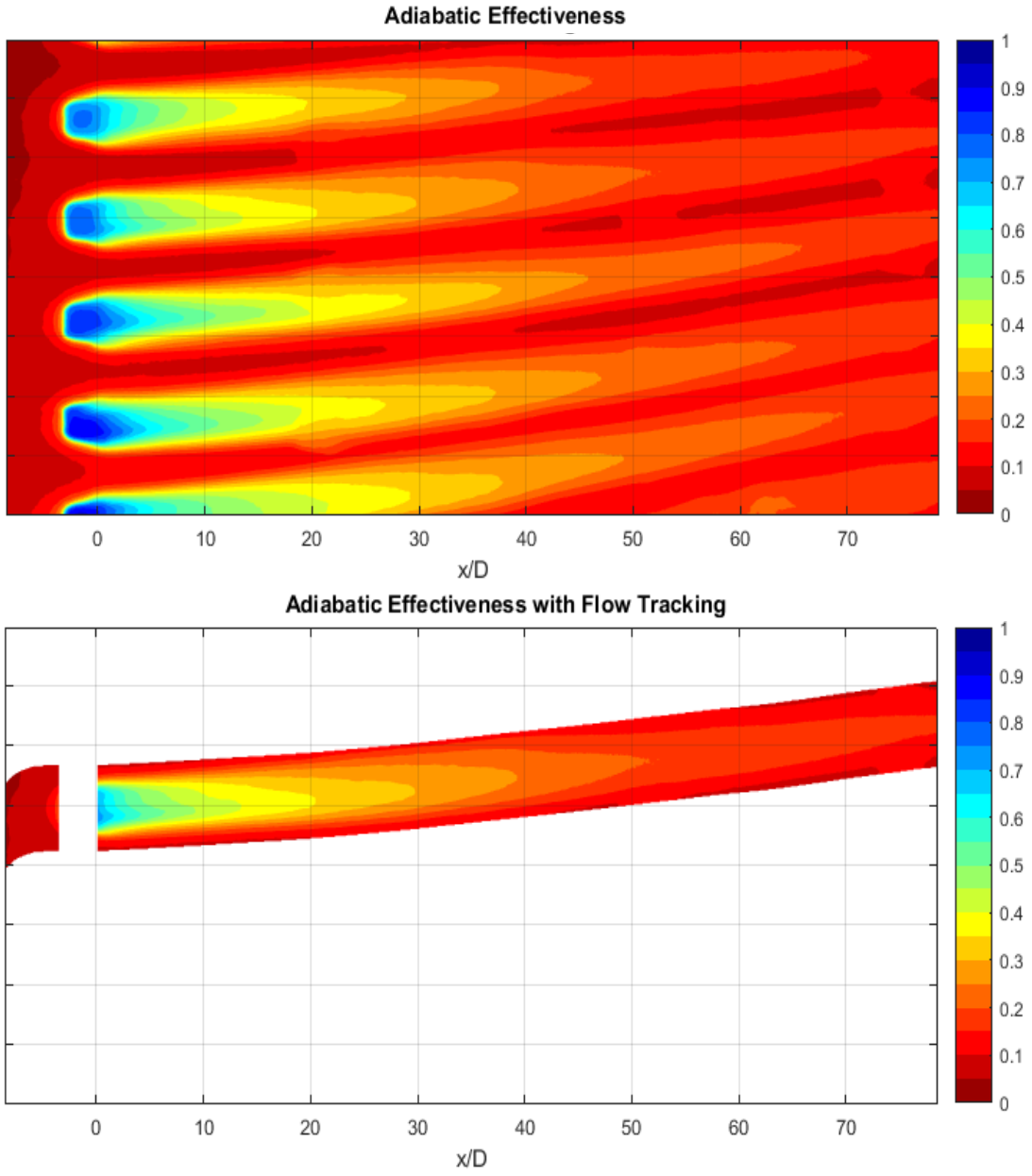

Figure 4.1: Example of adiabatic effectiveness contours before (top) and after (bottom) cropping to a single pitch width with flow tracking used for laterally averaging single row results

4.1.2 - Comparison to Flat Plate Correlations

An additional test was performed on the TTCRL's smaller wind tunnel facility using a flat plate coupon machined with a row of laidback fanshaped holes with the same geometry used in the vane model. More detail on the small tunnel facility and test section can be found in a dissertation written by McClintic [33]. In general, operating parameters were matched to the conditions of tests performed on the vane model in the large wind tunnel facility, shown in Table 4.5. The mainstream velocity was matched to the local velocity at Row 15 on the vane model, 54.0 m/s. This test provided an opportunity to validate the correlation proposed by Colban et al. [9] for this particular hole geometry. The form of the correlation (Equation 1.12) is discussed in Chapter 1. Figure 4.2 shows the flat plate laterally averaged adiabatic effectiveness results compared to the Colban correlation prediction. Data between 18-21D downstream has been removed due to contamination from additional conduction through a hatch seam. There is a good correspondence at x/D=0 between the measured results and the initial predicted effectiveness which is based on the coverage. The correlation matches up closely with the measured results at moderate blowing ratios (M=1.49, 2.01), but under predicted the effectiveness values at low blowing ratios (M=0.79, 1.02). The effectiveness values measured at M=2.23 were actually lower than at M=2.01 and 1.49. When providing additional coolant does not increase the film cooling performance, it is an indication that the coolant jet has separated from the wall surface. The Colban correlation does not have any mechanism to predict when jet separation occurs, which resulted in an over prediction of effectiveness at the highest blowing ratio, M=2.23.

Table 4.5: Experimental Parameters used for Flat Plate Adiabatic Effectiveness Testing

Experimental Parameter	Value
Mainstream Temperature	305 K
Mainstream Velocity	54.0 m/s
Turbulence Level	0.5 %
Coolant Temperature	250 K
Density Ratio	1.20
Reynolds Number Re_d	9000
Hole diameter	2.54 mm
Pitch spacing	8.0
Injection Angle (α)	30°

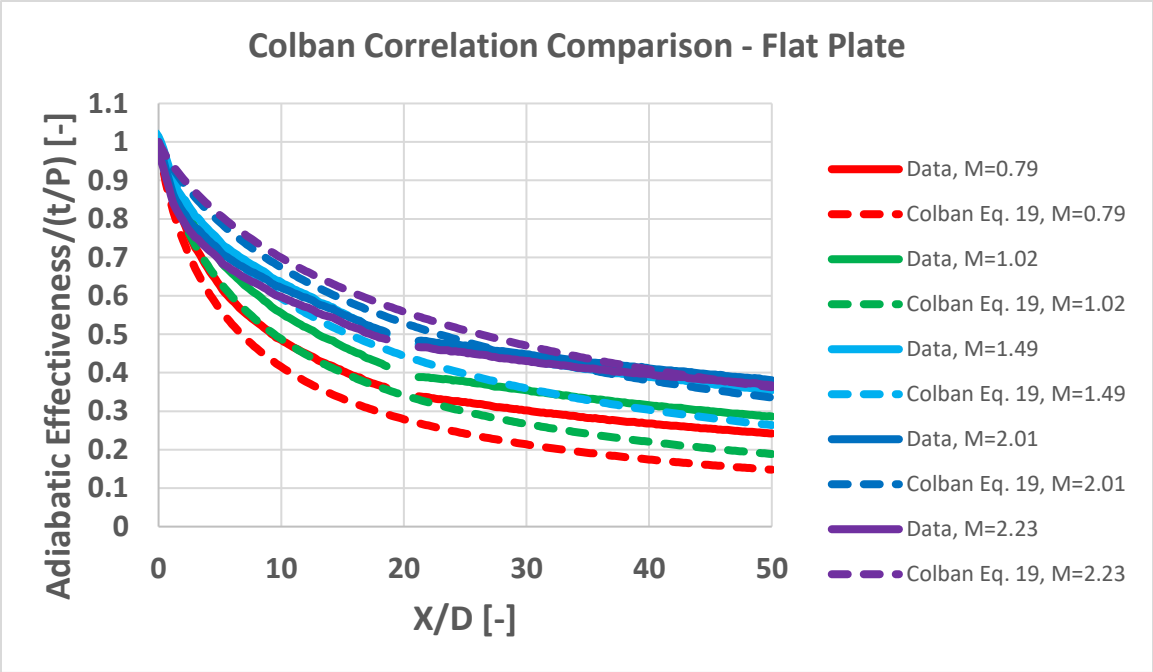

Figure 4.2: Comparison to Colban Correlation for laterally averaged adiabatic effectiveness from the flat plate test

In order to assess the performance of adiabatic effectiveness tests for each row measured individually on the vane model, the single row results were compared to the correlation developed by Colban et al [9]. While the correlation was built around flat plate data sets, comparisons to the single row test results can still provide a helpful baseline for evaluating the effect of model curvature on the film cooling performance. A schematic showing the location of each row tested is shown in Figure 2.7.

Because each suction side row tested a narrow range of blowing ratios, figures for these rows only included the minimum and maximum blowing ratios tested in order to improve readability. Measurements of laterally averaged adiabatic effectiveness for intermediate blowing ratios consistently fell in between the minimum and maximum blowing ratios tested on the suction side single rows. The film cooling performance on the suction side followed the expected trend of increasing effectiveness in areas of high convex curvature relative to flat plate predictions. For the first downstream suction side row, Row 12 (Figure 4.3), where the convex curvature is greatest ($\frac{2R}{d} = 68.7$) the laterally averaged adiabatic effectiveness substantially exceeded the predicted flat plate performance. At M =1.16, the averaged effectiveness was as much as 50% greater than the correlation prediction, up to 80D downstream. The averaged effectiveness was also improved for Row 13 (Figure 4.4), where the convex curvature was reduced relative to Row 12 but still significant ($\frac{2R}{d} = 79.1$). The averaged effectiveness for both blowing ratios was greater than predicted in the range of 20D to 60D. Row 14 (Figure 4.5) is further downstream in a low curvature area approaching flat plate conditions. The measured results at both

blowing ratios still exceeded the effectiveness predicted by the Colban correlation, but the difference was not as significant as it was for Rows 12 and 13 in areas of higher convex curvature. Considering these three cases together, the laterally averaged adiabatic effectiveness from the suction side single row tests follows the expected trend from convex curvature as previously explained by Ito and Goldstein

On the pressure side, Row 5 (Figure 4.6) was the only single row tested in an area of high concave curvature ($\frac{2R}{d} = 164.2$). The row was operated at fairly high blowing ratios up to M=3.0, and the average effectiveness underperformed relative to the flat plate prediction as would be expected. It should be noted that a small leak in the hatch downstream of Row 5 was observed during this test. A bump in effectiveness around 7D downstream can be observed in the laterally averaged plots. Since this leak would be expected to increase the effectiveness downstream, it can still be concluded that the high concave curvature for this row led to a decreased film cooling performance relative to the Colban correlation prediction. As the concave curvature became reduced farther downstream, the measured averaged effectiveness from Row 4 (Figure 4.7) matched up more closely to the Colban correlation at all blowing ratios tested. Data from this row between 35-40D has been removed due to an accidental change in the upstream camera positioning (AC655 #1) which led to contamination from the border of a viewing window. Rows 2 and 3 (Figures 4.8-9) produced laterally averaged adiabatic effectiveness results that were surprising, in that they significantly underperformed the Colban correlation predictions despite being in areas of low curvature approaching flat plate conditions on the pressure side. The initial averaged effectiveness at x/D=0 for Rows 2 and 3 were much

lower than would be expected based on coverage, which might indicate that the coolant was not filling out the diffuser fully. It should also be noted that the initial effectiveness at x/D=0 of Row 2 varied significantly with blowing ratio. This behavior was in contrast to the other single row tests which had a much narrower band of initial effectiveness values. The Colban correlation provides a helpful baseline expectation for shaped performance which makes identifying underperforming or otherwise unusual behaving rows an easier task.

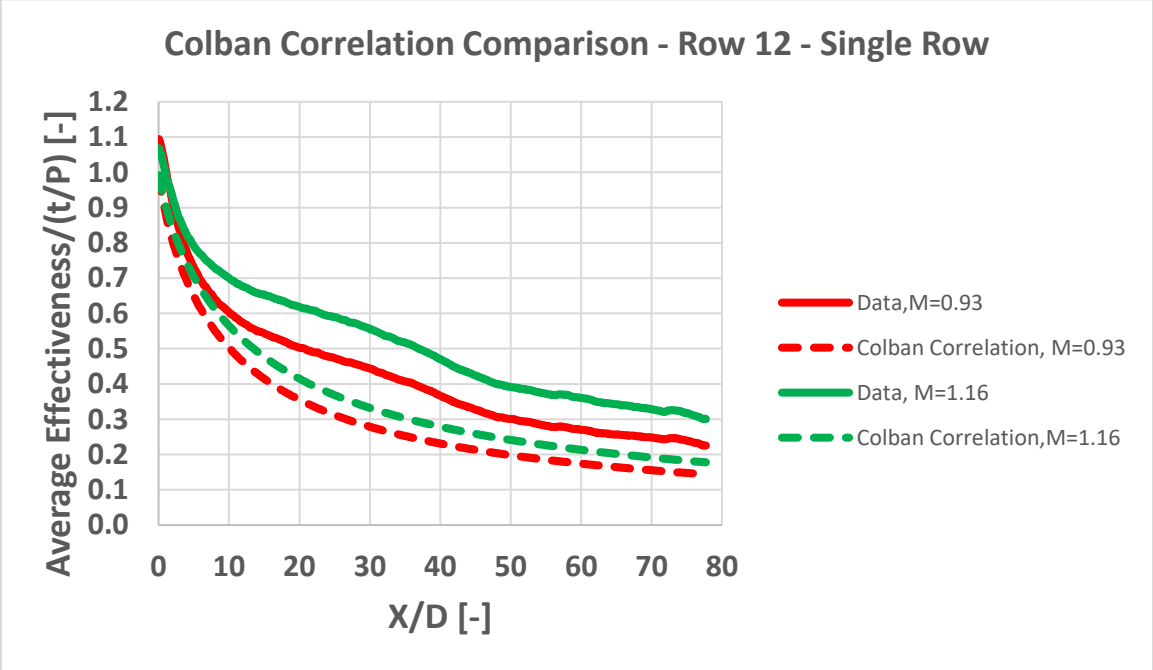

Figure 4.3: Comparison to Colban Correlation for laterally averaged adiabatic effectiveness from Row 12, single row test

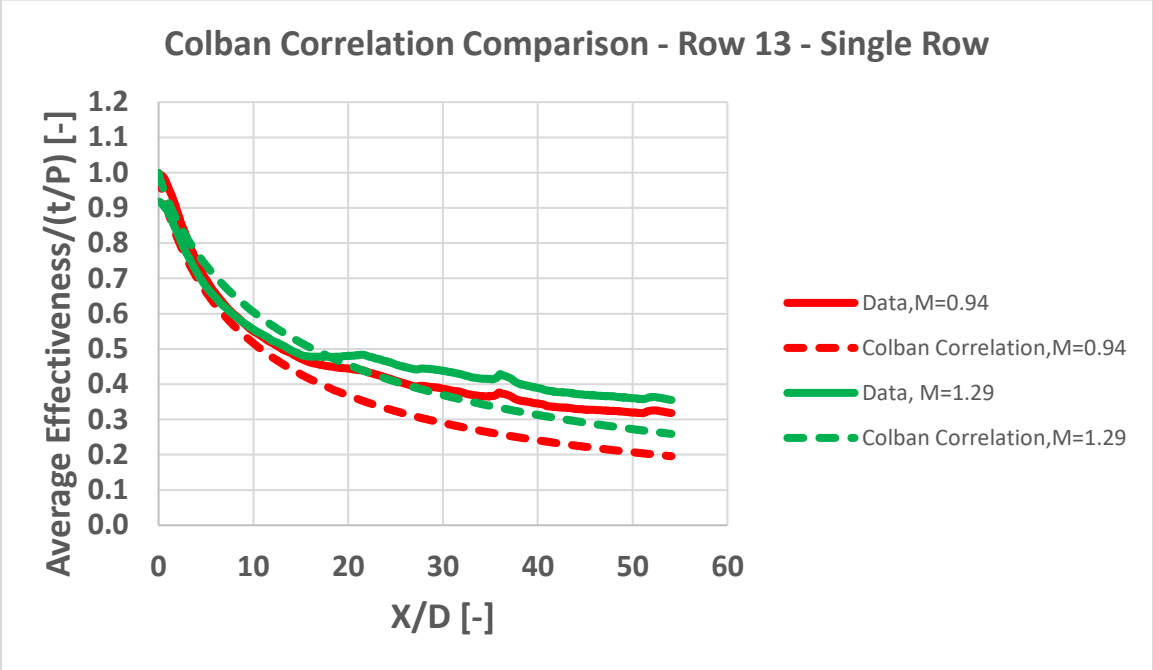

Figure 4.4: Comparison to Colban Correlation for laterally averaged adiabatic effectiveness from Row 13, single row test

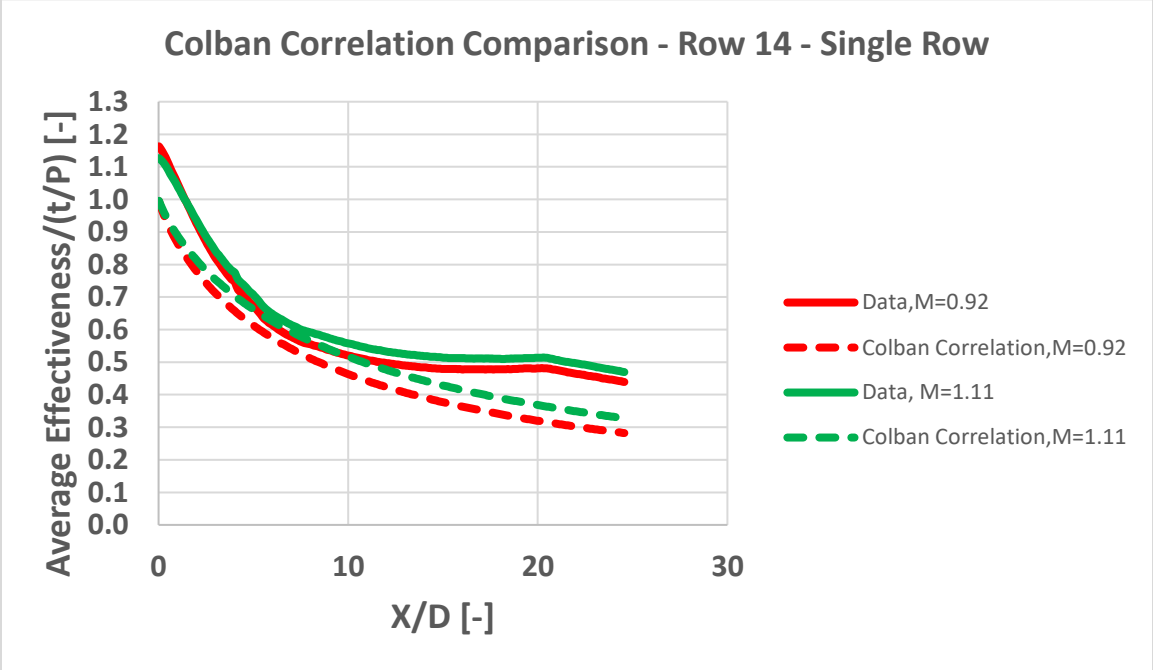

Figure 4.5: Comparison to Colban Correlation for laterally averaged adiabatic effectiveness from Row 14, single row test

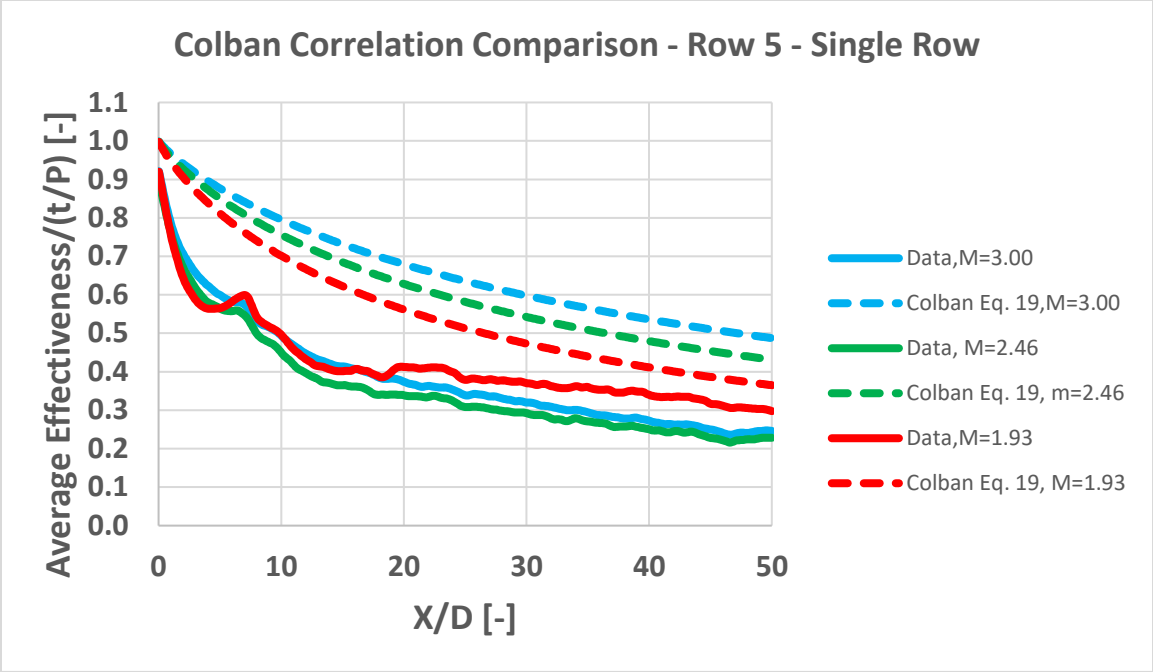

Figure 4.6: Comparison to Colban Correlation for laterally averaged adiabatic effectiveness from Row 5, single row test

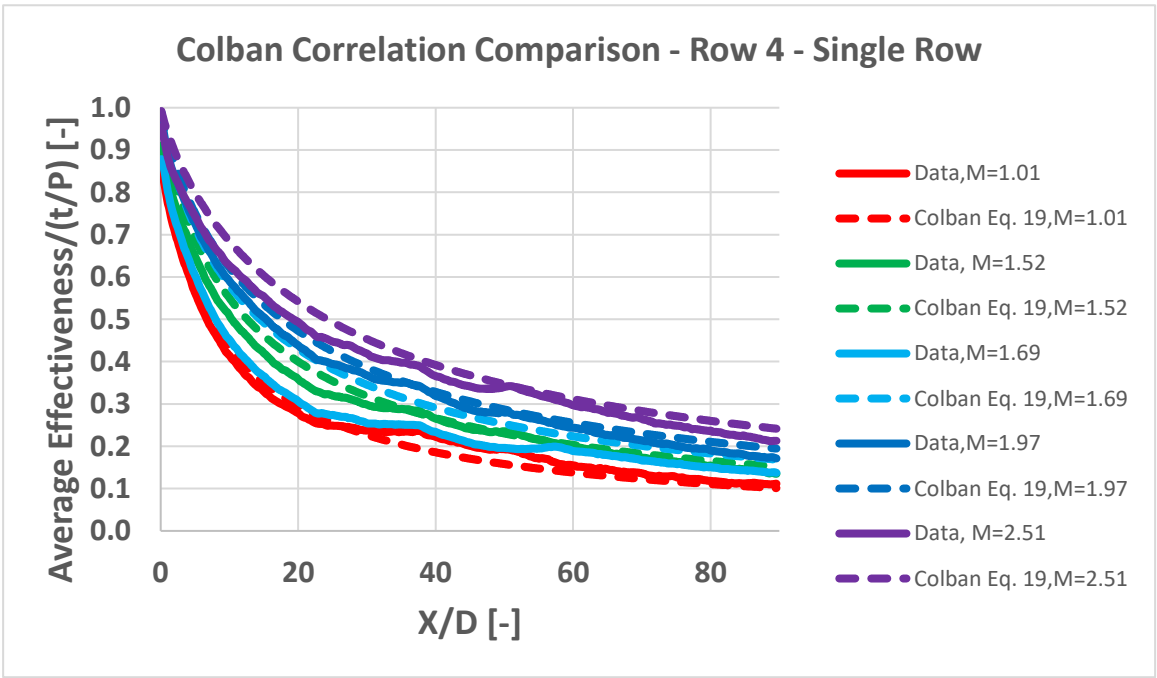

Figure 4.7: Comparison to Colban Correlation for laterally averaged adiabatic effectiveness from Row 4, single row test

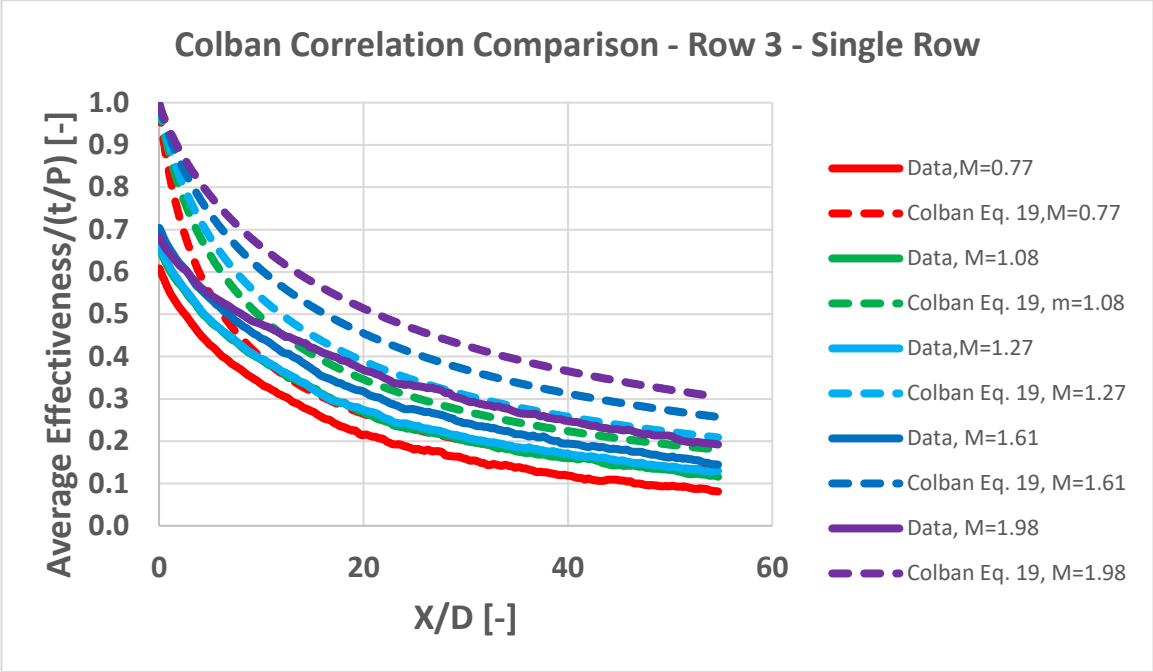

Figure 4.8: Comparison to Colban Correlation for laterally averaged adiabatic effectiveness from Row 3, single row test

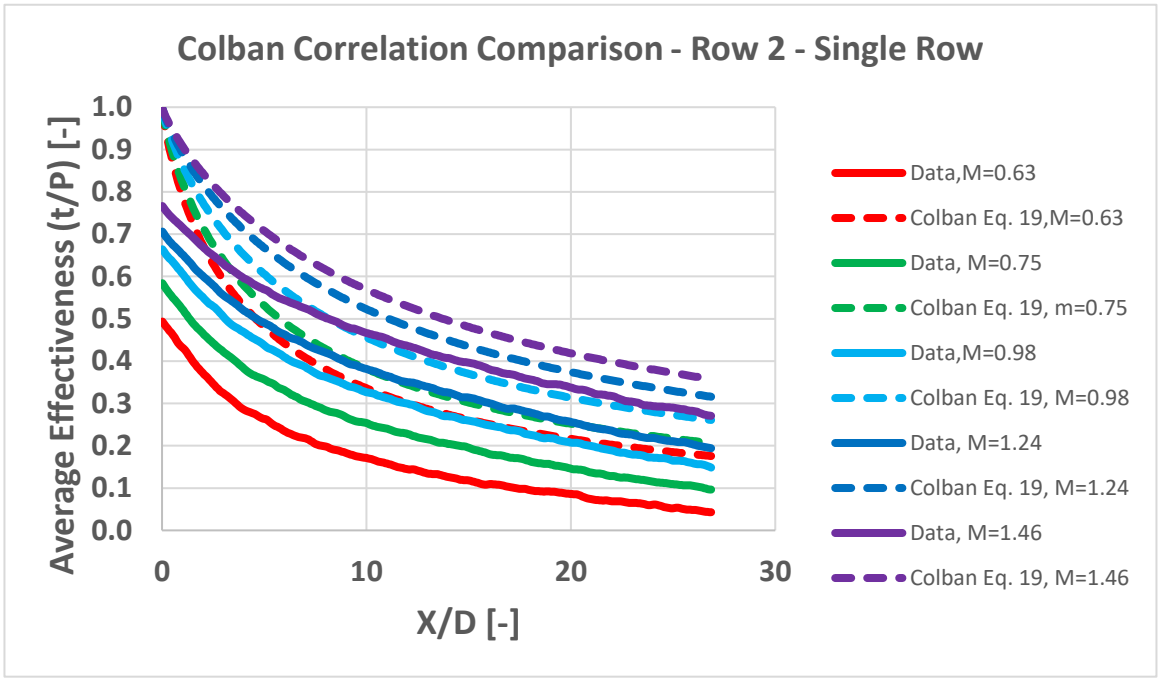

Figure 4.9: Comparison to Colban Correlation for laterally averaged adiabatic effectiveness from Row 2, single row test

4.2 - Comparison of Non-Showerhead and All Open Results

Two different configurations were tested in order to evaluate the impact of upstream showerhead cooling on the film cooling performance of rows downstream. The All Open and Non-Showerhead cases were performed at the Low Tu condition, and targeted the same blowing ratios for each set point tested. The laterally averaged results are shown across all rows in Figure 4.10 and 4.11 with and without showerhead cooling respectively. The presence of showerhead cooling produced different trends on the pressure and suction side of the vane model. For the All Open case, the film cooling performance increased with higher blowing ratios on the pressure side. However, on the suction side, effectiveness decreased at higher blowing ratios. This trend was not found in the non-showerhead case, where the film cooling performance increased with blowing ratio on both the pressure and suction sides. A comparison between these two tests at the lowest and highest blowing ratio conditions is shown in Figure 4.12. For the pressure side rows further downstream, Rows 1-4, showerhead cooling seems to have negligible effect at the low blowing ratio set point (S1), and actually decreases the performance relative to the non-showerhead test at the high blowing ratio set point (S5). The effect of showerhead cooling on the downstream suction side row (Row 14) seems to improve the average effectiveness at low blowing ratios, and decrease effectiveness at high blowing ratios.

Cutbirth and Bogard [34] evaluated the film cooling performance with and without showerhead cooling on the pressure side of a turbine vane with compound angle cylindrical holes. Measurements showed decreased peak values of adiabatic effectiveness with showerhead cooling. The pressure side was found to be subjected to higher turbulence

levels caused by the showerhead injection, which resulted in a greater dispersion of the pressure side coolant jets. The introduction of showerhead cooling has positive and negative contributing factors to the film cooling performance downstream. A benefit of showerhead cooling is the additional upstream coolant which can mix with coolant jets and create a more uniform lateral coverage of coolant. A potential downside of showerhead injection is that rows downstream will have a thicker and more turbulent approach boundary layer. This could result in a more rapid degradation of the adiabatic effectiveness, by augmenting the dispersion of the coolant jets mixing into the mainstream flow. The comparison between All Open and Non-showerhead cases indicates that the benefits of additional showerhead coolant on this test model were not observed far downstream, while the change in the approach boundary layer had a negative effect on effectiveness far downstream on both sides of the vane model.

A few studies have compared the performance with and without showerhead blowing on a vane model with axial laidback fanshaped holes. Colban et al. [18] found that the presence of showerhead cooling on the first pressure side row increased the effectiveness, but did not provide any results further downstream or on the suction side. Gao et al. [14] compared the cases with and without showerhead cooling for a full coverage turbine blade. The film effectiveness for several rows on the pressure and suction side was improved by the showerhead film cooling at an averaged blowing ratio of M=0.9 and 1.2. It is hard to compare results from this study without knowing the specific range of blowing ratios tested, and it is unclear if this trend would have continued at higher blowing ratios. Kinell et al. [20] also reported an improvement in effectiveness due to showerhead cooling,

although their attempt at superposition over predicted the measured effectiveness with combined showerhead cooling. The results of this study are at least partially in conflict with similar comparisons in the literature of the film cooling performance with and without showerhead cooling. The showerhead does introduce additional coolant which can mix with the coolant jets of rows downstream and fill in the gaps in coverage between holes. However, this additional coolant provided by showerhead injection, at least for this test model, does not seem to sufficiently counteract the degradation caused by a thicker and more turbulent boundary layer further downstream.

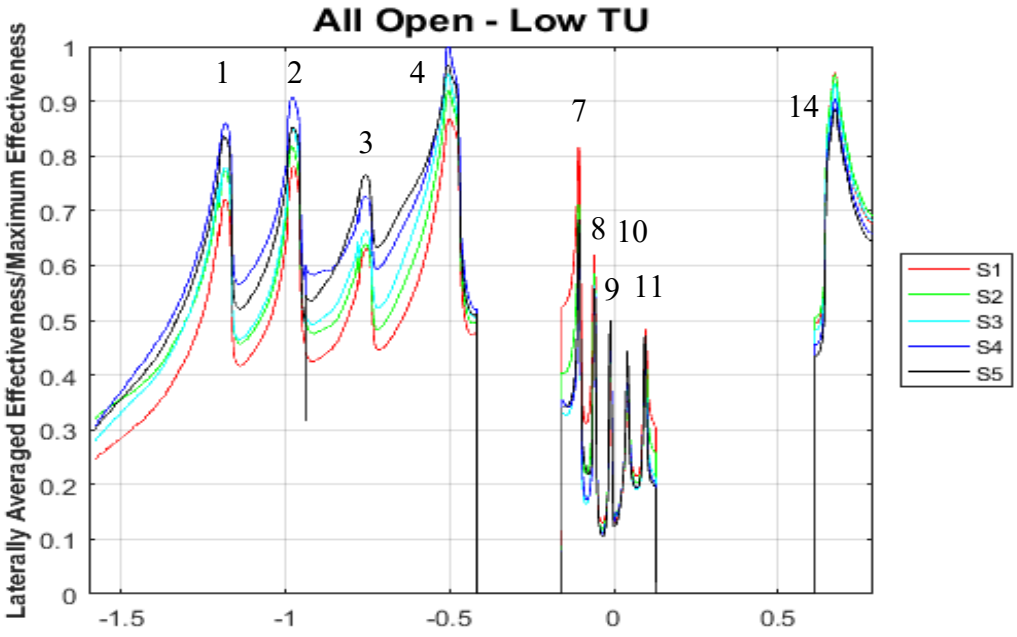

Figure 4.10: Laterally averaged effectiveness in the All Open configuration at Low Tu across the full span of the test model with row numbers indicated

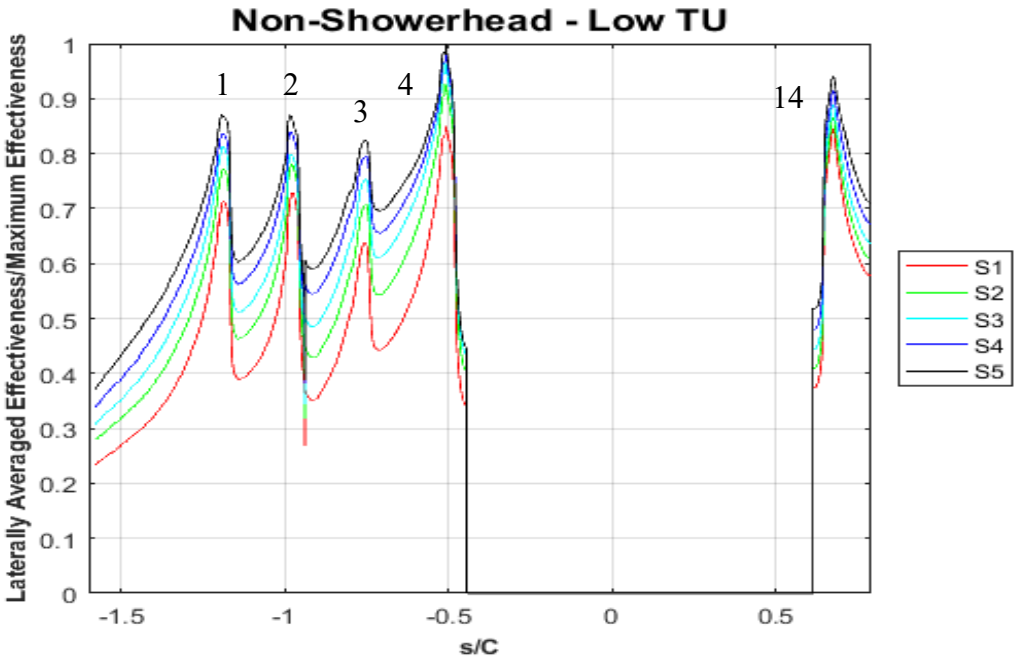

Figure 4.11: Laterally averaged effectiveness in the Non-Showerhead configuration at Low Tu across the full span of the test model with row numbers indicated

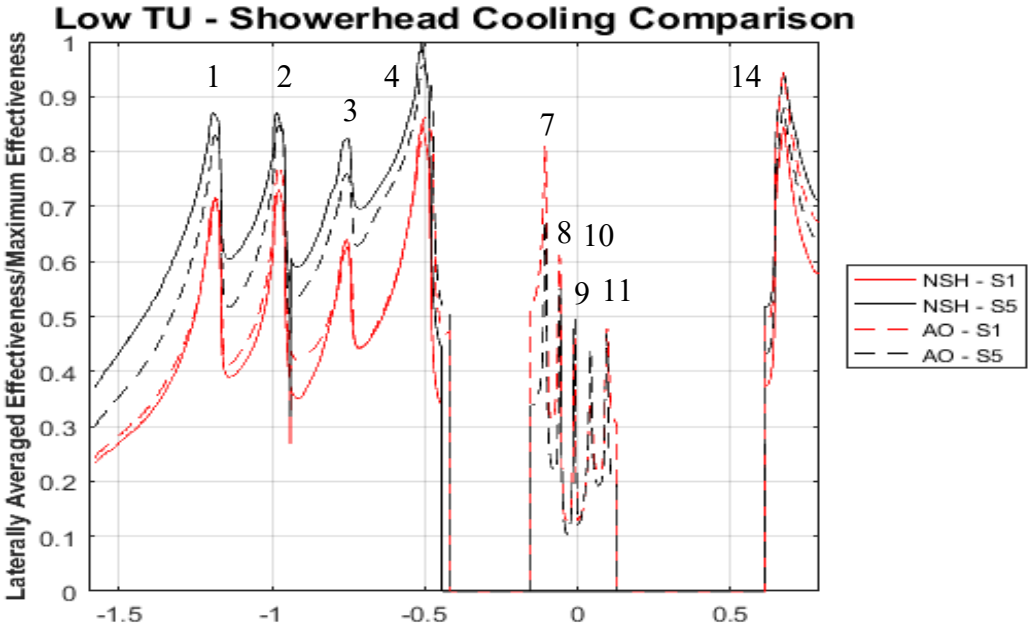

Figure 4.12: Comparison of All Open and Non-Showerhead cases at the lowest and highest blowing ratios tested with row numbers indicated

For Row 4 (Figure 4.13), with the exception of the lowest blowing ratio where the two cases are very similar, the effectiveness without showerhead cooling is slightly higher. A similar trend was found for the three pressure side rows further downstream (Figures 4.14-16). In each case, the non-showerhead and all open results were similar at the low blowing ratios, but as the blowing ratio increased the effectiveness with showerhead cooling would begin to underperform. For Rows 1-4, the greatest difference between the two test cases was found at the highest blowing ratios.

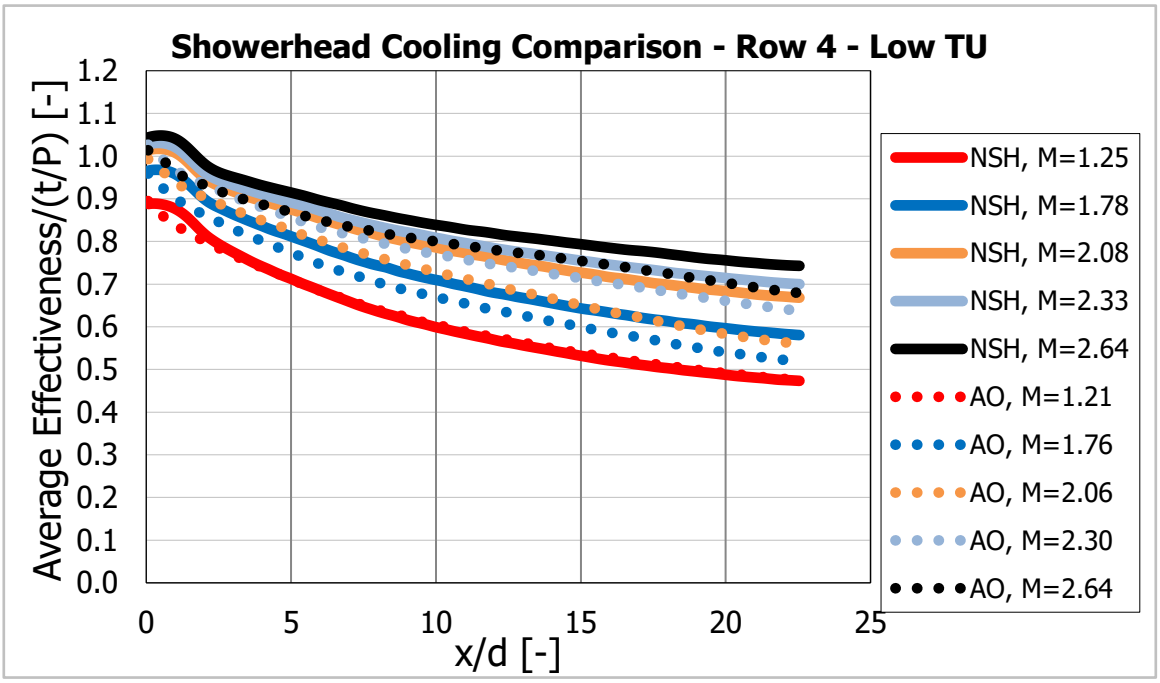

Figure 4.13: Comparison of All Open and Non-Showerhead cases for Row 4

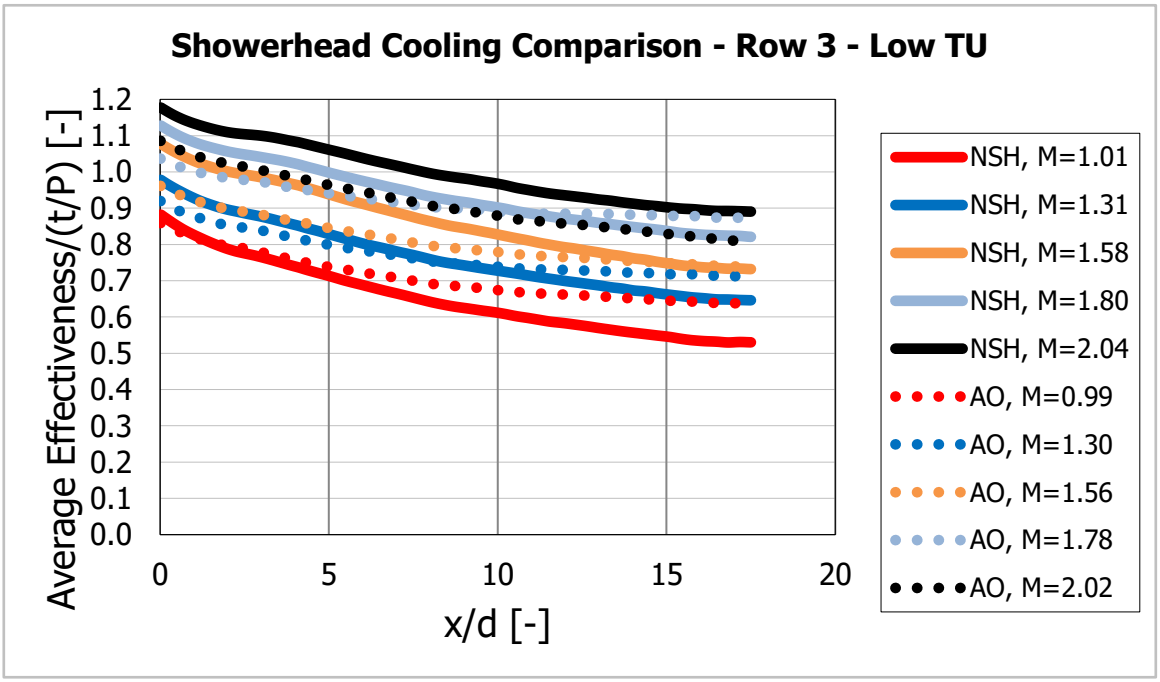

Figure 4.14: Comparison of All Open and Non-Showerhead cases for Row 3

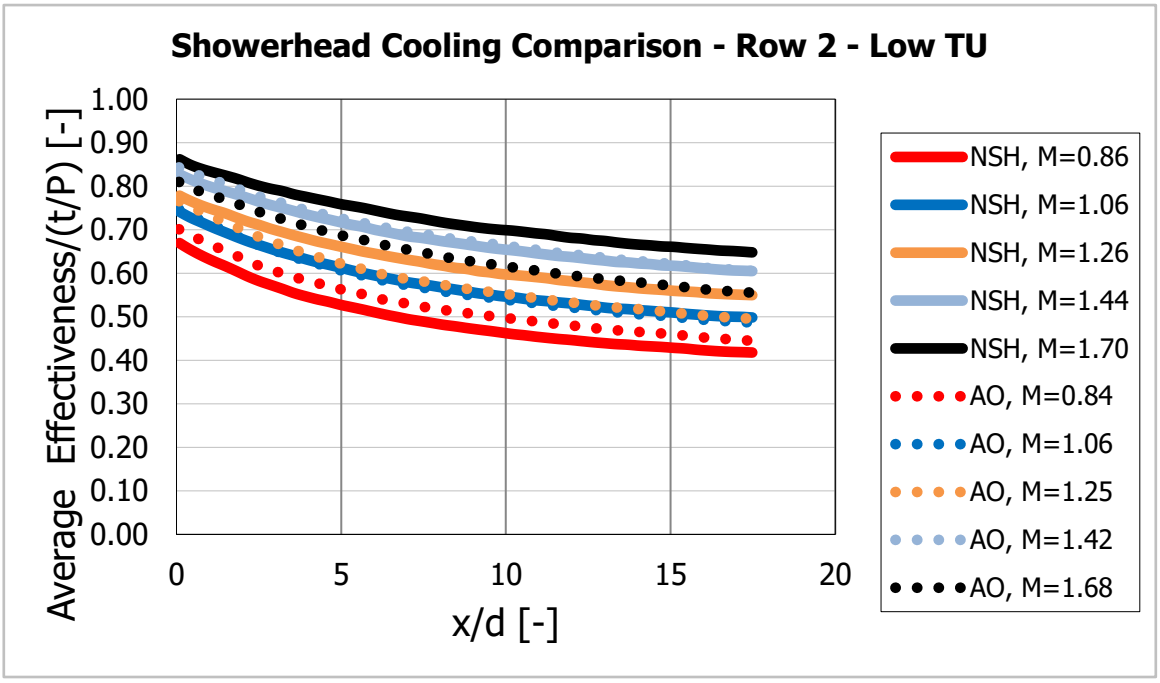

Figure 4.15: Comparison of All Open and Non-Showerhead cases for Row 2

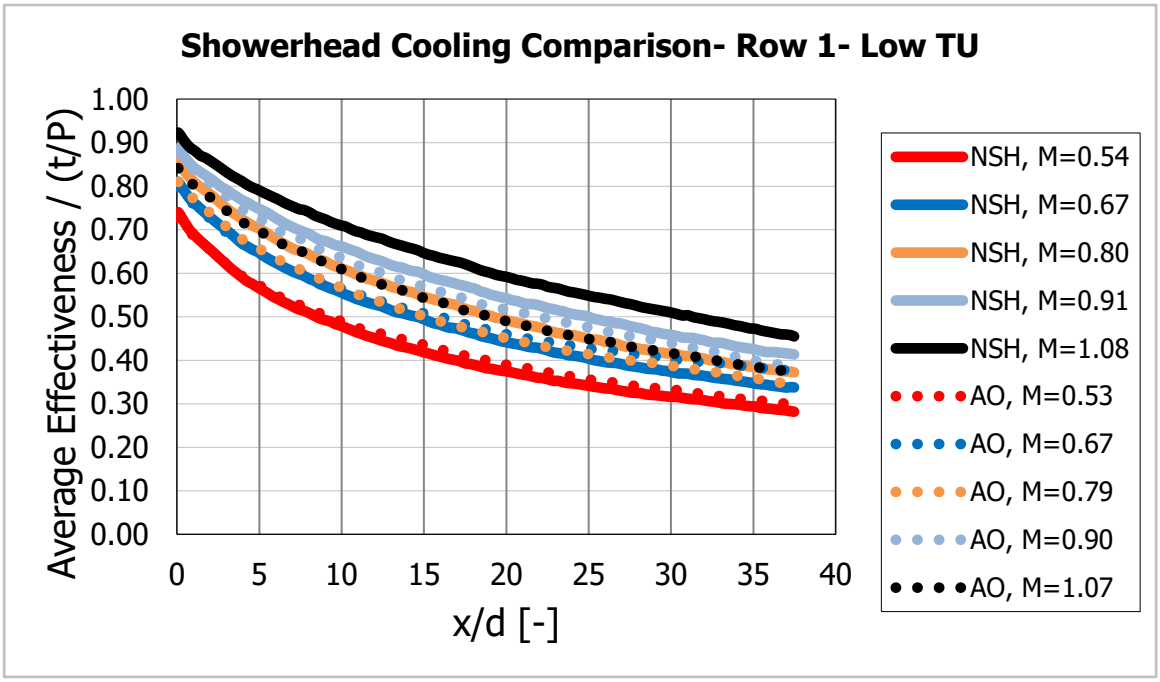

Figure 4.16: Comparison of All Open and Non-Showerhead cases for Row 1

One interesting result of comparing the full coverage tests with and without showerhead cooling was that, on the suction side, the laterally averaged adiabatic effectiveness measured had different trends with blowing ratio in the Non-Showerhead and All Open cases. Without showerhead cooling, effectiveness uniformly increased with higher blowing ratios, but with showerhead cooling, effectiveness would begin to decrease with higher flow rates. For Row 14 (Figures 4.17), the All Open case would perform better at low blowing ratios, but would fall below the Non-Showerhead case at higher blowing ratios. The decrease in effectiveness at higher blowing ratios could be a result of changes to the boundary layer caused by showerhead injection. Making measurements of the boundary layer with and without showerhead cooling in future studies would help to more definitively quantify this effect.

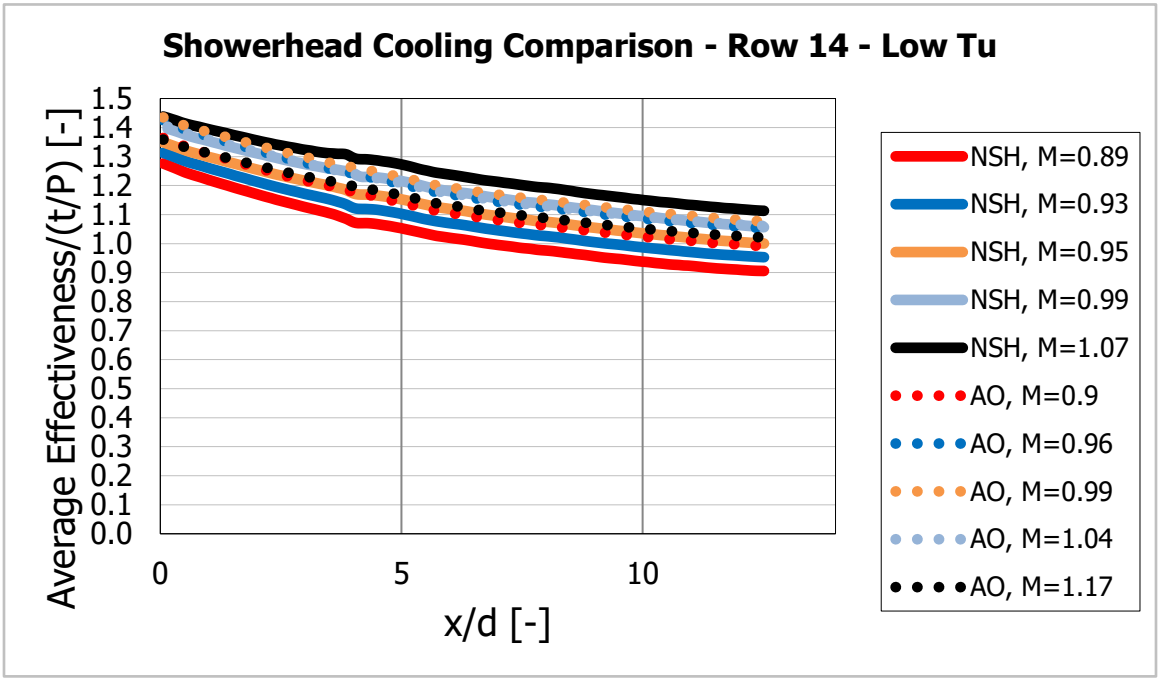

Figure 4.17: Comparison of All Open and Non-Showerhead cases for Row 14

4.3 - Effect of Increasing Mainstream Turbulence

A repeat of the All Open configuration adiabatic effectiveness test was performed with the turbulence grid previously described installed in order to raise the mainstream turbulence level from 0.5% to 7.5%. The two tests had the same mass flow rate targets, and tested a similar range of blowing ratios between both cases. Figure 4.18 shows the high turbulence results across the full span of the vane model viewing area. In general, higher mainstream turbulence levels seemed to moderately diminish average effectiveness levels at low blowing ratios, but the effect became negligible at higher blowing ratios shown in Figure 4.19. A comparison between the low and high Tu tests for each individual row has also been plotted in Figures 4.20-29. Rows further downstream on the pressure side

experienced a slight reduction at low blowing ratios, but at higher blowing ratios the performance was comparable and in some cases improved relative to the Low Tu baseline. Further downstream on the suction side, the effectiveness of Row 14 was reduced for all blowing ratios. For the showerhead rows, increasing the mainstream turbulence level had a mixed effect. The performance of Rows 8 and 9 was improved at high Tu, especially for Row 9 which is located on the stagnation line. In contrast, Rows 7, 10 and 11 all had reduced performance at higher Tu, the effect being strongest for Row 7 on the pressure side.

Results from this study are mostly consistent with the data available in the literature as reported by Saumweber et al. [13] and Liu et al. [14]. The main trend from the laterally averaged results from laidback fanshaped holes was a significant decrease from high turbulence at low blowing ratios which becomes negligible at high blowing ratios. In general, the potential benefits of high turbulence do not affect shaped holes because the coolant jets are more likely to stay attached at high blowing ratios and already have sufficient lateral expansion. A few cases were reported where the effectiveness actually improved at high Tu, which was inconsistent with previously reported results. For most of these cases on the suction side, the gains were small and fell within the uncertainty of the adiabatic effectiveness measurement. However, several pressure side rows (Rows 2-4) appeared to have more significant gains at intermediate blowing ratios, which might be an interesting subject for further testing to verify this effect.

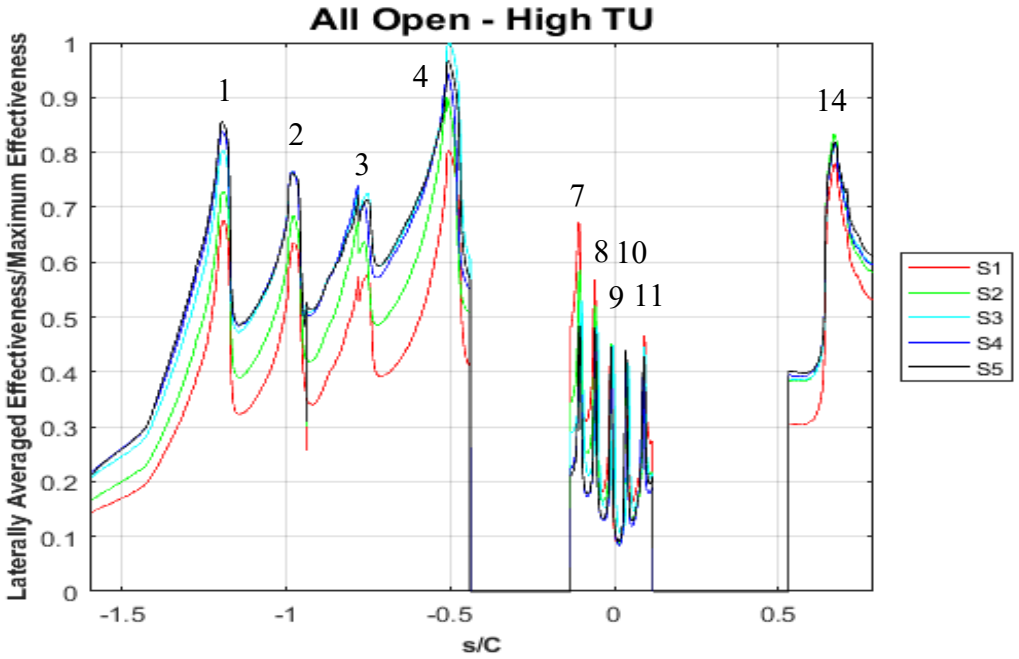

Figure 4.18: Laterally averaged effectiveness in the All Open configuration at High Tu across the full span of the test model with row numbers indicated

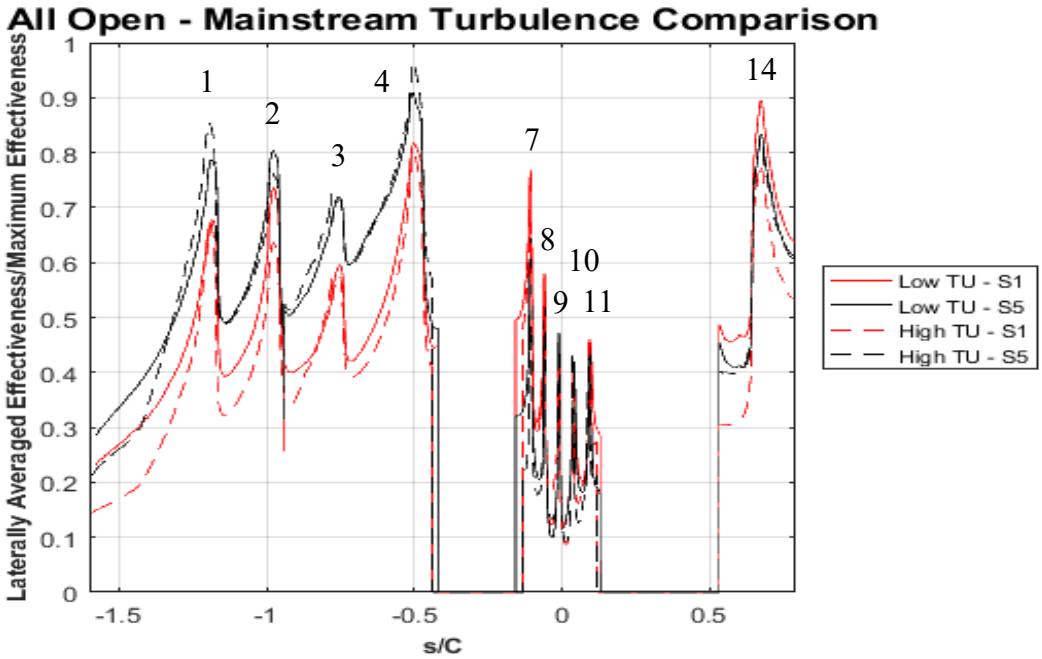

Figure 4.19: Comparison of the All Open Low and High Tu cases at the lowest and highest blowing ratios tested with row numbers indicated

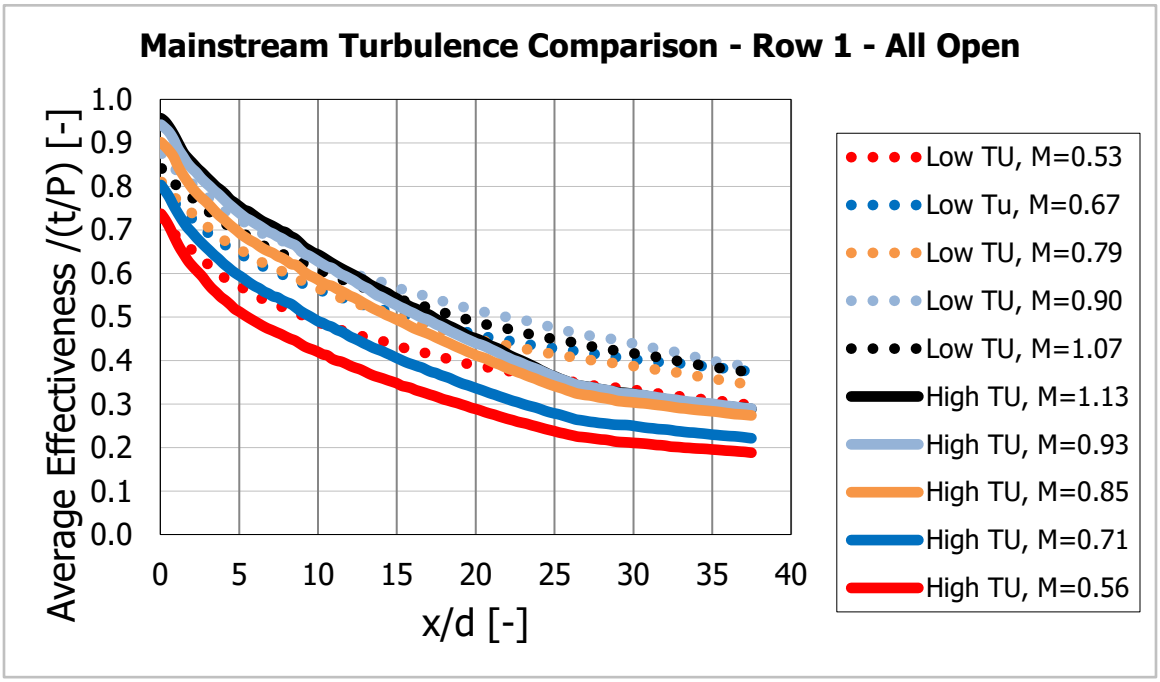

Figure 4.20: Comparison of the All Open Low and High Tu cases for Row 1

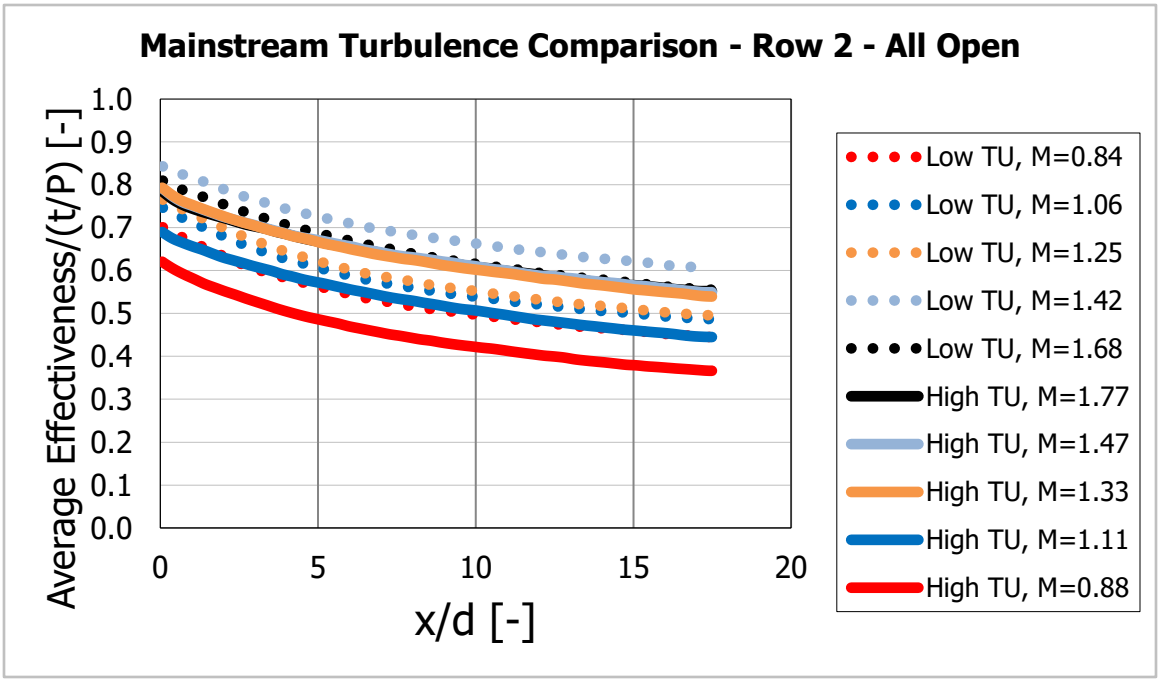

Figure 4.21: Comparison of the All Open Low and High Tu cases for Row 2

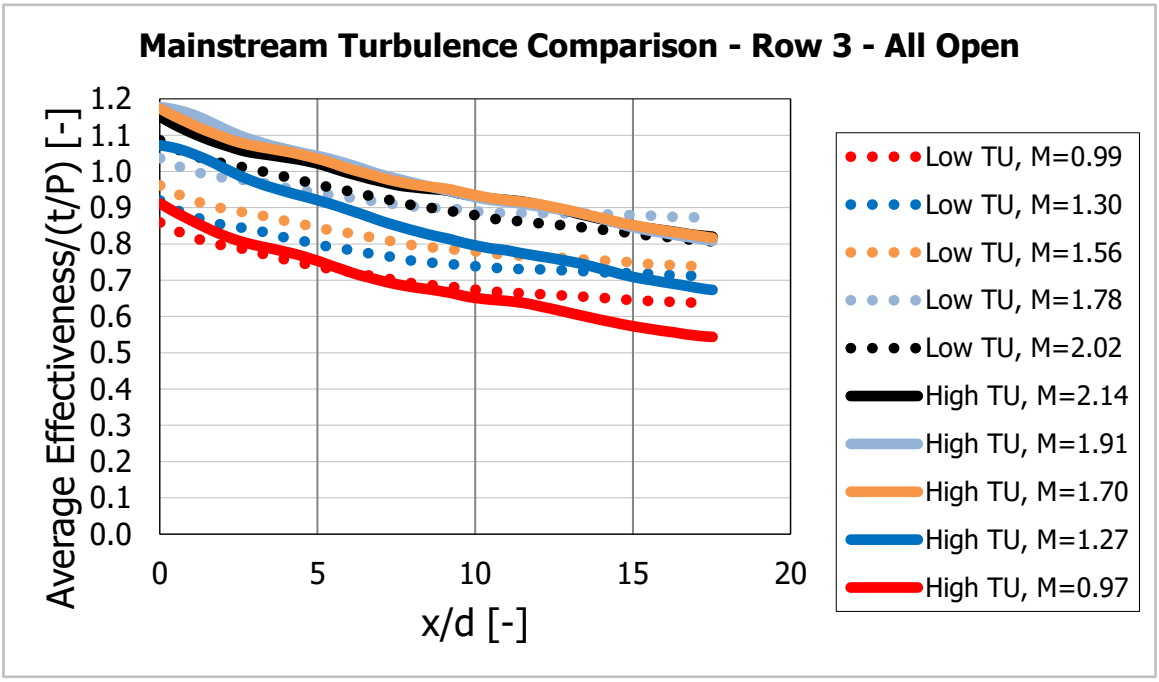

Figure 4.22: Comparison of the All Open Low and High Tu cases for Row 3

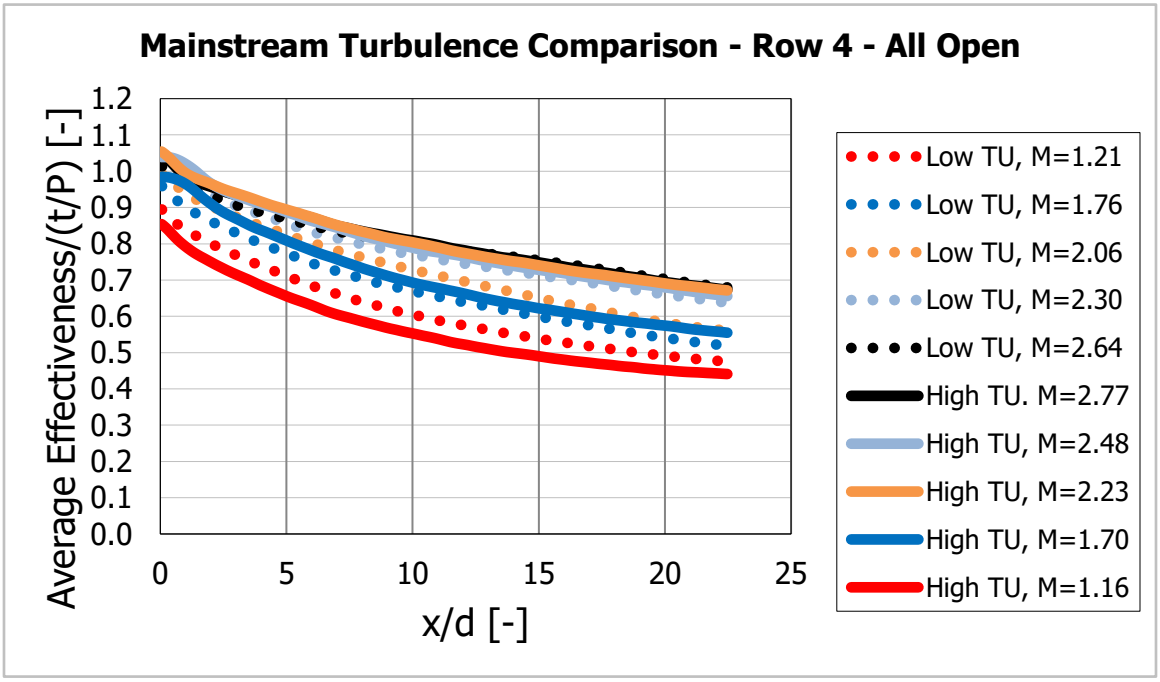

Figure 4.23: Comparison of the All Open Low and High Tu cases for Row 4

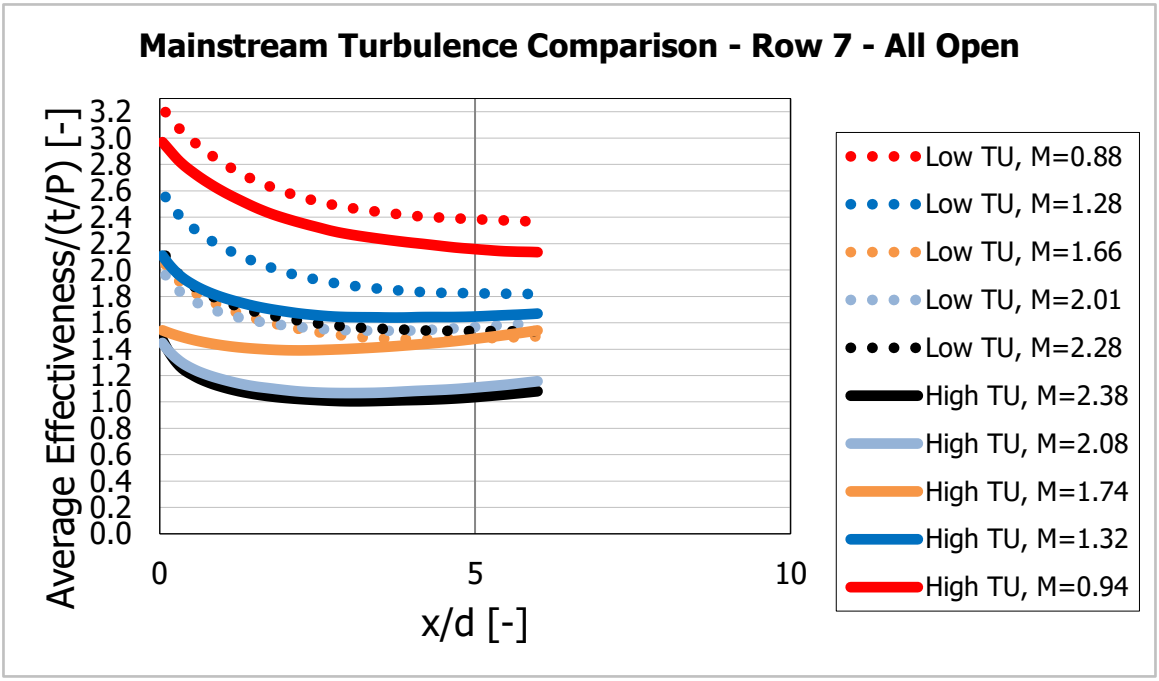

Figure 4.24: Comparison of the All Open Low and High Tu cases for Row 7

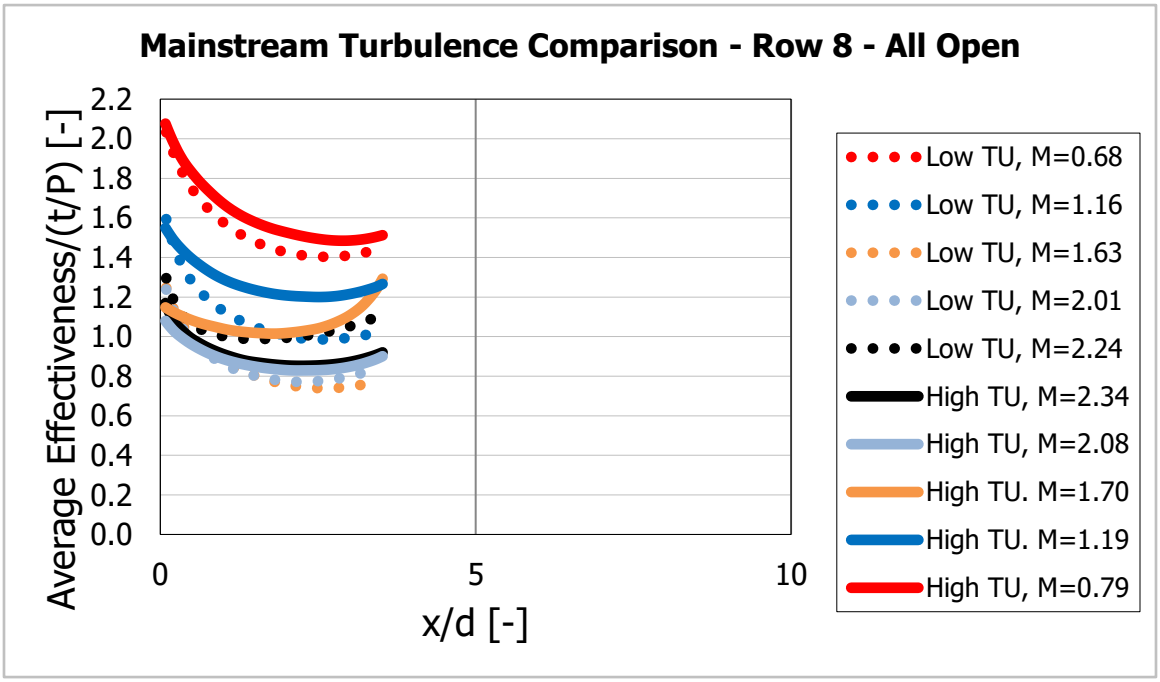

Figure 4.25: Comparison of the All Open Low and High Tu cases for Row 8

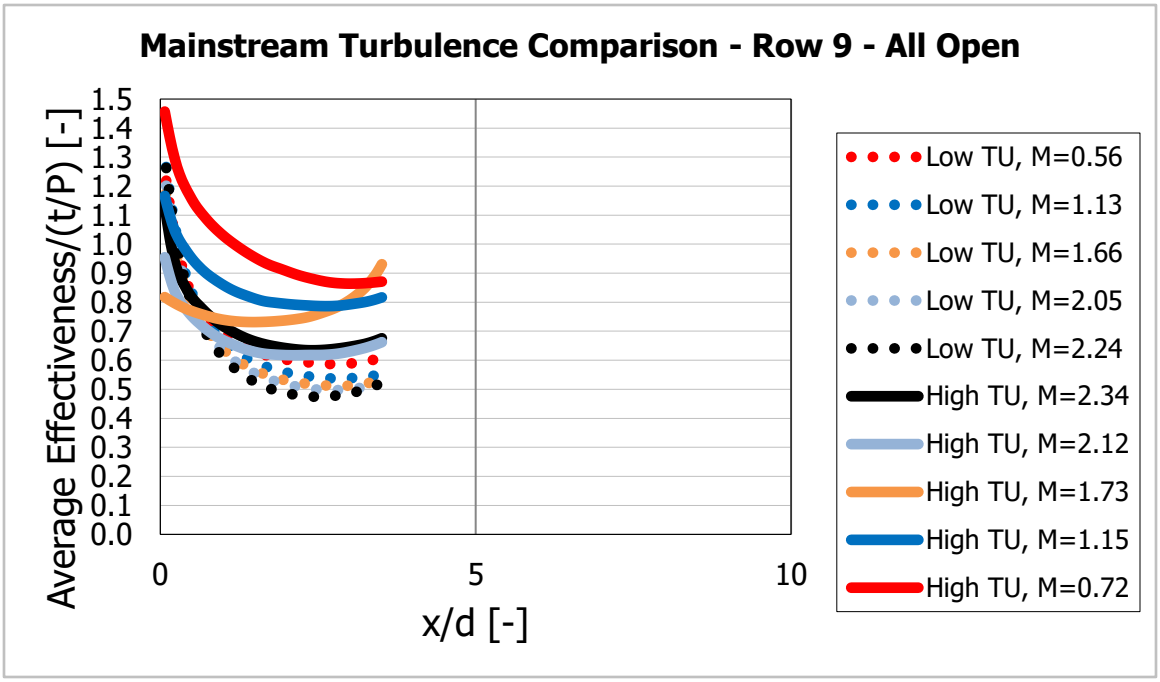

Figure 4.26: Comparison of the All Open Low and High Tu cases for Row 9

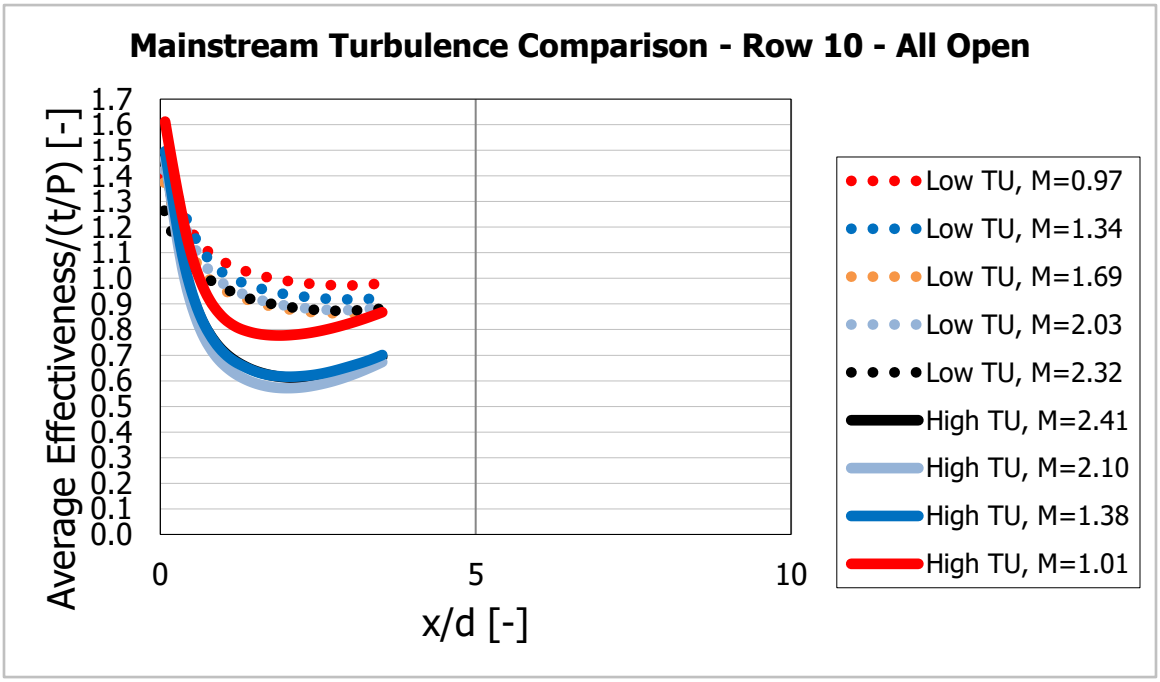

Figure 4.27: Comparison of the All Open Low and High Tu cases for Row 10

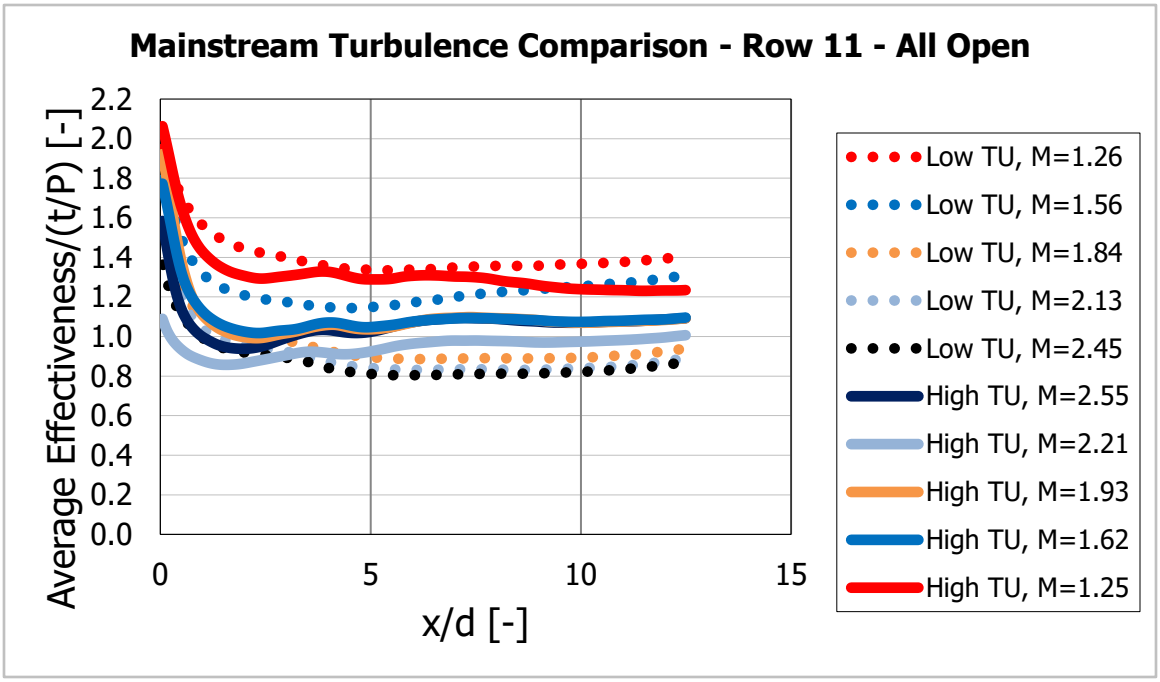

Figure 4.28: Comparison of the All Open Low and High Tu cases for Row 11

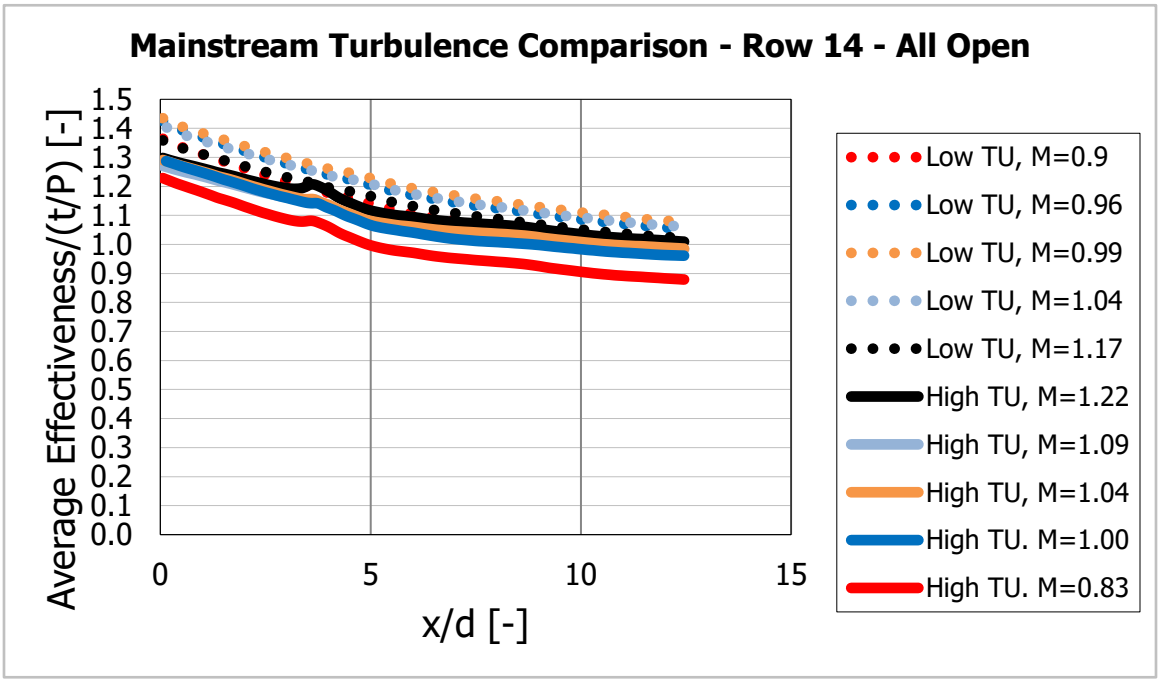

Figure 4.29: Comparison of the All Open Low and High Tu cases for Row 14

Chapter 5 – Conclusions

A series of adiabatic effectiveness measurements were carried out for single row and full coverage coolant configurations on a scaled turbine vane model. The goal of this study was to make comparisons between different test cases in order to evaluate the effect of local curvature, showerhead cooling, and mainstream turbulence levels. The vane model has a configuration of five rows of cylindrical holes in the showerhead region and 10 rows of laidback fanshaped holes on the pressure and suction side. The test model also employed a contoured endwall and adjustable sidewalls in order to more closely match the pressure distribution of engine conditions. Results have been presented in the form of laterally averaged adiabatic effectiveness.

5.1 – Adiabatic Effectiveness Measurements

Four rows on the pressure side and three rows on the suction side were tested individually in order to assess the effect of local curvature on their performance. A correlation from Colban et al. [9] was used as a baseline of the performance which would be expected on a flat plate. Results from the single row tests largely agreed with the expected effects from the normal pressure gradient resultant from convex and concave curvature, as outlined by Ito et al. [10]. Rows in areas of high concave curvature on the pressure side under performed relative to the flat plate baseline, while rows in areas of high convex curvature on the suction side over performed relative to the flat plat baseline. While keeping the expected effects of local curvature in mind, the Colban correlation proved to

be a helpful tool for setting expectations for a single row of laidback fanshaped holes on the test model.

Two full coverage coolant configurations with and without showerhead cooling provided a comparison for evaluating the effect of showerhead injection on the adiabatic effectiveness measured downstream. Overall, showerhead cooling for this test model had a negligible or slightly detrimental effect far downstream on both the pressure and suction side. The results of this comparison are partially in conflict with other data in the literature which shows a more global increase in effectiveness with showerhead cooling. Two factors introduced by showerhead cooling had a competing effect on the film cooling performance. Additional coolant was provided which could mix with coolant jets downstream and create a more uniform lateral coverage of coolant. On the other hand, showerhead cooling results in a thicker and more turbulent approach boundary layer for rows downstream, which may have contributed to the degradation in performance seen for rows far downstream when comparing the All Open and Non-showerhead cases.

The All Open test was repeated with a turbulence grid in place which raised the mainstream turbulence level from Tu=0.5% to 7.5%. In general, average effectiveness levels were diminished at higher turbulence levels, but this effect became less pronounced at higher flow rates. Results from this study are consistent with data in the literature on the effects of turbulence on shaped holes, although there were a few exceptions. A few cases were reported where the effectiveness was actually improved at higher turbulence. Most of these cases were within the experimental uncertainty, but a few rows on the pressure side

experienced more significant gains from higher turbulence levels at moderate blowing ratios.

5.2 – Recommendations for Future Work

During single row testing, it was found that the coolant was significantly warming, as much as 15-20K, between entering the inlet ducts and exiting onto the model surface. This was attributed to the low flow rates used during single row testing. This amount of warming was still quite unusual considering the low thermal conductivity of the foam used in the vane model. A more thorough investigation into this phenomenon, either through more testing at low flow rates or COMSOL simulations, would be an interesting subject of future study. Another good practice for future tests would be to place thermocouples at the metering holes close to whichever holes are being used for imaging, in order to have another indicator of the coolant temperature closer to the point of discharge.

Appendix – Spatially Dependent IR Temperature Calibrations

Camera	Thermocouple	Location, S/C`	Slope, M	Intercept, B
SC325	1	-1.43	1.45	-136.23
SC325	2	-1.21	1.74	-225.92
SC325	3	-0.99	1.70	-214.69

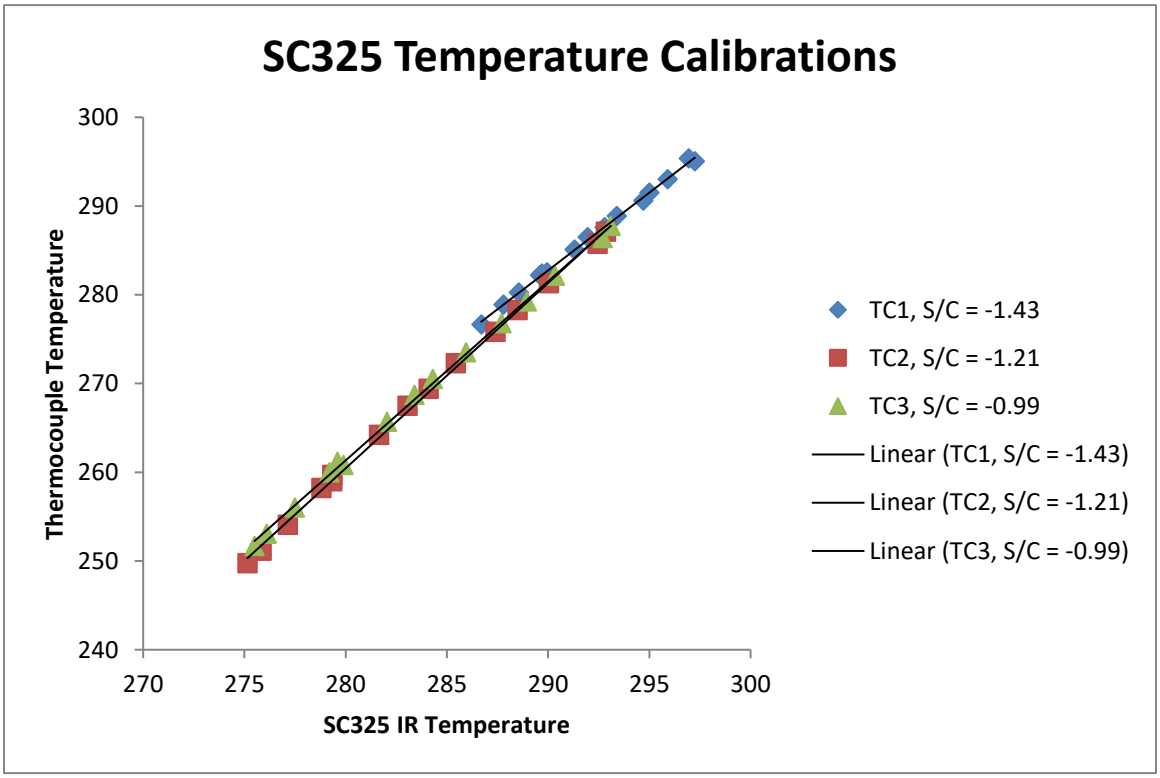

Camera	Thermocouple	Location, S/C`	Slope, M	Intercept, B
AC655 #1	1	0.09	1.39	-120.16
AC655 #1	2	0.04	1.34	-105.07
AC655 #1	3	-0.02	1.27	-84.44
AC655 #1	4	-0.06	1.24	-74.68
AC655 #1	5	-0.11	1.28	-87.54
AC655 #1	6	-0.24	1.43	-132.33
AC655 #1	7	-0.33	1.39	-123.18
AC655 #1	8	-0.51	1.44	-135.47
AC655 #1	9	-0.78	1.49	-150.26

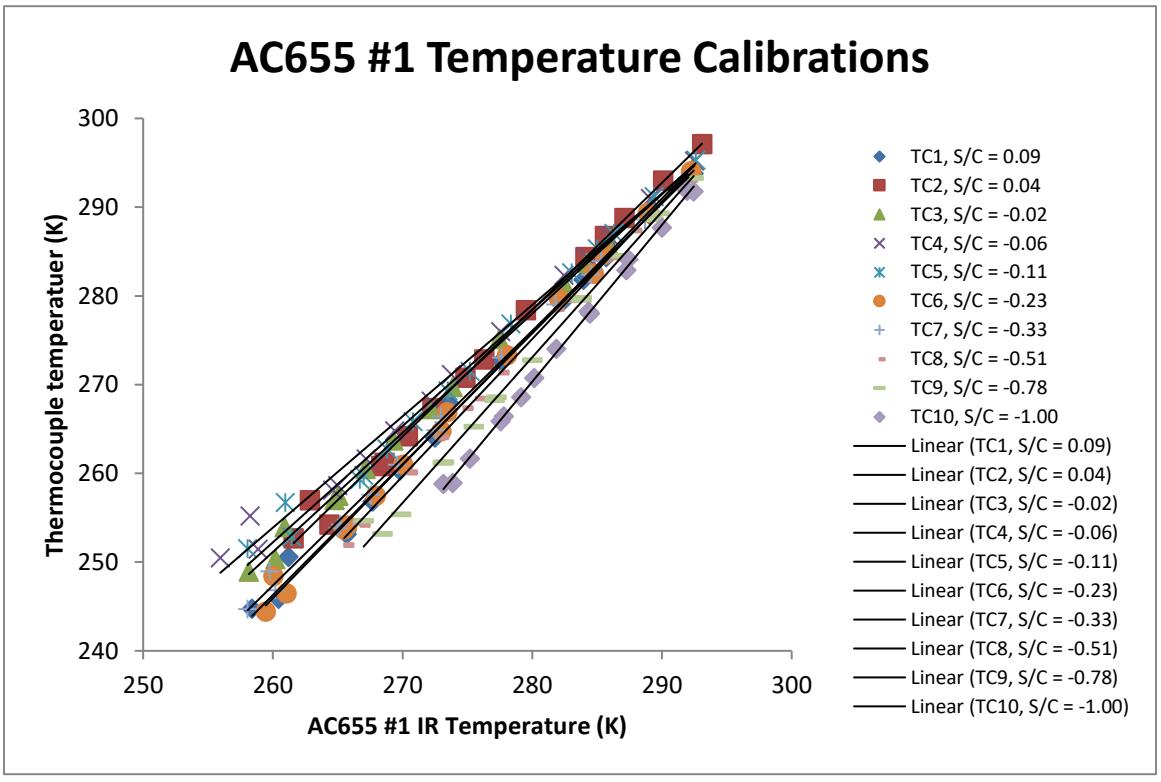

Camera	Thermocouple	Location, S/C`	Slope, M	Intercept, B
T620	1	0.43	1.33	-105.63
T620	2	0.09	1.38	-118.11
T620	3	0.04	1.36	-112.54
T620	4	0.27	1.37	-114.05

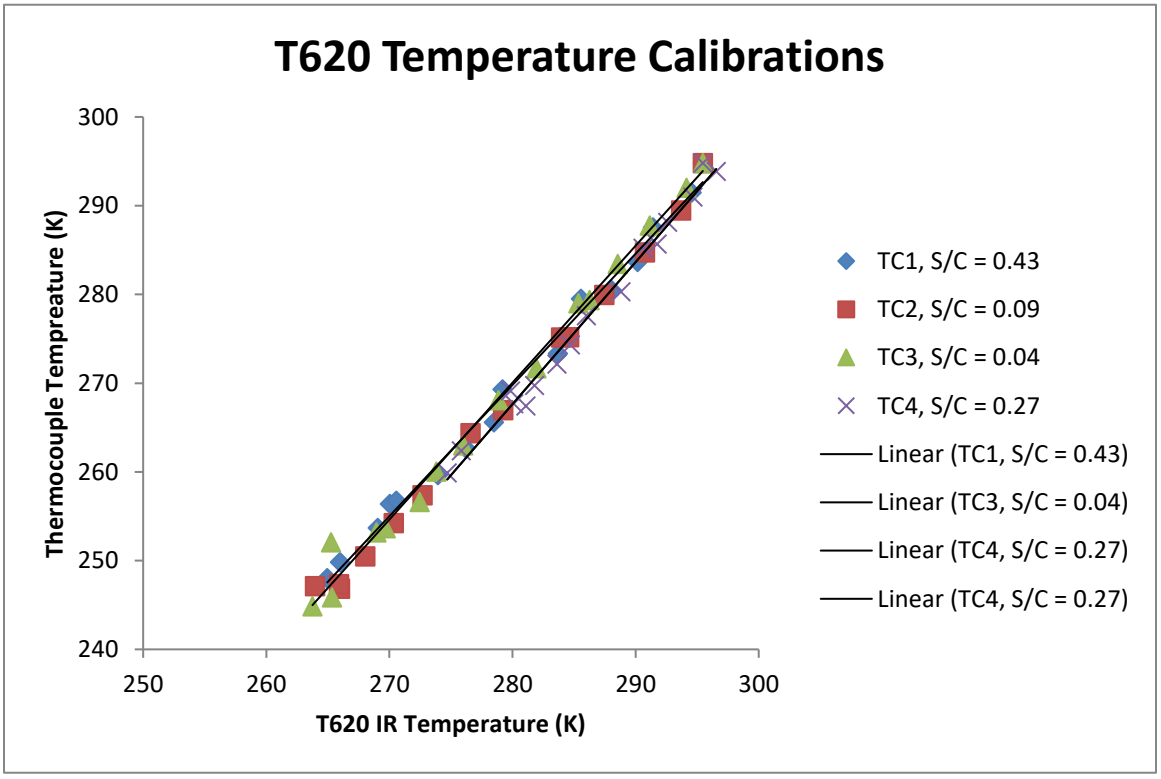

Camera	Thermocouple	Location, S/C`	Slope, M	Intercept, B
AC655 #2	1	0.53	0.76	72.19
AC655 #2	2	0.68	0.88	33.64
AC655 #2	3	0.86	0.92	23.86

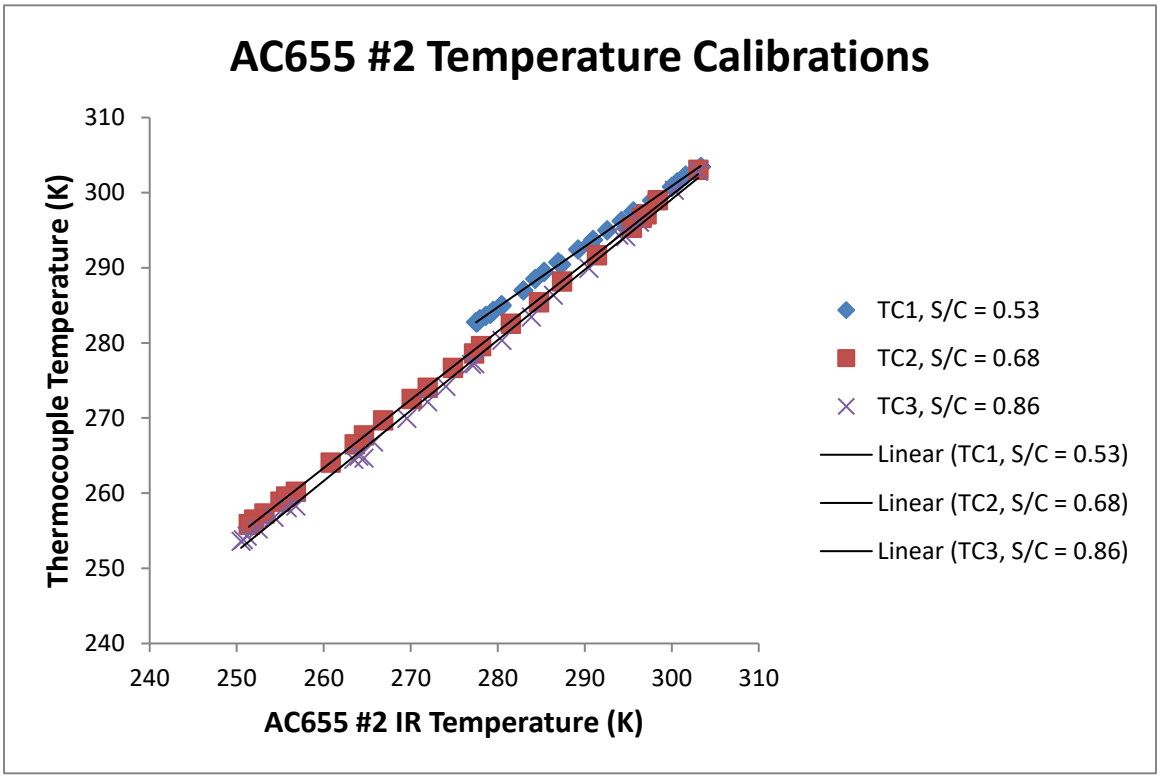

Bibliography

1. General Electric. *Heavy Duty Gas Turbine Products.* 2009. http://site.ge-energy.com/prod_serv/products/gas_turbines_cc/en/downloads/GEH12985H.pdf (accessed 10 31, 2013).
2. Kelner, Tomas. "The Art of Engineering: The World's Largest Jet Engine Shows Off Composite Curves." *GE Reports*. General Electric, 29 Apr. 2016. Web. 18 Mar. 2017. <http://www.gereports.com/the-art-of-engineering-the-worlds-largest-jet-engine-shows-off-composite-curves/>.
3. Moran, M.J., Shapiro, H.N. *Fundamentals of Engineering Thermodynamcs, 6th Ed.* Hoboken, NJ: John Wiley and Sons, 2008.
4. Bogard, D. G. and Thole, K. A., "Gas Turbine Film Cooling," *Journal of Propulsion and Power*, Vol. 22, No. 2, 2006, pp. 249-270.
5. Boyd EJ, McClintic JW, Chavez KF, Bogard DG. Direct Measurement of Heat Transfer Coefficient Augmentation at Multiple Density Ratios. ASME. *J. Turbomach.* 2016;139(1):011005-011005-11. doi:10.1115/1.4034190.
6. Goldstein, R. J., Eckert, E. R. G., and Burggraf, F., "Effects of Hole Geometry and Density on Three-Dimensional Film Cooling," International Journal of Heat and Mass Transfer, Vol. 17, No. 5, 1974, pp. 595–607.
7. Saumweber, C., and Schulz, A., 2012, "Effect of Geometry Variations on the Cooling Performance of Fan-Shaped Cooling Holes," ASME J. Turbomach., 134(6), p. 061008.
8. Gritsch MM, Schulz AA, Wittig SS. Discharge Coefficient Measurements of Film-Cooling Holes With Expanded Exits. ASME. *J. Turbomach.* 1998;120(3):557-563. doi:10.1115/1.2841753.
9. Colban, W.F., Thole, K.A., and Bogard, D. "A Film Cooling Correlation For Shaped Holes on a Flat-Plate Surface." ASME J. Turbomachinery, 133(1) (2011) 011002
10. Ito, S. Goldstein, R.J., and Eckert, E.R.G., 1978, "Film cooling of a Gas Turbine Blade," ASME J. Gas Turbine Power, 100 (July 1978), pp.476-481
11. Lutum, E., von Wolfersdorf, J., Semmler, K. et al. Heat and Mass Transfer (2001) 38: 7. doi:10.1007/s002310000149
12. Zhang L, Moon H. Turbine Blade Film Cooling Study: The Effects of Film Hole Location on the Pressure Side. ASME. Turbo Expo: Power for Land, Sea, and Air, Volume 4: Turbo Expo 2007, Parts A and B ():497-506. doi:10.1115/GT2007-27546.
13. Saumweber C, Schulz A, Wittig S. Free-Stream Turbulence Effects on Film Cooling With Shaped Holes. ASME. J. Turbomach. 2003;125(1):65-73. doi:10.1115/1.1515336.
14. Liu, C., Liu, J., Zhu, H., Wu, A., He, Y., Zhou, Z., Film cooling sensitivity of laidback fanshape holes to variations in exit configuration and mainstream

turbulence intensity, International Journal of Heat and Mass Transfer, Volume 89, October 2015, Pages 1141-1154, ISSN 0017-9310, https://doi.org/10.1016/j.ijheatmasstransfer.2015.06.019.
15. Guo, S. M., Lai, C. C., Jones, T. V., Oldfield, M. L. G., Lock, G. D., and Rawlinson, A. J., 1998, "The Application of Thin-Film Technology to Measure Turbine-Vane Heat Transfer and Effectiveness in a Film-Cooled, EngineSimulated Environment," Int. J. Heat Fluid Flow, 19, pp. 594–600
16. Gao, Z. H., Narzary, D., Mhetras, S., and Han, J. C., Full Coverage Film Cooling for a Turbine Blade With Axial Shaped Holes, 39th AIAA Thermophysics Conference, 25–28 June, Miami, Florida, USA. AIAA 2007-4031, 2007.
17. S. Mhetras, J.-C. Han, R. Rudolph, Effect of flow parameter variation on full coverage film-cooling effectiveness for a gas turbine blade, J. Turbomach. 134 (1) (2012) 011004.
18. Colban WW, Gratton AA, Thole KA, Haendler MM. Heat Transfer and Film-Cooling Measurements on a Stator Vane With Fan-Shaped Cooling Holes. ASME. J. Turbomach. 2005;128(1):53-61. doi:10.1115/1.2098789.
19. Polanka MD, Ethridge MI, Cutbirth J, Bogard DG. Effects of Showerhead Injection on Film Cooling Effectiveness for a Downstream Row of Holes. ASME. Turbo Expo: Power for Land, Sea, and Air, Volume 3: Heat Transfer; Electric Power; Industrial and Cogeneration ():V003T01A048. doi:10.1115/2000-GT-0240.
20. Kinell, M., Utriainen, E., Najafabadi, H. N., Karlsson, M., and Barabas, B., "Comparison of Gas Turbine Vane Pressure Side and Suction Side Film Cooling Performance and the Applicability of Superposition," ASME Turbo Expo 2012: Turbine Technical Conference and Exposition, American Soc. of Mechanical Engineers, New York, 2012, pp. 1479–1489.
21. Chavez, K.F. *Variable Incidence Angle Film Cooling Experiments on a Scaled Up Turbine Airfoil Model.* Unpublished PhD Dissertation, Austin TX: The University of Texas at Austin, 2016
22. Mosberg, N.A., *Experimental Investigation of the Performance of a Fully Cooled Turbine Vane with and without Mainstream Flow and Experimental Analysis supporting the Redesign of a Wind Tunnel Test Section.* Unpublished Masters Thesis, Austin TX:
23. Chavez, K.F. Unpublished TTCRL Report, Austin TX: The University of Texas at Austin, 2015
24. Albert, J.E. *Experimental Simulation and Mitigation of Contaminant Deposition on Film Cooled Gas Turbine Airfoil.* Unpublished PhD Dissertation, Austin, TX: The University of Texas at Austin, 2011.
25. Gritsch, M., Schulz, A., and Wittig, S., "Effect of Crossflows on the Discharge Coefficient of Film Cooling Holes with Varying Angles of Inclination and Orientation," *J. Turbomach*., vol. 123, 2001, pp. 781-787.

26. Hartley,R., and Zisserman, A., 2004, MultipleView Geometry in Computer Vision, Cambridge Univ Pr
27. Rutledge, J.L. *Suction Side Roughness effects on Film Cooling Heat Transfer on a Turbine Vane (Unpublished Masters' thesis).* Unpublished Masters' thesis, Austin, TX: The University of Texas at Austin, 2004.
28. Kline, S.J., McClintock, F.A. "Estimating the Uncertainty in Single-Sample Experiments." *Mechanical Engineering*, Jan. 1953.
29. Moffat, R.J. "Describing the Uncertainties in Experimental Results." *Experimental Thermal and Fluid Science*, 1988: 3-17.
30. Montgomery, D.C., and Runger,G.C., 2003. Applied Statistics and Probability for Engineers, 3rd Edition.
31. Kistenmacher, D.A., "*Experimental Investigation of Film Cooling and Thermal Barrier Coatings on a Gas Turbine Vane with Conjugate Heat Transfer Effects*." Unpublished Masters' thesis, Austin, TX: The University of Texas at Austin, 2013.
32. Packard, G., "*Experimentally Determined External Heat Transfer Coefficient of a Turbine Airfoil Design at Varying Incidence Angles."* Unpublished Masters' thesis, Austin, TX: The University of Texas at Austin, 2015.
33. McClintic, J.W., *"Diffused-Exit Film Cooling Holes Fed by an Internal Crossflow."* Unpublished PhD Dissertation, Austin TX: The University of Texas at Austin, 2017
34. Cutbirth J, Bogard DG. Evaluation of Pressure Side Film Cooling With Flow and Thermal Field Measurements: Part I — Showerhead Effects. ASME. Turbo Expo: Power for Land, Sea, and Air, Volume 3: Turbo Expo 2002, Parts A and B ():89-98. doi:10.1115/GT2002-30174.

Vita

Owen O'Neal was born and raised in Tuscaloosa, Alabama. He earned his B.S. in mechanical engineering from Stanford University in 2015. He then began studying for his master's degree in mechanical engineering with a focus in thermal/fluid systems at the University of Texas at Austin. His research with Dr. David Bogard the past two years has culminated in the writing of this thesis.

Permanent email: owen.oneal28@gmail.com
This thesis was typed by the author.